FORMATION OF PRIMORDIAL BLACK HOLES

Thesis submitted for the degree of
"Doctor Philosophiæ"

CANDIDATE
Ilia Musco

SUPERVISOR
Professor J.C. Miller

International School for Advanced Studies
SISSA–ISAS

March 2006

To my parents

Rita and Guido

To the one who guided me in this research

To John C. Miller

for all his passion devoted to science

To those who showed me that everything is possible

W. & A.

FORMATION OF PRIMORDIAL BLACK HOLES

Ilia Musco — *Ph.D. Thesis*

Supervisor: J.C. Miller

Abstract

This thesis presents results from general relativistic numerical computations of primordial black-hole formation during the radiation-dominated era of the universe. Growing-mode perturbations are specified within the linear regime and their subsequent evolution is followed as they become nonlinear. We use a spherically symmetric Lagrangian code and study both super-critical perturbations, which go on to produce black holes, and sub-critical perturbations, for which the overdensity eventually disperses into the background medium. For super-critical perturbations, we revisit the results of previous work concerning scaling-laws, noting that the threshold amplitude for a perturbation to lead to black-hole formation is substantially reduced when the initial conditions are taken to represent purely growing modes. For sub-critical cases, where an initial collapse is followed by a subsequent re-expansion, strong compressions and rarefactions are seen for perturbation amplitudes near to the threshold. We have also investigated the effect of including a significant component of vacuum energy and have calculated the resulting changes in the threshold and in the slope of the scaling law.

The specification of the growing-mode perturbations in the above work is approximate and in the later part of the thesis, we introduce a more sophisticated and elegant formulation in terms of curvature perturbations. This allows a direct connection to be made with the spectrum of perturbations coming from inflation and also, using this, we find that there is no longer evidence of shock production in connection with primordial black hole formation. Introducing adaptive mesh refinement into our code, we are able to follow black hole formation nearer to the critical limit and find evidence suggesting that scaling laws may continue down to very small masses, in contrast with previous suggestions in the literature.

Contents

List of Figures

Acknowledgements

First of all I would like to thank my supervisor John Miller who guided me in this work and during all my PhD at SISSA. He has always been ready to support and encourage me, also when the situation has been difficult. He has followed me with patience and enthusiasm and I am really very grateful to him. I want also to thank the present and previous heads of the Astrophysics Sector, Annalisa Celotti and Luigi Danese, together with of all my colleagues in the Sector, for their support and the possibility given to me to develop this work in an exciting and stimulating group. In particular I want to mention Luciano Rezzolla for his help and guidance, particularly in the early part of this work, and Stefano Liberati and Carlo Baccigaluppi for the useful discussions that I have had with them. I also want to thank Bernard Carr and Alexander Polnarev from Queen Mary University of London who have contributed important ideas to my research, some of which are present in this thesis. I also want to thank other colleagues with which I have had interesting discussions and with whom I hope to work more closely in the near future: Marco Bruni, Karsten Jedamzik, Karsten Gundlach, Ian Hawke, Diego Pavon, Pedro Ferreira, Roy Maartens and Thanu Padmanabhan. Finally I want to thank my parents for their support, which has always been present.

Introduction

In the 1970's Stephen Hawking gave an important contribution to the understanding of black hole physics with the discovery of quantum effects associated with these objects. This gave rise to the well known theory of black hole evaporation. What is probably not very well known is that the idea of having black holes formed in the early universe (so called primordial black holes) is the historical reason that led Hawking to this famous discovery. In 1971, in fact [1], he considered the gravitational collapse of primordial perturbations in the early universe, when the fluid is described by a relativistic equation of state, realising that it can lead to the formation of primordial black holes (PBHs) if the perturbation amplitude is sufficiently high. To make a simple estimate of the mass scale of PBHs we can compare the density of the early universe at a certain time t with the density associated with a black hole of mass M, and we can see that the mass of PBHs would be of the order of the horizon mass at their formation epoch

$$M_H = 2t \simeq 10^{15} \left(\frac{t}{10^{-23}\ \mathrm{s}} \right)\ \mathrm{g}\,. \tag{1}$$

This relation indicates that the masses of PBHs would span a wide range of orders of magnitude with the possibility of forming very small black holes (with sizes comparable with ones of the elementary particles) that it is not possible to form in other astrophysical scenarios. Hawking realised that such small black holes could be strongly affected by quantum theory and his famous work in 1974 showed that the mass-energy of a black hole is evaporated away with a thermal radiation spectrum.

From that time, the interest of Hawking in black holes continued to follow the line of unifying the theory of general relativity with quantum mechanics (quantum gravity), leaving the subject of PBHs to be investigated by other colleagues. One in particular, Bernard Carr, who was a student of Hawking in those years at Cambridge, worked with him on producing the first quantitative work on PBHs [2], and then continued independently throughout his subsequent career to be actively interested in this subject.

I began to be interested in PBHs during my undergraduate thesis work, collaborating with my present supervisor John Miller, and his colleague Luciano Rezzolla at SISSA, who guided me in the understanding of relativistic astrophysics and taught me the numerical techniques that have been fundamental for this thesis. In summer 2003, during the second year of my PhD, I was introduced to Bernard Carr and his colleague Alexander Polnarev at Queen Mary University of London. Dr. Polnarev is another leading person in the field of PBHs; he was, in fact, one of the group of students of Zel'dovich (together with Novikov and Nadezhin) who in 1978 performed the first numerical calculation of PBH formation. One of the main original

contributions of this thesis is due to ideas developed in collaboration with Carr & Polnarev and we will try to show how the old ideas of the seventies, revisited in view of modern ideas of cosmology, and deeply analysed with modern numerical techniques, can bring new light and new interest to the study of PBHs.

The formation of PBHs has, so far, been just a possibility admitted by theory and it is still very unclear whether they have a relevant cosmological impact. This depends on their effective rate of formation, and on the distribution that they have now if they have survived. If their mass is smaller than 10^{15} g, they will have completely evaporated away by now and their main cosmological impact is given by the radiation emitted in the universe during their lifetime. If their mass is larger than 10^{15} g, then the evaporation process is negligible and they can be considered as candidates for different kinds of observation related to compact objects. In particular there are three mass scales of PBHs that are particularly interesting, the ones of the order of a solar mass (like MACHO type objects), ones of a few hundred solar masses (the intermediate mass black hole range) and the largest ones that it is possible to form, of the order of 10^5 - 10^6 solar masses, which might be the seeds to form the supermassive black holes that we observe in the centres of galaxies. The scales correspond, in the history of the early universe, to times ranging from that of the QCD phase-transition up to that of nucleosynthesis. In general, the cosmological consideration of PBHs forming in the early universe can put strong constraints on models of cosmological perturbations, and therefore studying their possible formation is matter of interest even if their formation rate turns out to be very small. In our opinion the link between a realistic cosmological scenario characterised by a Gaussian spectrum of primordial perturbations and the numerical calculations presented in the recent literature is not very strong and needs revision in the way of introducing initial conditions. This thesis makes a contribution towards understanding how to treat this better.

Plan of the work

The work is divided in two parts. The first part (Chapters 1 - 3) reviews results taken from established theory and recent published works. The second part (Chapters 4 - 6) describes the original contributions of this thesis to the study of PBHs, giving particular attention to the treatment of imposing initial conditions and to the subject of critical collapse

Chapter 1 gives a description of the standard theory of the hot big bang, describing very synthetically the unperturbed universe, focusing attention on the radiative epoch when the fluid was relativistic. Chapter 2 then reviews the standard theory of cosmological perturbations coming as a Gaussian spectrum produced by inflation. We start with an introduction to the idea of inflation, explaining how this mechanism affects the evolution of the universe and how it can produce a spectrum of cosmological perturbations. Then we give a detailed analysis of the linear theory of cosmological perturbations, that is a crucial basis for the developments of the original calculations presented in the following chapters.

Chapter 3 gives an introduction to ideas about black holes and makes a summary of the results in the literature about PBHs. The material to be included here could cover a very wide range and we have therefore made a selection, presenting the subject of PBHs from our

perspective, pointing out the main points that we think need to be studied more carefully.

Chapter 4 explains the hydrodynamical scheme used in our calculations, presenting the set of equations used to write the computer code. We then show results from numerical calculations made with initial conditions similar to ones used previously in the literature, but with a fundamental improvement. Which clarifies an inconsistency that was noticed recently, comparing two different sets of calculations.

Chapter 5 explains a new formulation for introducing initial conditions to be used in the numerical simulations. We demonstrate that this formulation is self consistent for a spectrum of perturbations coming from inflation and allows the perturbations of all of the hydrodynamical variables to be expressed as functions of a unique time independent-variable, which is directly linked with the curvature perturbation.

Chapter 6 investigates critical collapse, related to the formation of the smallest mass PBHs at any given time, where the new formulation for specifying initial conditions explained in the previous chapter is used. With an adaptive scheme for the numerical grid we have been able to investigate regions of the mass spectrum that we were not able to investigate before.

The results presented in Chapter 4 and 5 have been presented in two different papers [3, 4], while the results of Chapter 6 will be presented soon in a paper that is in preparation [5].

Chapter 1

Cosmology of the early Universe

The aim of this chapter is to summarise the elements of cosmology applied to the description of the early Universe, the background scenario for primordial black hole formation. The main references used are [6, 7, 8]. For more specific details other references are specified in the text.

The "standard" theory of the early Universe is the so called **Hot Big Bang** based on the *cosmological principle* which says that, at least on large scales, the Universe is homogeneous and isotropic. This is an observational statement and the most relevant observational proof of it is the nearly identical temperature of the microwave background radiation coming from different parts of the sky.

To clearly describe the evolution of the Universe it is convenient to divide it into two parts. The large scale behaviour of the Universe can be described by assuming a homogeneous and isotropic background. On the background it is then possible to superimpose perturbations on different scales that evolving with time would give rise to the structures observed today in the current Universe. This chapter is dedicated to the first of these two parts, giving attention to all of the various aspects that play a role in the context of the PBH scenario.

1.1 The Friedmann Model

1.1.1 Hubble parameter and redshift

The first observational statement about the behaviour of the Universe is that it is expanding with a rate measured by a universal scale factor $a(t)$, where t is the *cosmic time* as measured by a family of "comoving fundamental observer". For a point comoving with the expansion of the Universe its distance measured from a defined location, can be written as

$$R(t) = a(t)\, r\,, \tag{1.1}$$

where r is the **comoving variable** appearing in the metric defined later. An equivalent relation can be used to define a useful time variable, known as **conformal time**

$$d\tau = \frac{dt}{a(t)}\,. \tag{1.2}$$

The rate of the expansion of the Universe is given at any time by the **Hubble parameter**

$$H \equiv \frac{1}{a}\frac{da}{dt} = \frac{\dot{a}}{a} \tag{1.3}$$

explicitly appearing in the Hubble law, measuring the expansion velocity U, obtained through the time derivative of expression (1.1),

$$U \equiv \frac{dR}{dt} = HR. \tag{1.4}$$

H has the dimension of the inverse of a time and H^{-1}, called the **Hubble time**, represents a first order estimate of the age of the Universe when H is measured. The Hubble length cH^{-1} is called the **horizon** scale of the Universe (see section 1.2) because it provides an estimate of the distance that light (idealised carrier of information) can travel while the Universe is expanding. Later we will use two other quantities called "horizons": the **particle horizon** (see section 1.2) is the distance that light could have travelled since the beginning of the Universe at $a = 0$, while the **event horizon** (see Chapter 3) is the limiting distance that light would be able to travel in the future. From the cosmological point of view the Hubble horizon is the most important and therefore we will often refer to it just as "the horizon".

The expansion of the Universe is usually measured with the redshift z, defined as the change of wavelength $d\lambda/\lambda$ of a photon that moves between the source and the observer, given by

$$1 + z \equiv \frac{\lambda_{\text{obs}}}{\lambda_{\text{emit}}}, \tag{1.5}$$

where λ_{obs} and λ_{emit} are the observed and the emitted wavelength. Because $\lambda = a/k$, where k is the comoving wave number used in Fourier expansion, the redshift z is directly related to scale factor a, by

$$1 + z = \frac{a(t_0)}{a(t_1)} \tag{1.6}$$

where the observer is supposed to be at the present epoch t_0, and t_1 is the time of emission. The observed redshift of the objects allows us to get a measure of the present value of the Hubble parameter, affected by the uncertainty on the measure of distance of the objects. This measure actually gives

$$H_0 = 100h \text{ km s}^{-1} \text{ Mpc}^{-1} = \frac{hc}{3000} \text{ Mpc}^{-1},$$

where h specifies the actual observational value.

1.1.2 The metric

Starting with this point we will use for all the thesis the geometrical units ($G = c = 1$), but sometimes, when we think it is useful, we will write the constants explicitly.

In general a homogeneous and isotropic Universe is described by the **Friedmann-Robertson-Walker (FRW) metric** given by

$$ds^2 = -dt^2 + a^2(t)\left[\frac{dr^2}{1 - Kr^2} + r^2\left(d\theta^2 + \sin^2\theta d\phi^2\right)\right]. \tag{1.7}$$

The constant K is a curvature parameter with $K = 0, -1, +1$, corresponding to a flat, open or closed Universe; $a(t)$ is the scale factor of the Universe, where t is the **cosmic time**, and (r, θ, ϕ) are the comoving spatial coordinates.

The definition of the conformal time given by (1.2) allows us to transform the FRW metric into a different form that will be useful in the following chapter when we deal with metric perturbations. Using conformal time the scale factor term a^2 multiplies the entire line element and all the time dependence is isolated into a unique multiplicative factor.

$$ds^2 = a^2(\tau)\left[-d\tau^2 + d\chi^2 + f^2(\chi)\left(d\theta^2 + \sin^2\theta d\phi^2\right)\right] \tag{1.8}$$

where

$$\chi = \int \frac{dr}{\sqrt{1-Kr^2}} = \begin{cases} \sin^{-1} r & (K=1) \\ r & (K=0) \\ \sinh^{-1} r & (K=-1) \end{cases} \tag{1.9}$$

and

$$f(\chi) = = \begin{cases} \sin^{-1} r & (K=1) \\ r & (K=0) \\ \sinh^{-1} r & (K=-1) \end{cases} \tag{1.10}$$

An alternative way to write the metric (1.7) is to transform the space coordinate instead of time coordinate. Setting

$$r = \frac{u}{1+Ku^2/4} \tag{1.11}$$

one gets the **isotropic** form of the FRW metric, given by

$$ds^2 = -dt^2 + \frac{a^2(t)}{\left(1+Ku^2/4\right)^2}\left[du^2 + u^2\left(d\theta^2 + \sin^2\theta d\phi^2\right)\right]. \tag{1.12}$$

It this way the spatial 3-metric component inside the square brackets has the same form as the flat metric, and the curvature component appears just outside the brackets.

1.1.3 Friedmann and continuity equations

The general relation between acceleration of the Universe and gravitational sources is described by the Einstein equations

$$R_{\mu\nu} - \frac{1}{2}g_{\mu\nu}R = -8\pi T_{\mu\nu} + \Lambda g_{\mu\nu} \tag{1.13}$$

where on the left hand side there are the geometrical terms $R_{\mu\nu}$, $g_{\mu\nu}$ and R: the Ricci tensor, the metric tensor and the Ricci scalar. On the right hand side there are the source terms, $T_{\mu\nu}$ is the energy momentum tensor and Λ is the cosmological constant (this term could also

be placed in the left hand side). We are treating the medium as a perfect fluid for which the energy momentum tensor is given by

$$T_{\mu\nu} = -pg_{\mu\nu} + (p+e)\, u_\mu u_\nu \,, \tag{1.14}$$

where e is the energy density and p is the pressure.

Using the metric tensor of the FRW metric (1.7) one obtains the fundamental equations that describe the evolution of the Universe:

$$H^2 = \frac{8\pi}{3}e + \frac{\Lambda}{3} - \frac{K}{a^2} \qquad \text{Friedmann equation} \tag{1.15}$$

$$\dot{e} + 3H(e+p) = 0 \qquad \text{Continuity equation} \tag{1.16}$$

The Friedmann equation (1.15) is obtained from the time component of Einstein equation, while the continuity equation (1.16) is derived from the radial component (due to the spherical symmetry the other spatial components give the same result as the radial one). The continuity equation is equivalent to the energy conservation law for adiabatic expansion, $dE = -pdV$ where $E = eV$ is the energy in a comoving volume $V \propto a^3$. Therefore the term $3He$ is the change of energy density due to the expanding volume and $3Hp$ is the energy change due to the hydrodynamical pressure acting on the expansion.

These two equations can be combined into a third one where the acceleration of the expansion $\ddot{a}$ appears directly.

$$\frac{\ddot{a}}{a} = -\frac{4\pi G}{3}(e+3p) \qquad \text{Acceleration equation} \tag{1.17}$$

From the Friedmann equation it is possible to derive a particular value of the density ρ ($e = \rho c^2$), known as the critical density, for which the Universe is spatially flat in the absence of a cosmological constant,

$$\rho_c = \frac{3H^2}{8\pi} \tag{1.18}$$

and at the present time t_0 we have

$$\rho_c(t_0) = 1.88h^2 \cdot 10^{-29} \text{ g cm}^{-3} = 2.77h^{-1} \cdot 10^{11} M_\odot / \left(h^{-1} \text{ Mpc}\right)^3 .$$

This is very useful because we can discriminate between an open and closed Universe with the density parameter

$$\Omega \equiv \frac{\rho}{\rho_c} \,. \tag{1.19}$$

1.1.4 The equation of state

In general the early Universe is assumed to be very well described by a perfect fluid, except at inflation or possible phase transitions, which are thought to be brief. For the cases of major interest it is possible to use a simple equation of state for each component of the fluid such as

$$p = \gamma e \tag{1.20}$$

where γ is a constant determined by the nature of the fluid: $\gamma = 0$ for non relativistic particles (matter domination era), $\gamma = 1/3$ for relativistic particles (radiation domination era), $\gamma = -1$ for vacuum energy (cosmological constant dominated era). [1] The γ parameter is related to the sound speed for an adiabatic fluid

$$c_s^2 = \left(\frac{\partial p}{\partial e}\right)_s = \gamma, \tag{1.21}$$

where s denotes the specific entropy.

The cosmological constant term present in the Einstein equations can be interpreted either as a geometrical term or a source term. This second option, chosen to write expression (1.13), can be very useful and leads to a simple expression for an effective equation of state taking into account of both the normal matter and the cosmological term that can be included inside the expression for the energy momentum tensor

$$\tilde{T}_{\mu\nu} = T_{\mu\nu} + \frac{\Lambda c^4}{8\pi G} g_{\mu\nu} = -\tilde{p} g_{\mu\nu} + \left(\tilde{p} + \tilde{\rho} c^2\right) u_\mu u_\nu, \tag{1.22}$$

with the effective pressure $\tilde{p}$ and effective energy $\tilde{\rho}$ are related to the normal quantities by:

$$\tilde{p} = p - \frac{\Lambda}{8\pi}, \qquad \tilde{e} = e + \frac{\Lambda}{8\pi}, \tag{1.23}$$

that combined together with (1.20) gives

$$\tilde{p} = \gamma\left(\tilde{e} - \frac{1+\gamma}{\gamma}\frac{\Lambda}{8\pi}\right). \tag{1.24}$$

This expressions is equivalent to (1.20) when $e = 0$ and $\gamma = -1$.

1.1.5 The dynamics of the Friedmann model

The solution of the Friedmann equation and continuity equation with $\Lambda = 0$ is the so called Friedmann Universe model. The substitution of the equation of state in the Friedmann and continuity equation gives a general solution for the evolution of the energy density given by

$$e = e_0 \left(\frac{a}{a_0}\right)^{-3(1+\gamma)}. \tag{1.25}$$

Combining the Friedmann equation with the equation of state and the expression for critical density Ω measured at the present time t_0 we obtain

$$H^2 = H_0^2 \left(\frac{a_0}{a}\right)^2 \left[\Omega_0 \left(\frac{a_0}{a}\right)^{1+3\gamma} + (1 - \Omega_0)\right]. \tag{1.26}$$

If we substitute the evolution of density ρ in the definition of Ω given by (1.19) and then insert in (1.26) we have an expression for the evolution of the Hubble parameter as function of redshift,

$$H^2(z) = H_0^2 (1+z)^2 \left[\Omega_0 (1+z)^{1+3\gamma} + (1 - \Omega_0)\right] \tag{1.27}$$

[1] Note that this usage of γ is to be distinguished from that appearing in the polytropic law $p = k\rho^\gamma = (\gamma - 1)\rho\epsilon$, with ρ being the rest mass density and ϵ being the specific internal energy per unit mass. For a radiation fluid this gives $p = (\gamma - 1)e$

Finally, substituting this into (1.19) we get an important equation

$$\Omega(z) = \frac{\Omega_0 (1+z)^{1+3\gamma}}{(1-\Omega_0) + \Omega_0 (1+z)^{1+3\gamma}}, \tag{1.28}$$

which shows the property of the Universe to conserve the sign of spatial curvature. Infact if Ω is measured to be greater or smaller than one at a particular time it would be like that at every time. In the special case of $\Omega = 1$ at a particular time it is just constant. In other words if we measure our Universe to be spatially open, closed or flat at the present time, it would have this property during all its past and future evolution.

The special case of $\Omega = 1$ is particularly important because we think that the Universe roughly satisfies this and it is the one which we will use to describe the early Universe. The explicit solution is easily written.

$$a = a_0 \left(\frac{t}{t_0}\right)^{2/3(1+\gamma)} \tag{1.29}$$

$$H = \frac{2}{3(1+\gamma)t} = H_0 \frac{t_0}{t} = H_0 (1+z)^{3(1+\gamma)/2} \tag{1.30}$$

$$e = e_0 \left(\frac{t_0}{t}\right)^2 = \frac{1}{6(1+\gamma)^2 \pi t^2} \tag{1.31}$$

In the more general case of Λ not equal to zero it is also possible to get an explicit analytical solution that is described in Appendix 1.

1.2 Scales of the Universe

1.2.1 Hubble Horizon

The fundamental time scale in an expanding Universe is given by the reciprocal of the Hubble parameter, H^{-1}. This time scale corresponds to a length scale which is called Hubble horizon scale defined as

$$R_H = \frac{1}{H}. \tag{1.32}$$

This gives an estimate of the size of the region over which physical processes operate coherently and it is also the length-scale at which general relativistic effects become important. An important related quantity is the **Horizon Mass**, defined as the mass inside the Hubble horizon.

$$M_H = \frac{4}{3}\pi e R_H^3 \tag{1.33}$$

In the Friedmann model, described in the previous section, where the evolution of the scale factor is just a power law of time, the horizon scale is given by

$$R_H = \frac{3(1+\gamma)}{2} t, \tag{1.34}$$

which grows linearly with time. The horizon is therefore expanding faster than physical distances ($d \propto t^{1/2}$). This has an important cosmological consequence, because regions that at an

early time are separated by a distance greater than the horizon scale, would later be separated by a distance smaller than the horizon. The horizon crossing moment, corresponding to the time when the size of a defined region $R_0 = a(t)r_0$ is equal to R_H, is in first approximation the moment when all of the matter in the perturbation has come into causal contact. In the Friedmann model, using the explicit expression for the energy density, the expression for the horizon mass is given by

$$M_H = \frac{3(1+\gamma)}{4}t, \tag{1.35}$$

From this expression we can see that the horizon scale can be related to the corresponding mass by

$$R_H = 2M_H \tag{1.36}$$

the same expression that we find for the **event horizon** when we discuss black holes in chapter 3. We will see better there that this is not a coincidence, because the physical nature of these two horizons is similar.

1.2.2 Particle Horizon

The coordinate distance travelled by a freely moving photon emitted at time t and observed at the present time is

$$d(t) = \int_t^{t_0} \frac{dt}{a}. \tag{1.37}$$

In the limit of the initial time of the Universe $t \to 0$, using the idealisation of $a(0) = 0$ the integral remains convergent. Replacing the present time with an arbitrary epoch we get the definition of the **particle horizon** scale

$$R_{\rm hor} = a_0 \int_0^t \frac{dt}{a}. \tag{1.38}$$

In the Friedmann model with $\Omega = 1$ the integral is easily solved by

$$R_{\rm hor} = \frac{3(1+\gamma)}{5+3\gamma}t = \frac{2}{5+3\gamma}R_H\,. \tag{1.39}$$

1.3 Epochs of the Universe

The contents of the Universe in the early epochs consisted of very hot gas. In particular our main objective is to describe a radiative fluid corresponding to a phase of the Universe when the temperature T of the fluid was higher than the rest mass of particles. To enter more into detail we describe synthetically below the gas thermodynamics during the Hot Big Bang (discussed more extensively in [8]).

1.3.1 Gas dynamics in flat space time

In statistical thermodynamics, without considering particle spin, the properties of an ideal gas are specified completely by the *distribution function* $f(t, \mathbf{r}, \mathbf{p})$, which gives the number dN of

particles with position $\mathbf{r}$ and momentum $\mathbf{p}$. We assume that the processes of interaction between particles are homogeneous, with a sufficiently fast transition rate Γ. The interaction between particles is considered as a thermalization process that produces and maintains thermodynamic equilibrium among the interacting particles with some temperature $T(t)$. Therefore we can treat the system of particles as an ideal Bose or Fermi gas, characterised by a distribution function

$$f(\mathbf{p}) = \frac{g_i}{(2\pi)^3} \frac{1}{\exp[(E_\mathbf{p} - \mu_i)/T] \pm 1}, \tag{1.40}$$

where g_i is the spin degeneracy factor of the species of particles, μ_i is the chemical potential, $E(\mathbf{p}) = (p^2 + m^2)^{1/2}$ is the total energy and T the temperature. The plus sign corresponds to fermions and the minus one to bosons.

At any instant of time the Universe contains a black body distribution of photons with some characteristic temperature $T_\gamma(t)$. If a particular species of particles is coupled with the photons with a high enough rate of interaction ($\Gamma > H$), then these particles will have the same temperature as the photons. Because this is the case in the early Universe, the photon temperature is considered as the temperature of the Universe. With the expansion of the Universe, the temperature changes on the Hubble time scale H^{-1}.

The energy density, pressure and number density of particles can be calculated using the distribution function, where we suppress the time dependence and the subscript i for simplicity.

$$n = \int f(\mathbf{p}) d\mathbf{p} \tag{1.41}$$

$$e = \int f(\mathbf{p}) E(\mathbf{p}) d\mathbf{p} \tag{1.42}$$

$$p = \int f(\mathbf{p}) \frac{\mathbf{p}}{E(\mathbf{p})} d\mathbf{p} \tag{1.43}$$

For a relativistic fluid $E \simeq |\mathbf{p}|$, while for non relativistic matter $E \simeq m$ and in spherical symmetry $d\mathbf{p} = 4\pi p^2 dp$.

1.3.2 Radiation dominated era

In the first period of the Universe the fluid particles are relativistic and their behaviour is therefore described as pure **radiation**. The photon distribution has the black body form and the energy density is directly related to temperature by

$$e_\gamma = \frac{\pi}{30} g_\gamma T^4. \tag{1.44}$$

Here the Boltzmann constant has been set equal to 1 and $g_\gamma = 2$ is the number of spin states of the photon. This gives a photon number density equal to

$$n_\gamma = \frac{\zeta(3)}{\pi^2} g_\gamma T^3, \tag{1.45}$$

where ζ is the zeta function ($\zeta(3) = 1.202$).

In the radiation dominated era, photons and relativistic particles are in thermal equilibrium with chemical potential equal to zero. This means that the distribution of these particles is analogous to photons with a blackbody distribution, for both fermions and bosons. The energy and number density of each particular species of particles are given by expressions (1.44) and (1.45), with coefficient 3/4 for bosons and 7/8 for fermions. These expressions apply to any particular species of particles until it becomes non relativistic, corresponding to temperature $T \sim m$. In the radiation dominated era the energy density of the Universe is given by that of relativistic particles

$$e_R = \frac{\pi}{30} g_*(T) T^4 , \tag{1.46}$$

where

$$g_*(T) = \sum_{bosons} g_i + \frac{7}{8} \sum_{fermions} g_i . \tag{1.47}$$

The number of particle species $g_i(T)$ depends on temperature because at different temperatures there are different species in thermal equilibrium. In general $g_i(T)$ is an increasing function of temperature, where the exact profile of the function depends on the model of elementary particles is being considered (see for example Figure 2.1 of [6]).

A perfect fluid in thermodynamical equilibrium is also described by the second law of thermodynamics

$$de = Tds - p\frac{dV}{V} , \tag{1.48}$$

where here $V \propto a^3$ is the comoving volume, and s is the entropy density. Using (1.46) this gives

$$s = \frac{e+p}{T} = \frac{2\pi}{45} g_* T^3 \sim g_* n_\gamma . \tag{1.49}$$

This is a very important relation because it allows us to understand the variation of T with respect the scale factor. In fact, if the Universe is adiabatic (no heat transfer) and isotropic the entropy in a comoving volume $S = sa^3$ is constant, and therefore $T \propto g_*^{-1/3} a^{-1}$. The variation of g_* with temperature is negligible during the radiation dominated era, therefore

$$T \propto \frac{1}{a} . \tag{1.50}$$

This holds until the decoupling of neutrinos from the photons, corresponding to a temperature of $T \sim 1$ Mev.

In the Friedmann model, the radiation dominated era is characterised by (1.20) with $\gamma = 1/3$ which gives

$$e_R \propto a^{-4} \quad \text{and} \quad a \propto t^{1/2} . \tag{1.51}$$

1.3.3 The matter dominated era and the equivalence

At the present time we see that the Universe is dominated by non relativistic matter. In the Friedmann model this corresponds to equation of state (1.20) with $\gamma = 0$, because when the particles becomes non relativistic the pressure given by their peculiar velocities is negligible

with respect to their rest mass energy. Opposite to radiation, this kind of matter is sometimes called **dust**. Putting $\gamma = 0$ in the Friedmann model one gets

$$e_M \propto a^{-3} \quad \text{and} \quad a \propto t^{2/3}. \tag{1.52}$$

At a time $t = t_{eq}$ in the past, the energy density of radiation and dust should have been comparable,

$$e_R(t_{eq}) = e_c\,\Omega_R\,(1+z_{eq})^4 = e_M(t_{eq}) = e_c\,\Omega_M\,(1+z_{eq})^3\,. \tag{1.53}$$

This transition era is called *equivalence* and the corresponding redshift and temperature are

$$1 + z_{eq} = \frac{\Omega_M}{\Omega_R} = 24\,000\,\Omega_0 h^2\,, \tag{1.54}$$

$$T_{eq} = T_0(1+z_{eq}) = 65\,500\,\Omega_0 h^2\ K\,. \tag{1.55}$$

During this period the evolution of the scale factor is more complicated because we have to include both components in the Friedmann equation,

$$H^2 = \frac{8\pi}{3}\left[\left(\frac{a_{eq}}{a}\right)^3 + \left(\frac{a_{eq}}{a}\right)^4\right]. \tag{1.56}$$

This equation can be solved exactly in the conformal time τ but there is not an explicit analytical expression in cosmic time t,

$$\frac{a(\tau)}{a_{eq}} = (2\sqrt{2}-2)\left(\frac{\tau}{\tau_{eq}}\right) + (3-2\sqrt{2})\left(\frac{\tau}{\tau_{eq}}\right)^2, \tag{1.57}$$

$$\tau_{eq} = \frac{2\sqrt{2}-2}{a_{eq}}\sqrt{\frac{3}{8\pi e_{eq}}}\,. \tag{1.58}$$

1.3.4 The cosmological constant

Observations in recent years have indicated that matter in the Universe has less than the critical density and that at the present time the Universe is accelerating. A way to explain this, conserving a spatially flat Universe ($K = 0$) is to consider a non zero cosmological constant in the Friedmann equation (1.15),

$$H^2 = \frac{8\pi}{3}e + \frac{\Lambda}{3}\,. \tag{1.59}$$

When the Universe is dominated by the cosmological constant the solution gives an exponential expansion rate

$$a(t) \propto \exp\left(\sqrt{\frac{\Lambda}{3}}\,t\right). \tag{1.60}$$

In this case the Hubble horizon scale is constant, while the scale of the particle horizon grows from zero to reach asymptotically that of the Hubble horizon.

$$R_H = \left(\sqrt{\frac{\Lambda}{3}}\right)^{-1} \tag{1.61}$$

$$R_{hor} = \left[1 - \exp\sqrt{\frac{\Lambda}{3}}t\right] R_H \tag{1.62}$$

The observations of distant supernovae are thought to give an appropriate measurement of the expansion of the Universe. The result of these observations gives a value of the cosmological constant roughly comparable with the energy density of the present Universe ($\Omega_{M0} = 0.3$ and $\Omega_{\Lambda 0} = 0.7$), which means that the Universe has started to accelerate recently. This introduces a fine tuning problem that is being intensively studied. One possibility for avoiding this problem is to have Λ not being constant but evolving with time, giving rise to models known by the name of *quintessence* [9, 10].

1.4 The cosmic microwave background

The **cosmic microwave background** (CMB) was first detected in 1965. It is nearly a uniform signal at microwave frequencies, coming from every direction in the Universe with a high degree of isotropy. This signal is therefore not coming from discrete sources but it is understood as having been produced from the last moment of scattering of photons with matter. The CMB is characterised by a black body spectrum with an observed temperature of $T \simeq 2.7\,K$ at the present time. The very high degree of isotropy strongly supports having a homogeneous theory of the Universe on sufficiently large scales. Recently satellites such as COBE have measured small anisotropies ($\Delta T/T \simeq -10^5$) on angular scales larger than 1 deg, which corresponds to scales larger then the horizon scale at the time of the production of the CMB. Understanding the initial spectrum of cosmological perturbations is an important field of current research, which we discuss in the next chapter.

1.5 Thermal history of the Universe

In this last section we give a qualitative description of the history of the Universe, pointing out what modern cosmology speculates today for the very early moments before nucleosynthesis.

Nucleosynthesis is the era when the temperature of the Universe, of the order of 1 MeV, about 1 seconds after the big bang, allowed the formation of atomic nuclei. The predictions of the nucleosynthesis model are in very good agreement with observations: mainly Hydrogen at $\sim 75\%$ and Helium at $\sim 25\%$, while the presence of havier nuclei is very small [11, 12]. Nucleosynthesis is one of the great successes of hot big-bang cosmology and represents a threshold between what is considered standard cosmology and speculative theory with indirect observational evidence.

The high degree of isotropy measured in the Universe with the CMB suggests that at a certain primordial time the whole Universe should have been inside the Hubble Horizon, in thermal equilibrium. At a certain point a particular mechanism, called **inflation**, connected with the existence of scalar fields should have produced an exponential expansion with an enormous acceleration. Following the theory of inflation (see next chapter) the exponential acceleration is subsequently followed by an intermediate state where the scalar field decays

producing a reheating of the whole Universe that is left with a temperature where relativistic particles are dominant (radiation dominated epoch). The exponential acceleration makes the dimensions of the Universe much larger that the Hubble scale but conserves the high level of isotropy. Another important aspect of inflation is the possibility to have quantum oscillations of the scalar filed at the end of this process, with the effect of creating cosmological perturbations. The theory for the evolution of cosmological perturbations represents the basis for the origin of structures on different scales and it will be reviewed in the next chapter.

In the following we give just a synthetic overview of the main epochs of the Universe, starting from the very beginning at the Planck scale ($T_{Pl} \sim 10^{19}$ GeV):

- $T_{Pl} > T > 10^2$ Gev
  This is the epoch when inflation ($a(t) \propto \exp(t)$) is supposed to happen, leaving the Universe with a value of the reheating temperature between 10^{16} and 10^{10} GeV, depending on the model. The Universe then enters into the "hot big bang" evolution, dominated by relativistic particles, with the scale factor $a(t) \propto t^{1/2}$.

- 10^2 Gev$> T >$ 10 eV
  The temperature of 100 GeV corresponds to the Electroweak phase transition and the physics of particles is now described by the Standard Model or some extension of it. This is the first important phase transition at which the electromagnetic and weak forces separate and corresponds to the last possible time at which it is possible to generate baryon asymmetry (**baryogenesis**).

  Later, at $T \sim 100$ MeV there is a another important phase transition, corresponding to the QCD scale when free quarks became bound to form hadrons.

  For some time all the light particles (γ, ν, e, $\overline{e}$, n and p) are in thermal equilibrium, but when temperature $T \sim 1$ MeV there is the decoupling of neutrinos and $e\overline{e}$ annihilation.

  When $T \sim 0.1$ MeV there is nucleosynthesis with the formations of the nuclei of Hydrogen and Helium.

  Finally at $T \sim 10$ eV the non relativistic matter reaches a density comparable to the relativistic matter and the radiation epoch ends.

- $T <$ 10 eV
  With the onset of matter domination the rate of the expansion changes to $a(t) \propto t^{2/3}$. When $T \sim 0.1$ eV **recombination** occurs, where the majority of the electrons bind with nuclei to form atoms. Initially the photons remain coupled to the ionised electrons that remain free but soon afterwards the radiation decouples completely from the matter and the photons are free to propagate. This is what we see today as the CMB.

  After **decoupling** the sequence of thermal processes finishes and the rest of the history of the Universe is characterised by gravitational processes of structure formation.

Chapter 2

Cosmological perturbation theory

The aim of this chapter is to review some elements of cosmological perturbation theory that are fundamental for PBH formation. We have tried to be fairly synthetic but at the same time to give a homogeneous presentation of the main aspects.

Inflation is discussed in the first and second section, explaining which problems arise in the "hot big bang model" presented in the previous chapter, and summarising the inflation mechanism, that gives a mechanism to produce cosmological perturbations. In the third section we describe the statistical properties of cosmological perturbations and their spectrum. Finally in the fourth section we deal with the linear theory of cosmological perturbation evolution.

The main references for this chapter are [6, 7], other references are specified in the text.

2.1 The problems of the hot big bang model

One problem of the standard theory, known as the **flatness problem**, can be seen looking at the Friedmann equation (1.15) written explicitly for the density parameter Ω, that is

$$\Omega - 1 = \frac{k}{a^2 H^2} \,. \tag{2.1}$$

From observations we know that at the present time $\Omega \simeq 1$ which implies, remembering that $|\Omega - 1|_M \propto t^{2/3}$ and $|\Omega - 1|_R \propto t$ during radiation domination, that in the past Ω should have been much closer to 1 (for instance at the era of nucleosynthesis we have $|\Omega - 1| \lesssim 10^{-16}$). This gives a fine tuning problem because it is very unlike that initial conditions were tuned to be so close to a flat universe.

In the previous chapter we have discussed the existence of the CMB signal, characterised by a very high degree of isotropy on scales much larger than the horizon at the time of the last scattering. Also in this case there is no explanation for why regions of the universe that cannot have interacted before decoupling have almost the same temperature, and the homogeneity seems to be somehow part of the initial conditions. This is known as the **horizon problem**. Another important aspect of the CMB signal is the small irregularities measured for example by the COBE satellite. These perturbations are intrinsic to the last scattering surface and are

on too large scales with respect the Hubble length at that time to have been created in the early universe before decoupling. Therefore these perturbations must have been introduced at the very beginning of the early universe, before the standard hot big bang history.

2.2 Inflation

2.2.1 The idea of inflation

The idea of inflation comes directly from the problems described in the previous section: one needs a mechanism such that the horizon length is decreasing for a certain period of time and the universe accelerates, avoiding the fine tuning problem. In this way regions that initially were inside the horizon would be outside at the end of this process. Looking at the Friedmann, continuity and acceleration equations one clearly sees that this corresponds to three equivalent conditions:

$$\text{INFLATION} \iff \begin{cases} \ddot{a} < 0 \\ \\ \dfrac{d}{dt}\left(\dfrac{H^{-1}}{a}\right) \\ \\ e + 3p < 0 \end{cases} . \tag{2.2}$$

Because energy density is considered always positive the third condition of (2.2) implies that during inflation pressure is negative.

The flatness problem is solved because enough inflation would move any value of Ω very close to one so that it would be close to one until the present moment. The horizon problem is solved by the second expression of (2.2), and the geometrical behaviour of the Hubble scale is explained in Figure 2.1.

At the end of this section we will explain how inflation is connected with the origin of cosmological perturbations.

2.2.2 Scalar fields

Scalar fields are used in particle physics to describe particles with spin equal to zero and they are also associated with symmetry breaking between fundamental forces (although these fields have not been observed yet). It is therefore plausible to assume existence of scalar fields in the very early universe. The Lagrangian description of a homogeneous scalar field ϕ is given by

$$e_\phi = \frac{1}{2}\dot{\phi}^2 + V(\phi) \tag{2.3}$$

$$p_\phi = \frac{1}{2}\dot{\phi}^2 - V(\phi) \tag{2.4}$$

where the first term can be interpreted as kinetic energy and the second as potential energy. The form of the potential $V(\phi)$ of the scalar field determines in the evolutionary equation the

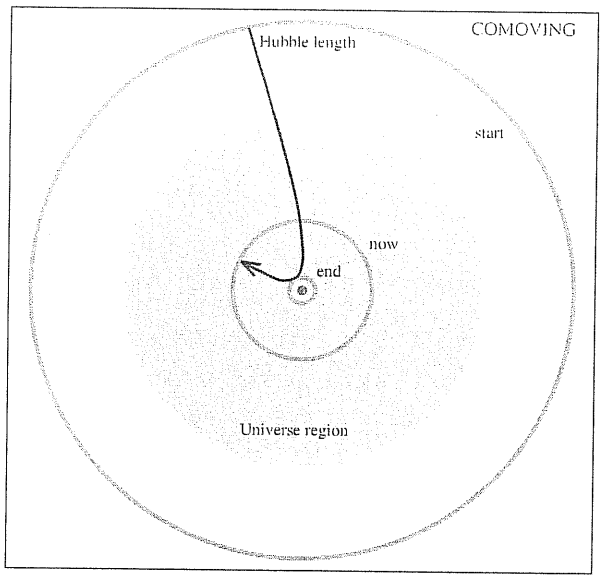

Figure 2.1: Schematic plot of the inflationary solutions to the horizon problem, where comoving units have been used. The figure has been taken from [6]

behaviour of inflation. In the present context we do not want to discuss the various possible forms of the potential, and therefore we treat $V(\phi)$ as a free function.

2.2.3 Equation of motion and solutions

Inflation is driven by the behaviour of the scalar field called the **inflaton** and its evolution is determined from the substitution of expressions (2.3) and (2.4) into the Friedmann and continuity equations, obtaining

$$H^2 = \frac{8\pi}{3}\left[V(\phi) + \frac{1}{2}\dot{\phi}^2\right] \tag{2.5}$$

and

$$\ddot{\phi} + 3H\dot{\phi} = -\frac{dV(\phi)}{d\phi}. \tag{2.6}$$

The expressions appearing in (2.2) imply that the condition for inflation is satisfied if $\dot{\phi}^2 < V(\phi)$ and this is provided when the potential is flat enough. This allows the equations to be solved in the **slow roll approximation**, where one term can be neglected in both (2.3) and (2.4). This leads to

$$H^2 \simeq \frac{8\pi}{3} V(\phi), \tag{2.7}$$

$$3H\dot{\phi} \simeq -V'(\phi), \tag{2.8}$$

that in literature is often expressed by the slow-roll parameters

$$\epsilon(\phi) = \frac{1}{16\pi}\left(\frac{V'}{V}\right)^2, \ll 1 \qquad |\eta(\phi)| = \frac{1}{8\pi}\frac{V''}{V} \ll 1. \tag{2.9}$$

The amount of inflation is usually expressed by the number of *e-foldings* N

$$N \equiv \ln\left(\frac{a(t_{\rm end})}{a(t_{\rm initial})}\right) = \int_{t_{\rm i}}^{t_{\rm e}} H dt \simeq -\int_{\phi_{\rm i}}^{\phi_{\rm e}} \frac{V}{V'} d\phi\,, \tag{2.10}$$

where in the last passage the slow roll approximation has been used.

2.2.4 Reheating: the end of inflation

During inflation all the content of the universe is enormously expanded and red shifted to very low density. To link the inflation expansion to the standard hot big bang one, suppose that the scalar field that has driven inflation decays into relativistic particles, with a conversion of the inflaton energy density into standard matter. This process takes places when the slow roll approximation breaks down and gives rise to oscillations of the inflaton on the bottom of the potential. The damping of these oscillations, that phenomenologically can be described as a harmonic oscillator, produces the decay of the field into conventional matter at very high temperature. Details on the topic of reheating can be found in [6, 13, 14] .

2.2.5 Perturbation production

The most important property of inflation is that it produces a spectrum of density perturbations and gravitational waves. The first can explain the formation of structures in the universe while the second plays an important role in the interpretation of the microwave anisotropies measured in the CMB signal ([6] and references within). For the purpose of this work we give attention just to the density perturbations.

The density perturbations derive from the quantum perturbations of the inflation field and to understand the mechanism we have to remember that perturbations on scales smaller than the Hubble length are causally connected and therefore interact by gravitational processes. On the other hand perturbation on scales larger than the Hubble length are frozen (the pressure gradients are negligible as we will see later in this chapter) and their evolution is determined just by the cosmological expansion. In the hot big bang model one has that initial super horizon scale perturbations grow smoothly until they cross the horizon and then they start to interact and eventually give raise to bound structures. During inflation one has just the opposite because initially perturbations of the scalar field are on sub horizon scales and can interact to solve the horizon problem. Later with the inflation expansion, that decreases the Hubble scale and maintains constant the comoving scales of perturbations, the perturbations cross outside the horizon and the causal physical interactions are stopped, leaving a spectrum of perturbations frozen into the Universe. These perturbations are created on very wide range of scales and the spectrum derived from the particular model of inflation specifies the scale distribution.

The nature of the initial perturbations of the scalar field ($\phi = \phi(t) + \delta\phi(\mathbf{x}, t)$) is explained by the Uncertainty Principle of quantum theory which ensures that one cannot avoid some irregularities. The scale of these irregularities depends on the energy scale at which inflation takes place. We will not enter into any details of the calculation of the vacuum fluctuation

of the scalar field, that can be found in [6], giving just the final result that relates the field perturbations to metric or curvature perturbations $\mathcal{R}$.

$$\boxed{\mathcal{R} = -\left[H\frac{\delta\phi}{\dot{\phi}}\right]_{t=t_*}} \tag{2.11}$$

The curvature perturbation $\mathcal{R}$ will be systematically defined later in section (2.4), where t_* is the initial time after inflation when the cosmological perturbations are introduced in the standard hot big bang universe.

2.3 Gaussian perturbations

For the aim of this work we are mainly interested to consider cosmological perturbations during the radiation dominated era, where the content of the universe is very well described as a one component perfect fluid. We need therefore to take into account the simplest types of cosmological perturbation, referred in literature as **Gaussian** and **adiabatic** perturbations. These are characterised by the assumption that the inflaton field has only one component which gives rise to a spectrum of perturbation with a spectral index close to 1 and to the important property that the spatial curvature is time independent on scales well outside the horizon. Another standard assumption is that there are no other important vacuum fluctuations of fields different from the inflaton that have significant effect after inflation. The property of $\mathcal{R}$ to be time independent allows the evolution of the density perturbations to be connected to the initial time t_* of perturbation production after inflation, when the right hand term of expression (2.11) is calculated.

2.3.1 Fourier description of Gaussian perturbations

In the analysis of vacuum fluctuations it is useful to describe them with Fourier expansion components in a comoving box characterised by a comoving length L

$$\delta\phi(\mathbf{r},t) = \sum_{\mathbf{k}} \delta\phi_{\mathbf{k}}(t)e^{i\mathbf{k}\cdot\mathbf{r}}, \tag{2.12}$$

where $\mathbf{r}$ is the comoving distance and the physical wavenumber is k/a ($\Delta k = 2\pi/L$). In this language the Gaussian property means that to a first approximation, the Fourier components of the vacuum fluctuations are uncorrelated. To understand better this aspect we have to consider the quantum description of the scalar field perturbations component $\phi_{\mathbf{k}}$, where these are composed of a real and imaginary part, each described as a harmonic oscillator, with a Gaussian probability distribution and no relation between them (Gaussian property). The variances of the probability distributions can be calculated from the inflation model and are independent of the direction $\mathbf{k}$ (stochastic property).

Now we apply the Fourier formalism to a generic perturbation $g(\mathbf{r},t)$

$$g(\mathbf{r},t) = \sum_{\mathbf{k}} g_{\mathbf{k}}(t)e^{i\mathbf{k}\cdot\mathbf{r}}, \tag{2.13}$$

where the single mode $g_{\mathbf{k}}$ is related to the primordial curvature perturbation using the transfer function $T_g(k,t)$ as

$$g_{\mathbf{k}}(t) = T_g(k,t)\mathcal{R}_{\mathbf{k}}\,, \tag{2.14}$$

and the curvature perturbation is fixed by the model of inflation used with expression (2.11).

The probability of finding the real part $R_{\mathbf{k}}$ of a generic perturbation mode $g_{\mathbf{k}}$ is

$$\mathbf{P}(R_{\mathbf{k}}) = \frac{1}{\sqrt{2\pi}\sigma_k}\exp\left(-\frac{R_{\mathbf{k}}^2}{2\sigma_k^2}\right) \tag{2.15}$$

where σ_k is the **dispersion** of $R_{\mathbf{k}}$ and the normalisation makes the total probability equal to 1 (The same relation holds for the imaginary part $I_{\mathbf{k}}$). A more convenient quantity is the **spectrum** $\mathcal{P}_g$ of generic perturbations $g_{\mathbf{k}}$, defined as

$$\mathcal{P}_g(k) \equiv \left(\frac{2\pi}{L}\right)^3 4\pi k^3\langle|g_{\mathbf{k}}|^2\rangle\,. \tag{2.16}$$

In the limit of large box size L, the Fourier series transforms into Fourier integrals and the fundamental transformation rule to be used is

$$\left(\frac{2\pi}{L}\right)^3\sum_{\mathbf{k}} \to \int d^3k \tag{2.17}$$

that gives

$$\left(\frac{L}{2\pi}\right)^3 g_{\mathbf{k}} \to \frac{1}{(2\pi)^{3/2}}\,g_{\mathbf{k}}\,. \tag{2.18}$$

Using the volume element $d^3k = 4\pi k^2 dk$ we can calculate the variance of the whole perturbation spectrum

$$\sigma_g^2(\mathbf{r}) \equiv \langle g^2(\mathbf{r})\rangle = \int_0^\infty \mathcal{P}_g(k)\frac{dk}{k}\,, \tag{2.19}$$

or alternatively

$$P_g \equiv L^3\langle|g_{\mathbf{k}}|^2\rangle = \frac{2\pi}{k^3}\mathcal{P}_g(k) \tag{2.20}$$

$$\sigma_g^2(\mathbf{r}) = \frac{1}{2\pi}\int_0^\infty P_g(k)k^2dk\,. \tag{2.21}$$

The generic perturbation $g(\mathbf{r})$ written as a Fourier series in (2.13) becomes a Fourier integral as

$$g(\mathbf{r}) = \frac{1}{(2\pi)^{3/2}}\int g(\mathbf{k})e^{i\mathbf{k}\cdot\mathbf{r}}d^3k \tag{2.22}$$

or

$$g(\mathbf{k}) = \frac{1}{(2\pi)^{3/2}}\int g(\mathbf{k})e^{-i\mathbf{k}\cdot\mathbf{r}}d^3r \tag{2.23}$$

and the probability distribution of $g(\mathbf{r})$ is Gaussian

$$P(g) = \frac{1}{\sqrt{2\pi}\sigma_g}\exp\left(-\frac{g^2}{2\sigma_g^2}\right)\,. \tag{2.24}$$

2.3.2 The window function

The integrals of (2.22) and (2.23) are not converging in the limit of large k because of the large number of structures on small scales. To get rid of this, one can use a smooth function called the **window function** W considering a smoothed new quantity $g(R, \mathbf{r})$ instead of $g(\mathbf{r})$

$$\mathrm{g}(R, \mathbf{r}) = \frac{1}{V} \int W(|\mathbf{r}' - \mathbf{r}|/R) g(\mathbf{r}') d^3 r' . \tag{2.25}$$

The physical property of the window function $W(y)$ is to weight the interaction of the nearby regions as a filter, reducing it rapidly when $y > 1$ and its volume is

$$V = \int W(r/R) d^3 r = 4\pi R^3 \int W(y) y^2 dy . \tag{2.26}$$

The exact choice of the window function is arbitrary, just as matter of convenience. Two simple choices frequently used are the *top hat* defined by $W = 1$ for $y \leq 1$ and $W = 0$ for $y > 1$, and *Gaussian* defined by $W(y) = \exp(-y^2/2)$.

The convolution theorem states that

$$g(R, \mathbf{k}) = W(kR) g(\mathbf{k}) \tag{2.27}$$

where $W(kR)$ is the Fourier transform of $W(r/R)/V$

$$W(kR) \equiv \frac{\int W(r/R) e^{i\mathbf{k}\cdot\mathbf{r}} d^3 r}{\int W(r/R) d^3 r} ; \tag{2.28}$$

and $g(\mathbf{k})$ is given by (2.23). For the top hat and Gaussian expressions for W, one can perform the integral of (2.28) analytically giving

$$W(kR) = 3 \left[\frac{\sin(kR)}{(kR)^3} - \frac{\cos(kR)}{(kR)^2} \right] \tag{2.29}$$

for the top hat, and

$$W(kR) = \exp\left(-\frac{k^2 R^2}{2} \right) \tag{2.30}$$

for the Gaussian. The filtering with the window function removes structures on scales $\lesssim R$ without affecting structure on much bigger scales. Applying the convolution theorem to the variance of g, we have

$$\langle g^2(R, \mathbf{r}) \rangle \equiv \sigma_g^2(r) = \int_0^\infty W^2(kR) \mathcal{P}_g(k) \frac{dk}{k} \tag{2.31}$$

and if $\mathcal{P}_g(k)$ is increasing with k, the function $W^2 \mathcal{P}_g$ has a maximum at $k_R \sim 1/R$, giving roughly

$$\sigma_g^2(R) \sim \mathcal{P}(k_R) . \tag{2.32}$$

Usually R is taken to be time independent, comoving with the expansion of the universe.

2.3.3 Spectrum of primordial curvature perturbation

The spectrum $\mathcal{P}_g$ is related to the primordial spectrum of curvature perturbations $\mathcal{P}_\mathcal{R}$, with the transfer function defined in (2.14), by

$$\mathcal{P}_g(t) = T_g(t)\mathcal{P}_\mathcal{R}. \tag{2.33}$$

The possibility to calculate the primordial spectrum of curvature perturbations is important for all of the subsequent comparisons of the model with observations. Applying the slow roll approximation (see (2.11)) one has

$$\mathcal{P}_\mathcal{R} = \left[\left(\frac{H}{\dot{\phi}}\right)^2 \mathcal{P}_\phi(k)\right]_{t=t_*} \tag{2.34}$$

where the primordial time t_* corresponds a few Hubble times after the time of horizon exit given by $k = aH$. An important result of free field vacuum fluctuations (see [6] for derivation), using a massless scalar field, is that after a few Hubble times after horizon exit the vacuum fluctuations settle down to a constant value and their spectrum is simply given by

$$\mathcal{P}_\phi(k) = \left(\frac{H}{2\pi}\right)_{k=aH}. \tag{2.35}$$

Inserting this expression in (2.33) one gets the spectrum of the primordial curvature perturbations

$$\mathcal{P}(k) = \left[\left(\frac{H}{\dot{\phi}}\right)\left(\frac{H}{2\pi}\right)\right]^2_{t=t_*}, \tag{2.36}$$

where the term $(H/\dot{\phi})$ can be calculated at horizon exit $k = aH$ instead of at t_*, because in the slow roll approximation the variation of the scaler field with time given by $\dot{\phi}$ is negligible during a few horizon time scales.

This last expression applied to most of the inflation models gives a simple power law for the primordial perturbation spectrum of curvature

$$\mathcal{P}_\mathcal{R}(k) \propto k^{n-1}, \tag{2.37}$$

where the constant n is the **spectral index**, and the value $n = 1$ gives the scale invariant Harrison-Zel'dovich spectrum [15, 16]. We now understand that having observational constraints on the value of n permits us to get observational constraints on inflation.

For future application of the power spectrum one should notice that (2.37) implies that the spectrum of the density contrast $P_\delta(k)$, with $\delta \equiv \delta e/e_b$, becomes

$$P_\delta(k) \propto k^n \tag{2.38}$$

on scales well outside the horizon.

2.4 Linear theory of cosmological perturbations

In the linear theory of cosmological perturbations one intends to study analytically the evolution of small perturbations away from homogeneity and isotropy. When the scales of a perturbation is well within the horizon it is possible in good approximation to use Newtonian theory, while when the scale is outside one need to use general relativity. We give attention mainly to the relativistic approach that is converging to the Newtonian treatment if the perturbation is within the horizon.

The results presented in this thesis have been obtained in spherical symmetry with a perfect fluid, and therefore we have neglected in the following parts of this chapter the discussion of possible non spherical effects.

The linear approximation evolution is described by a set of coupled linear partial differential equations because the derivatives are with respect space and time. To simplify these features it is useful to use the Fourier expansion of the equations, because the background quantities are just functions of time. We then obtain a set of coupled ordinary differential equations, containing only time derivatives, that the Fourier coefficients of the perturbation have to satisfy for each $\mathbf{k}$. This simplification is possible because, as we have just said previously, there is no coupling between different modes for Gaussian perturbations.

An important problem arising in general relativity is how to choose a coordinate system and if there is a preferred one. In the case of an unperturbed universe, the choice is natural because we have a set of comoving fundamental observers perfectly synchronised, that do not observe any velocity field at their own position. It is then intuitive to consider an orthogonal slicing of the space time along the world lines of each comoving observer, because on every slice the universe is homogeneous.

Introducing perturbations, it is no longer possible to a have a preferred coordinate system because the properties deriving from homogeneity and isotropy are lost. One is therefore free to chose any possible coordinate system, with the only requirement being that it converges to the standard one in the limit of vanishing perturbations. A choice of coordinate with this constraint is called a **Gauge** choice, but now there is not a unique preferred possibility. For the purpose of describing cosmological perturbations a useful choice is the **comoving slicing**, orthogonal to the worldlines of comoving observers, where the space and time coordinates are regarded as those of the unperturbed slicing, because taking into account their perturbations is a second order effect. This slicing is also useful for the definition of perturbations of curvature $\mathcal{R}$ given in the following.

2.4.1 Metric Perturbations

In (1.7) we have defined the FRW metric of the unperturbed universe in different gauges. Taking as background metric the spatially flat one with $K = 0$, we perturb it using the conformal time form (1.2) in the spherically symmetric case.

$$ds^2 = a^2(\tau)\left[-(1+2A)d\tau^2 + (1+2D)\delta_{ij}dx_i dx_j\right] \tag{2.39}$$

with $A, D \ll 1$. The term A is the **lapse function** which gives the transformation between the conformal time and the proper time.

$$\frac{dt_{\rm pr}}{d\tau} = \sqrt{1+2A} \simeq 1 + A\,. \tag{2.40}$$

The meaning of D is directly linked to curvature and we can see this using the definition of the Ricci Tensor to calculate the corresponding three curvature

$$R^{(3)} = 4\frac{k^2}{a^2}D\,. \tag{2.41}$$

Using this expression we can now define properly the curvature perturbation $\mathcal{R} \equiv D$ as the **comoving perturbation curvature** on the comoving slice, which is equivalent to saying that

$$R^{(3)} = 4\frac{k^2}{a^2}\mathcal{R}\,. \tag{2.42}$$

We have just mentioned previously that this quantity is time independent at first order when the perturbation is outside the horizon. In the following we will understand clearly how to derive this statement when we see how $\mathcal{R}$ relates to the evolution equations.

2.4.2 Evolution equations

The hydrodynamical variables appearing in the energy momentum tensor for a perfect fluid are just energy density and pressure. We need to specify the perturbation of the velocity field of our density perturbations in relation to the Hubble parameter appearing in the Friedmann and acceleration equations. Therefore we will define a variable local Hubble parameter $H(r,t)$, which is equivalent to giving a peculiar velocity to the comoving elements of the fluid.

$$e(r,t) = e_b(t) + \delta e(r,t) \tag{2.43}$$

$$p(r,t) = p_b(t) + \delta p(r,t) \tag{2.44}$$

$$H(r,t) = H_b(t) + \delta H(r,t) \tag{2.45}$$

To begin, consider the general relativistic form of the continuity and acceleration equations:

$$\frac{de}{dt_{\rm pr}} = 3H(e+p)\,, \tag{2.46}$$

$$\frac{dH}{dt_{\rm pr}} = -H^2 - \frac{4\pi}{3}(e+3p) + \frac{1}{3}\frac{\nabla^2 p}{(e+p)} \tag{2.47}$$

where the last term of (1.15) has been obtained using the Euler equation. These equations are written with respect the proper time $t_{\rm pr}$, where $dt_{\rm pr}$ is the proper time increment along a comoving worldline. We need now to recast the derivatives of these equations with respect the time coordinate t of the comoving slicing. Using (see [7])

$$\frac{dt_{\rm pr}}{dt} = 1 - \frac{\delta p}{e+p}\,, \tag{2.48}$$

one gets the final form of the differential equations to solve,

$$\delta\dot{e} = -3(e+p)\delta H - 3H\delta e \tag{2.49}$$

$$\delta\dot{H} = -2H\delta H - \frac{4\pi}{3}\delta e - \frac{1}{3}\frac{\nabla^2\delta p}{(e+p)} \tag{2.50}$$

where the overdot denotes $\partial/\partial t$ at fixed r. As we shall see in the next section these expressions can be applied also in the limit of Newtonian theory to calculate the density evolution of perturbations inside the horizon.

In Newtonian gravity, the gravitational effects are described by the **Poisson equation**[1]

$$\nabla^2\Phi_{\rm gr} = 4\pi e \tag{2.51}$$

where $\Phi_{\rm gr}$ is the gravitational potential that in a spherically symmetric unperturbed universe is equal to $2\pi a^2 r^2 e/3$. Introducing a perturbation one has

$$\Phi_{\rm gr}(r,t) = \frac{2\pi}{3}e_b + \Phi(r,t) \tag{2.52}$$

where Φ corresponds to an analogous relativistic quantity called the **peculiar gravitational potential**, that appears in the perturbed Poisson equation

$$\nabla^2\Phi = 4\pi\delta e\,. \tag{2.53}$$

To get rid of the spatial gradient it is useful to write each quantity as a Fourier series as in (2.12), which means that, for each $\mathbf{k}$, one can replace

$$\nabla \to i\frac{\mathbf{k}}{a}, \qquad \nabla^2 \to -\left(\frac{k}{a}\right)^2. \tag{2.54}$$

It is useful for the following to define the **adimensional density contrast** $\delta \equiv \delta e/e$ and we can see that (2.53) can be written using Fourier expansion as

$$\delta_{\mathbf{k}} = -\frac{2}{3}\Omega\left(\frac{k}{aH}\right)^2\Phi_{\mathbf{k}}\,, \tag{2.55}$$

where we have taken into account the possibility of having a universe with $\Omega \neq 1$.

2.4.3 The evolution of density perturbations

Now we calculate the time evolution of energy density perturbation solving the system of equations (2.49) and (2.50). The first step is to insert the equation of state $p = \gamma e$ into the continuity equation to write it as function of the adimensional density contrast $\delta = (\delta e/e)$,

$$\delta H = -\frac{1}{3(1+\gamma)}\left[\dot{\delta} - 3H\gamma\delta\right]. \tag{2.56}$$

[1]Usually the Poisson equation is written with density ρ instead of energy density e. Instead in this thesis we have made the perhaps unusual choice in cosmology of using e instead of ρ as it is used later in the hydrodynamical equations. The two quantities can anyway be identified as the same, in fact $e = \rho c^2$ and in our notation $c = 1$.

In the general case of $\gamma = \gamma(t)$ one has

$$\delta p = v^2 \delta e\,, \qquad \dot{\gamma} = 3H(\gamma - v^2)(1+\gamma) \tag{2.57}$$

where v is the general sound speed that converges to the simple case of $\gamma = v^2$ when γ is a constant as in the case of the radiation or matter dominated epochs. Substituting these definitions also into (2.50) one gets

$$\delta\dot{H} = -\frac{1}{3(1+\gamma)}\left[\ddot{\delta} - 3H(2\gamma - v^2)\dot{\delta} + \frac{9}{2}H(2v^2 + \gamma^2 - \gamma)\delta\right], \tag{2.58}$$

and combining the two equations one gets finally the **perturbation equation**

$$\ddot{\delta} + H\left[2 - 3(2\gamma - v^2)\right] - \frac{3}{2}H\left(1 - 6v^2 - 3\gamma^2 + 8\gamma\right) = v^2\nabla^2\delta\,. \tag{2.59}$$

This important equation allows us to calculate the amplitude evolution of each mode $\delta_{\rm k}$ using the replacement $\nabla^2\delta_{\rm k} = -(k/a)^2\delta_{\rm k}$.

One can solve this equation changing the independent variable from t to a, by

$$\frac{d}{dt} = \dot{a}\frac{d}{da} = H_b a\frac{d}{da}\,, \qquad \dot{H}_b = -\frac{3}{2}(1+\gamma)H_b^2 \tag{2.60}$$

and the perturbation equation becomes

$$a^2\frac{d^2\delta_{\rm k}}{da^2} + Aa\frac{d\delta_{\rm k}}{da} + \left(B + \frac{k^2v^2}{H^2a^2}\right)\delta_{\rm k} = 0\,, \tag{2.61}$$

where

$$A = \frac{3}{2}\left(1 - 5\gamma + 2v^2\right), \qquad B = \frac{3}{2}\left(1 - 6v^2 + 8\gamma - 3\gamma^2\right). \tag{2.62}$$

In the radiative epoch $\gamma = v^2 = (1/3)$ and one gets

$$a^2\frac{d^2\delta_{\rm k}}{da^2} + \left(\frac{k^2}{3H^2a^2} - 2\right)\delta_{\rm k} = 0\,. \tag{2.63}$$

When the k-mode is well outside the horizon, the term $(k^2/3Ha^2) \ll 1$ can be neglected, and this equation has two independent simple solutions:

$$\delta_1 \propto a^2 \propto t, \qquad \delta_2 \propto a^{-1} \propto t^{-1/2}\,. \tag{2.64}$$

that in general combine linearly into the general solution $\delta = c_1\delta_1 + c_2\delta_2$. The first mode δ_1 represents the growing mode solution, corresponding to the adiabatic component of the perturbation (we will better understand this point later), while δ_2 is the decaying mode component. If the k-mode is well inside the horizon $(k^2/3Ha^2) \gg 1$ and we have that the solution is a plane wave that oscillates rapidly, given by

$$\delta \propto \exp\left(i\frac{k}{\sqrt{3}Ha^2}\right). \tag{2.65}$$

In the matter dominated epoch we can set $\gamma = v^2 = 0$ in the definitions of the coefficients A and B; $v \ll 1$ is the sound speed c_s for a non relativistic fluid,

$$a^2 \frac{d^2\delta_k}{da^2} + \frac{3}{2} a \frac{d\delta_k}{da} + \left(\frac{k^2 c_s^2}{H^2 a^2} - \frac{3}{2} \right) \delta_k = 0 . \tag{2.66}$$

This equation corresponds to the Newtonian treatment of gravity, where the role of the Hubble horizon is replaced by the **Jeans length** λ_J, given by

$$\lambda_J = \frac{2\pi c_s}{\sqrt{4\pi e}} . \tag{2.67}$$

If the wavelength of the **k**-mode is larger than the Jeans length, the term $(k^2 c_s^2 / H a^2) \ll 1$ can be neglected, and this equation has a growing and decaying mode component as in the relativistic case, that behave as

$$\delta_1 \propto a \propto t^{2/3}, \qquad \delta_2 \propto a^{-3/2} \propto t^{-1} . \tag{2.68}$$

If the wavelength of the **k**-mode is smaller than the Jeans length the term $(k^2 c_s^2 / H a^2) \gg 1$ dominates inside the parenthesis and the solution of the equation has an oscillating behaviour, giving raise to **acoustic oscillations** of the matter.

The presence of two different modes in the general solution of the perturbation equations is related to the fact that the perturbation equation is a second order differential equation with two degrees of freedom. Physically this means that there is no direct coupling in the initial conditions between the energy density distribution and the velocity field. The decaying mode component represents the uncoupled component of the initial condition that is soon dispersed during perturbation evolution.

2.4.4 Adiabatic Condition

At beginning of section 2.3 we have made the assumption that the inflation field has only one component, and that eventual vacuum fluctuations of other fields have no significant effect after inflation. These assumptions are fundamental for proving that $\mathcal{R}$ is time independent on scales well outside the horizon.

A way to understand this argument better is to consider the whole universe on super horizon scales as being separated into different regions that evolve like separate FRW universes where the vacuum fluctuations determines the difference between the locally measured proper times. At horizon entry, when these regions become causally connected, the difference in proper times corresponds to a difference in density of the regions, thus giving density perturbations, because each region has evolved differently. In other words, if the perturbation is on a scale well outside the horizon, it is possible to divide this scale into different regions such that in each one the universe can be seen as unperturbed, looking therefore identical if their clocks are synchronised on scales of constant ϕ a few Hubble times after horizon exit during inflation.

Entering more into details of this aspect is beyond the aim of this thesis and it is very well analysed in [6]. It is however important to say that these properties lead to an important

relation called the **generalised adiabatic condition**, that for each Fourier mode well outside the horizon is

$$\frac{\delta g_{\mathbf{k}}}{\dot{g}} = \frac{\delta e_{\mathbf{k}}}{\dot{e}}. \tag{2.69}$$

This can be written in a form to relate the density perturbation of each particular species of particles to the density perturbation of the total matter of the universe. If g is the density e_i of a particular species, applying to each species the continuity equation $e_i = -3H(e_i + \mathrm{p}_i)$ one gets

$$\frac{1}{1+p_i/e_i}\delta_i = \frac{1}{1+p/e}\delta, \tag{2.70}$$

that gives

$$\delta_i = \delta \qquad \text{(radiation)} \tag{2.71}$$

$$\delta_i = \tfrac{3}{4}\delta \qquad \text{(matter)} \tag{2.72}$$

Identifying g as the total pressure in (2.69) one obtains that

$$\frac{\delta p_k}{\dot{p}} = \frac{\delta e_k}{\dot{e}}, \tag{2.73}$$

and this expression allows one to show the time independence of curvature perturbation $\mathcal{R}_k$.

2.4.5 The Curvature perturbation

Finally we can relate the curvature perturbation $\mathcal{R}$ to the density perturbation and see that on scales well outside the horizon $\mathcal{R}$ is time independent. To simplify we consider just the case of critical density corresponding to $K = 0$.

An equivalent definition of $\mathcal{R}$ seen in (2.42) appears in the local Friedmann equations,

$$H(r,t) = \frac{8\pi}{3}e(r,t) + \frac{2}{3}\nabla^2\mathcal{R}(r,t) \tag{2.74}$$

that is equivalent to perturbing the constant K appearing in the Friedmann equation as

$$\delta K = \frac{2}{3}a^2\nabla^2\mathcal{R}, \qquad \delta K_{\mathbf{k}} = -\frac{2}{3}k^2\mathcal{R} \tag{2.75}$$

Now, if we consider equation (2.50) with $\delta p = 0$, we can see that, together with the continuity equation we obtain an expression equivalent to (2.74) with δK being time independent. In fact if we multiply (2.74) by a^2, take the time derivative and use the continuity and acceleration equation, we get

$$\dot{\mathcal{R}}_{\mathbf{k}} = -H\frac{\delta p_k}{e+p}. \tag{2.76}$$

The physical statement now looks clear: *on a sufficiently large scale well outside the horizon the pressure gradients are negligible and therefore the curvature perturbation is constant in time.* To complete the proof we still need to show that $\delta p_{\mathbf{k}} \ll \mathcal{R}_{\mathbf{k}}$, and to start we can rewrite

equation (2.74) using the definition of the peculiar gravitational potential $\Phi_{\rm k}$ seen in (2.52) and the the equation of state $p = \gamma e$, obtaining the time variation of $\mathcal{R}_{\rm k}$,

$$\frac{1}{H}\frac{\partial \mathcal{R}_{\rm k}}{\partial t} = \frac{2}{3}\frac{\delta p_{\rm k}}{\delta e_{\rm k}}\left[\left(\frac{k}{aH}\right)^2 \frac{\Phi_{\rm k}}{(1+\gamma)\mathcal{R}_{\rm k}}\right]. \tag{2.77}$$

Using the adiabatic condition (2.69), that implies that $|\delta p_{\rm k}/\delta e_k| \sim 1$ at any scale well outside the horizon, we see clearly that the time dependence of $\mathcal{R}_{\rm k}$ is negligible far outside the horizon, when $(k/aH)^2 \ll 1$, provided that $|\Phi_{\rm k}| \sim |\mathcal{R}_{\rm k}|$.

To prove this last condition we consider the local Friedmann equation 2.74 for the perturbed quantities

$$2H\delta H_{\rm k} = \frac{8\pi}{3}\delta e_{\rm k} - \frac{2}{3}\left(\frac{k}{a}\right)^2 \mathcal{R}_{\rm k}\,, \tag{2.78}$$

to eliminate $\delta H_{\rm k}$ in (2.49), and obtain

$$\frac{1}{H}\dot{\Phi}_{\rm k} + \frac{5+3\gamma}{2}\Phi_{\rm k} = -(1+\gamma)\mathcal{R}_{\rm k} \tag{2.79}$$

The solution of this equation has the growing solution

$$\Phi_{\rm k} = -\frac{3(1+\gamma)}{5+3\gamma}\mathcal{R}_{\rm k}\,, \tag{2.80}$$

showing that $\Phi_{\rm k}$ and $\mathcal{R}_{\rm k}$ are of the same order.

The definition of the peculiar gravitational potential gives the relation between the density and curvature perturbations corresponding to a pure growing mode, obtaining

$$\delta_{\rm k} = \frac{2(1+\gamma)}{5+3\gamma}\left(\frac{k}{aH}\right)^2 \mathcal{R}_{\rm k}\,. \tag{2.81}$$

Before ending this chapter we want to stress again that the result of the curvature perturbation being constant is working as a consequence of the adiabatic condition of Gaussian perturbations, with the additional assumption that there is only one degree of freedom, and this corresponds to a pure growing mode solution of the perturbation equation.

Chapter 3

Primordial black holes in the Universe

This chapter reviews the main ideas of PBH formation, from the initial landmark papers appearing in the seventies until the last years. In the first introductory section we synthetically introduce the general idea of what a black hole is. In the second section we discuss the idea of PBHs starting from a historical perspective about their possible formation, taking into account particularly the results of the numerical studies developed in the past. In the third section we analyse the idea of PBHs from a cosmological point of view, pointing out the main aspects where the possible presence of PBHs plays an interesting role (the structure of this section has been mainly based on the recent review by Carr [17]). Finally we present some summarising conclusions pointing out some open questions that arise and that we have tried to address in the following chapters.

Naturally we cannot be exhaustive with all the literature produced on the topic during about 35 years. This chapter is therefore our personal perspective of the argument, where we have tried to be sufficiently exhaustive in mentioning different references related the topic of PBHs.

3.1 An introduction to Black Holes

A possible definition of a Black Hole is *a portion of space-time where there is a singularity "hidden" behind a surface called an* **event horizon**. *The event horizon makes all information coming from inside invisible to an outside observer, creating a* **trapped surface** *that it is possible to cross inward but is impossible to escape from outward.* To complete this definition we need to specify the concept of singularity as a region of the space time where our measure of curvature (Riemann tensor) diverge, stopping any further physical analysis. A more rigorous and complete definition can be found in [18].

The simplest solution describing a black hole is the Schwarzschild metric that can represent the empty space time around a spherical mass M collapsed in a central singularity. The metric

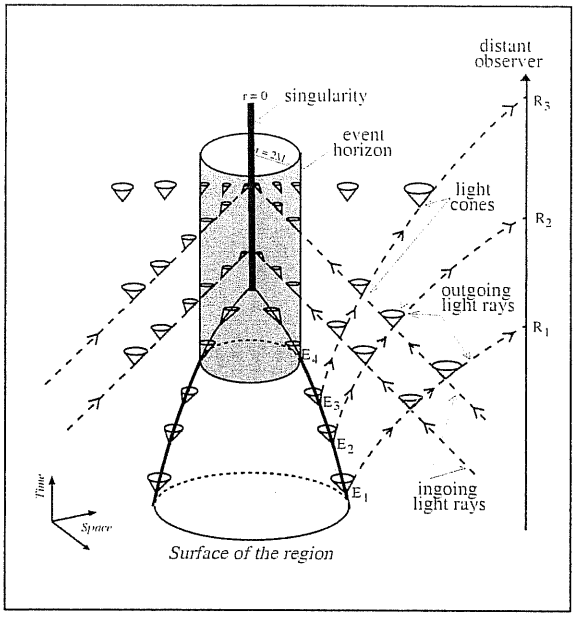

Figure 3.1: Space time diagram for a black hole formation due to the collapse of a spherical region. The figure has been taken from [19]

explains how the space time is "curved" around the centre,

$$ds^2 = -\left(1 - \frac{2M}{R}\right) dt^2 + \left(1 - \frac{2M}{R}\right)^{-1} dR^2 + R^2 d\Omega^2 . \tag{3.1}$$

Looking at the Schwarzschild metric one can see two different singularities, one is at the event horizon at $R = 2M$, the other is in the centre, at $R = 0$. The first is a coordinate singularity that can be eliminated with a coordinate transformation and this implies that nothing special happens to a test particle that crosses that point. The nature of the central singularity is different, this is in fact a genuine singularity that cannot be eliminated with any coordinate transformation.

The coordinate singularity of the Schwarzschild metric represents the **event horizon** and in figure 3.1 one can see a space time diagram of a black hole formed from a spherical gravitational collapse. The meaning of the event horizon can be seen looking at the angles of the light cones that do not allow particles to escape if $R \leq 2M$; such particles are then obliged to fall into the singularity.

An important measurable effect of the curved metric around a black hole is the difference in the lapse (the g_{00} component of the metric tensor) measured by a comoving observer moving toward the singularity and another one far away outside the hole. The first observer will measure a finite proper time of the collapse without noticing special features of the space time when he is crossing the event horizon. The second observer will instead see the first one approaching the event horizon in an infinite amount of time, because of information from the first observer becoming infinitely red shifted.

3.2 Primordial black hole formation

3.2.1 Historical Overview

Many years ago it was realised that the high density associated with the early universe can lead to the formation of black holes with a wide range of masses. It has been shown in (1.36) that the relation between the Hubble horizon mass and the Hubble radius is the same that relates the event horizon radius and the mass of the black hole. The reason for this analogy is because both surfaces are trapped surfaces. More precisely *a black hole event horizon is the asymptotic location of the outermost trapped surface for outgoing light-rays* whereas the cosmological horizon is the innermost trapped surface for incoming light rays.

Comparing the density of the early universe at a certain time t with the density associated with a black hole of mass M, one can see that PBHs would have the mass of the order of the horizon mass at their formation epoch.

$$M_H = 2t \simeq 10^{15} \left(\frac{t}{10^{-23}\ \mathrm{s}} \right) \mathrm{g}\,. \tag{3.2}$$

The mass range of PBHs goes from very small values as such the Planck mass (10^{-5} g) for holes formed at the Planck scale up to such large values as for those formed at Nucleosynthesys (1 s), of the order of $10^5\ M_\odot$. Although expression (3.2) was first derived by Zeldovich & Novikov [20] they were not really considering black holes but a kind of "retarded core". They were arguing anyway that the presence of these objects should be very unlikely because they pointed out they would be characterised by a catastrophically accretion [20]. The idea was based on a Newtonian argument that allows these objects to grow at the same rate of the horizon through all the radiation dominated epoch, reaching the horizon mass of $10^{15}\ M_\odot$ at the end of this era

.

Two years later Hawking [1] was the first to really realise that primordial density perturbations in the universe might lead to formation of PBH of the order of the horizon mass by gravitational collapse in the radiation dominated epoch. A few years later together with Carr he disproved the argument of catastrophic accretion, pointing out that Zeldovich & Novikov had neglected the cosmological expansion. More precisely they demonstrated that there is no spherically symmetric similarity solution which represents a black hole attached to an exact Friedmann model via a sound wave [2]. The conclusion was that after formation PBHs become soon much smaller than the cosmological horizon, with negligible accretion.

The possibility of the real existence of PBHs stimulated Hawking to study their quantum properties leading to the famous discovery of evaporation: black holes emit a spectrum of thermal radiation as a blackbody with a temperature related to the mass of the hole,

$$T = \frac{1}{8\pi G} \sim 10^{-7} \left(\frac{M}{M_\odot} \right)^{-1} K. \tag{3.3}$$

The evaporation rate is to first approximation proportional to the inverse of the mass squared

$$\frac{dM}{dt} \propto -\frac{1}{M^2}\,, \tag{3.4}$$

giving a timescale for the evaporation of

$$\tau(M) \propto M^3 \sim 10^{64} \left(\frac{M}{M_\odot}\right)^3 y\,. \tag{3.5}$$

This means that black holes with a mass larger than 10^{15} g would evaporate in a timescale longer than the age of the universe at the present moment, making the effect completely negligible. The final state of this process is still unclear, because at that stage a complete quantum theory is needed. One possibility is to have a final explosion that would disperse all of the mass but a more interesting option from the point of view of PBHs is a final stable remnant of the order of Planck mass (see section 3.3).

We will see in the next section that the Hawking effect for possible PBHs with such small masses imposes strong constraints on their possible existence. During the evaporation in fact there is the emission of photons with energies of 100 Mev at the present epoch and the observational limits on the γ-ray background gives a present density of such PBHs of 10^{-8} times the critical density. The possibility to detect them seems therefore unlikely but nevertheless the PBH evaporation could still have interesting cosmological consequences changing many processes in the early universe [21]. For example there is a possibility to modify standard nucleosynthesis [22, 23] or to induce the reionisatioin of the universe [24] just to mention few of them (see for example [17] for a more extended description).

Subsequently the attention on PBHs moved to other mechanisms of formation, for example during phase transitions that might have happened in the early universe. It was proposed that the gravitational collapse of primordial perturbations could be enhanced during some phase transitions leading to an increment of PBH formation at some particular scales (See section 3.3). Other mechanisms of formation investigated have considered more exotic scenarios like bubble collisions [25, 26, 27] and formation of compact cosmic string loops [28, 29, 30, 31, 32].

3.2.2 Formation mechanism

The first attempt to get a quantitative estimation of the amplitude required for a cosmological perturbation to form a PBH was made by Carr in 1975 [33]. The idea was that the cosmological perturbation must be able to overcome the pressure support of radiation ($\gamma = 1/3$) but also not to be so large as to create a topologically disconnected region, larger than the horizon. This implies that the length scale of the perturbation at the moment of maximum expansion should be less than that of the horizon and larger than the Jeans length

$$\sqrt{\gamma} R_H \lesssim R \lesssim R_H\,. \tag{3.6}$$

Expressing the length scale as function of the perturbation amplitude $\delta = \delta e/e_b$ one gets, in the radiation dominated epoch,

$$\delta_c \lesssim \delta \lesssim 1, \tag{3.7}$$

with $\delta_c = 1/3$, and a mass of the hole is of the order of the horizon mass. Naturally this was just a first attempt to get an idea of the orders of magnitude involved, in order to make some

cosmological estimations about the distribution of these objects. A more refined calculation needs a numerical analysis of the relativistic effects of the gravitational collapse.

Nadezhin, Novikov & Polnarev in 1978 [34] carried out the first detailed numerical study of PBH formation using a hydrodynamical computer code similar to those of May & White (1966) [35] and Podurets (1964) [36] using a "cosmic-time" coordinate with a diagonal metric which reduces to a form similar to that of the FRW metric in the absence of perturbations. A well-known difficulty with this approach is that in a continuing collapse, singularities typically appear rather quickly and stop the computation before the black hole formation is complete. In [34], this difficulty was overcome by using an early form of excision with the evolution being stopped in the region where the singularity would appear.

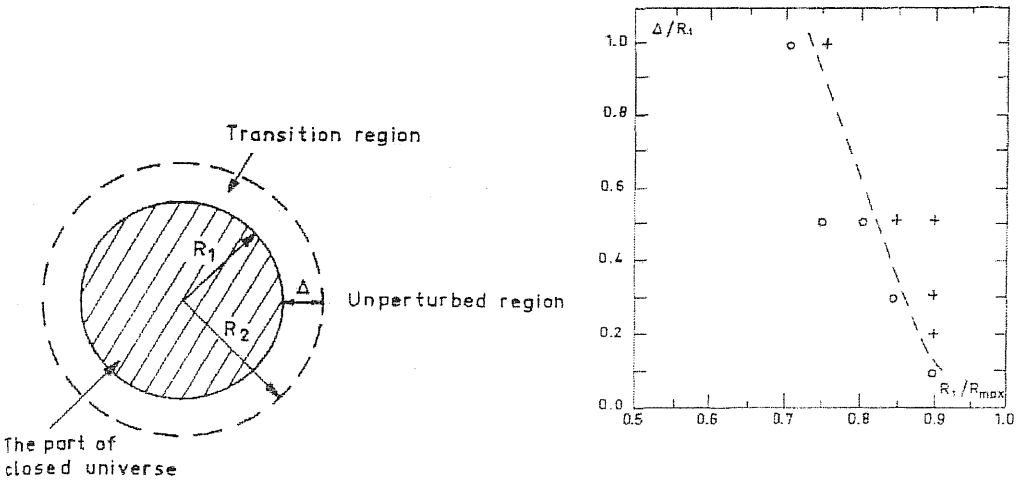

Figure 3.2: These figures have been taken by the paper of Nadezhin, Novikov & Polnarev [34]. The first shows schematically how they were describing the initial conditions: they were working with a prescription that uses curvature, having a closed Universe in the region of radius R_1, a flat universe outside region of radius R_2 and a transition region of amplitude Δ. The second figure shows the values of parameters that they found to give black hole formation. In this second plot $R_{\max}$ is corresponding to R_2 of the first diagram.

As initial conditions Nadezhin, Novikov & Polnarev considered a spherical region of radius R_1 described as a FRW universe with $K = 1$, and connected it to a spatially flat universe with $K = 0$ at a radius $R_2 > R_1$, having a transition region of amplitude Δ (see figure 3.2). The idea was of specifying initial conditions in this way was to describe the pressure gradients growing with decreasing of Δ/R_1, and the amplitude of the perturbation growing with R_1.

Their result are summarised in figure 3.2 where the region of parameters that allow PBH formation is shown and, as one can intuitively argue, high pressure gradients make formation of PBHs more difficult. The qualitative features of the earlier picture therefore were basically confirmed but it was found that the PBH masses were always much smaller than the horizon mass.

Shortly afterwards, Bicknell & Henriksen (1979) [37] carried out related calculations using a

method based on integration along hydrodynamical characteristics which avoids the problems associated with the appearance of singularities. They used rather different initial data from that of [34] and found formation of black holes with masses of the same order as the horizon mass (or greater in cases where the overdensity in the initial perturbation was not compensated by a surrounding under-dense region). They noted the appearance of both ingoing and outgoing compression waves during evolutions leading to black hole formation.

Twenty years later Niemeyer & Jedamzik [38, 39] made further numerical calculations, reformulating the problem and pointing out some new features. Historically this work has been crucial for us because we started to be interested in the problem shortly after the outcome of this work and we have used it as a starting point to develop our contribution. A detailed description of their results will therefore be given in the next chapter when we start to present our personal results. The main contribution of Niemeyer & Jedamzik was to point out the relevance of scaling-laws for PBH formation. They found that the black hole mass M_{BH} follows a power law in $(\delta - \delta_c)$ when the latter is sufficiently small, which is a similar behaviour to that seen in critical collapse by Choptuik [40] and many subsequent authors (see the review by Gundlach [41]). The specific expression is

$$M_{\rm BH} \propto (\delta - \delta_c)^{\gamma} M_H \quad \text{if} \quad (\delta - \delta_c) \ll 1 , \tag{3.8}$$

where γ is a characteristic parameter of scaling law behaviour [41]. Niemeyer & Jedamzik started from initial perturbations specified at the moment when the overdensity enters the horizon and then computed the subsequent evolution obtaining $\delta_c \gtrsim 0.7$ for each of the three types of perturbation profile which they studied.

While Niemeyer & Jedamzik [39] demonstrated the existence of a scaling law for PBH masses down to around one tenth of the horizon mass, they did not investigate smaller masses and so it was not possible to determine whether the scaling law was likely to continue down to vanishingly small masses (when $\delta \to \delta_c$) as in type II critical collapse [41]. In fact, the calculations become very challenging from a numerical point of view when δ is very close to δ_c because of the appearance of strong shocks and deep voids outside the region where the PBH is forming. Hawke & Stewart (2002) [42] addressed this problem using a sophisticated purpose-built code which allowed them to make calculations for values of δ closer to δ_c and to handle the strong shocks which occur in these cases. They found that the scaling law does *not* continue down to very small values of $(\delta - \delta_c)$ but rather reaches a minimum value for M_{BH} around 10^{-4} of the horizon mass, with the limit resulting from the behaviour of the shocks produced in nearly critical collapse.

We need to point out at this stage that the horizon mass normalisation used by Hawke & Stewart [42] is not the same as that used by Niemeyer and Jedamzik [39], because in the first case the initial conditions were imposed well within the horizon, while in the second case they are imposed exactly at the horizon crossing time and the horizon mass used for normalisation is that at the initial time in each case. This means that the results of these two papers cannot be compared straightforwardly without taking into account the different scales of normalisation. We will come back to this in chapter 6, when we investigate with our formulation the problem of a possible minimum mass in the scaling law.

Finally, almost contemporary with Niemeyer & Jedamzik Shibata & Sasaki (1999), [44] presented an alternative formalism for studying the problem of PBH formation, using constant mean curvature time slicing and focusing on metric perturbations rather than density perturbations. A key point that they emphasised is the importance of using initial data which can be directly related to perturbations arising from inflation. Their formulation was not restricted to spherical symmetry (as had been the case for the previous authors mentioned here) but they presented results only from spherical calculations. They located the threshold perturbation amplitude for PBH formation (in terms of the metric perturbation) and found that this varied considerably depending on the density of the medium surrounding the density peak. They concluded from this that it is probably important to take into account spatial correlations of density fluctuations when considering PBH formation.

It is not straightforward to make the link between results from this last type of calculation and ones from the more standard approach focused on density fluctuations. However, this was addressed in a recent paper by Green et al. (2004) [43]. They calculated the PBH abundance produced from two different fluctuation spectra, using peaks theory together with the threshold criterion of Shibata & Sasaki [44]. They then compared the results of this with ones obtained from a standard calculation based on a Press-Schechter-like approach and using density perturbations. They found that the Shibata & Sasaki results are consistent with ones using a density perturbation if δ_c lies in the range $0.3 \lesssim \delta_c \lesssim 0.5$ and, as they pointed out, there is an evident discrepancy with the result of $\delta_c \gtrsim 0.7$ [39].

3.3 Cosmological consequences and constraints of PBH

3.3.1 PBH and the spectrum of cosmological perturbations

Following the formalism defined in the previous chapter applied to the distribution of PBHs [45] one can define the initial mass fraction β_i of PBHs, given by the fraction of the universe satisfying equation (3.7),

$$\beta_i \equiv \frac{\rho_{\mathrm{PBH,i}}}{\rho_{\mathrm{tot,i}}} = \int_{1/3}^{1} P(\delta) d\delta \tag{3.9}$$

where $P(\delta)$ is the probability distribution for δ. For the lower limit of the integral we have put the "primordial" estimation of Carr as is often done in the literature. The debate about a more refined value is still open so, for the moment, we follow the main literature in using $\delta_c = 1/3$, keeping in mind that the value of δ_c is an open question.

Assuming a Gaussian distribution of primordial perturbations, as described in Chapter 2, one defines the mass variance $\sigma^2(M)$ of the probability distribution as explained in the previous chapter

$$\sigma^2(M) = \frac{1}{2\pi} \int_0^\infty \mathcal{P}(K) W(kR^2) k^2 dk\,, \tag{3.10}$$

usually evaluated at horizon crossing. Usually the power spectrum $\mathcal{P}(k)$ used is the power law

form of (2.37), and the mass fraction of PBHs is given by

$$\beta(M) = \frac{1}{\sqrt{2\pi}} \int_{1/3}^{1} \frac{1}{\sigma(M)} \exp\left(-\frac{\delta^2}{2\sigma^2(M)}\right) d\delta \simeq \sigma(M) \exp\left(-\frac{1}{18\sigma^2(M)}\right), \tag{3.11}$$

where the approximation of the last relation uses the property of β being a rapidly decreasing function. This expression for the mass distribution of PBHs can be related to the comoving scales during inflation [45] therefore linking the distribution of PBH to the observational constraints.

Many scenarios for the cosmological density perturbations give a scale-invariant behaviour for $\sigma(M)$ in (3.11) corresponding to $n = 1$ in the power spectrum. The dependence of β on this function is however very sensitive and even a tiny deviation from the scale invariance can be important. If $\sigma(M)$ decreases with increasing M, then the spectrum falls off exponentially and the distribution of PBHs is mainly given by the smallest ones. On the other hand, if $\sigma(M)$ increases with increasing M, the spectrum rise exponentially and PBHs can form only on the largest scales. This second possibility seemed anyway to be rejected, because in this case the microwave anisotropies would be larger than observed.

Carr was the first in 1975 [33] to express the density parameter $\Omega_{\rm PBH}$ associated with PBHs formed at a redshift z or time t in relation to β,

$$\Omega_{\rm PBH} = \beta\Omega_{\rm R}(1+z) \simeq 10^6\beta\left(\frac{t}{1{\rm s}}\right)^{-1/2} \simeq 10^{18}\beta\left(\frac{M}{10^1{\rm 5g}}\right)^{-1/2}, \tag{3.12}$$

where $\Omega_{\rm R} \simeq 10^{-4}$ is the density parameter of the microwave background. The factor $(1+z)$ appears because the density of PBHs scales as a^3, while the density of the radiation scales as a^4. The constraints placed on $\Omega_{\rm PBH}$ translate to $\beta(M)$ and these are summarised in the first plot of figure 3.3, taken from Carr et al. [46]. The strongest constraints are coming from the γ-ray limit associated with PBHs evaporating at the present epoch [47, 48], while PBHs with masses larger than 10^{15} g are constrained only gravitationally, requiring that $\Omega_{\rm PBH} < 1$. Finally PBHs that have completely evaporated in the past have different constraints depending on their mass scales. In table 3.1 we have summarised the different aspects with respect the mass fraction of black holes at evaporation, $\alpha_{\rm evap}(M) = \rho_{\rm PBH}/\rho_{\rm rad}$. To interpret these one needs to relate the black hole masses to their lifetimes [49, 50], by

$$\alpha(M)_{\rm evap} = \frac{\beta_i}{1-\beta_i}\left(\frac{t_{\rm evap}}{t_{\rm form}}\right)^{1/2} \tag{3.13}$$

where $t_{\rm evap}$ and $t_{\rm form}$ are the evaporation and the formation time. These constraints on α are then translated to β, taking care of the model of the early universe, and then from β translated to $\sigma(M)$ using equation (3.11). These are summarised in the second plot of figure 3.3.

The calculation of the mass spectrum has not taken into account the relevance of critical collapse in PBH formation pointed out by Niemeyer & Jedamzik [38]. Green and Liddle [51] have recently analysed this under certain assumptions for the power spectrum, trying to see under which conditions the results of Niemeyer & Jedamzik seem cosmologically consistent. It is however a problem still to investigate, because Niemeyer & Jedamzik obtained a mass spectrum between $0.1 - 1$ times the horizon mass, not being able to see if smaller PBH are allowed to form.

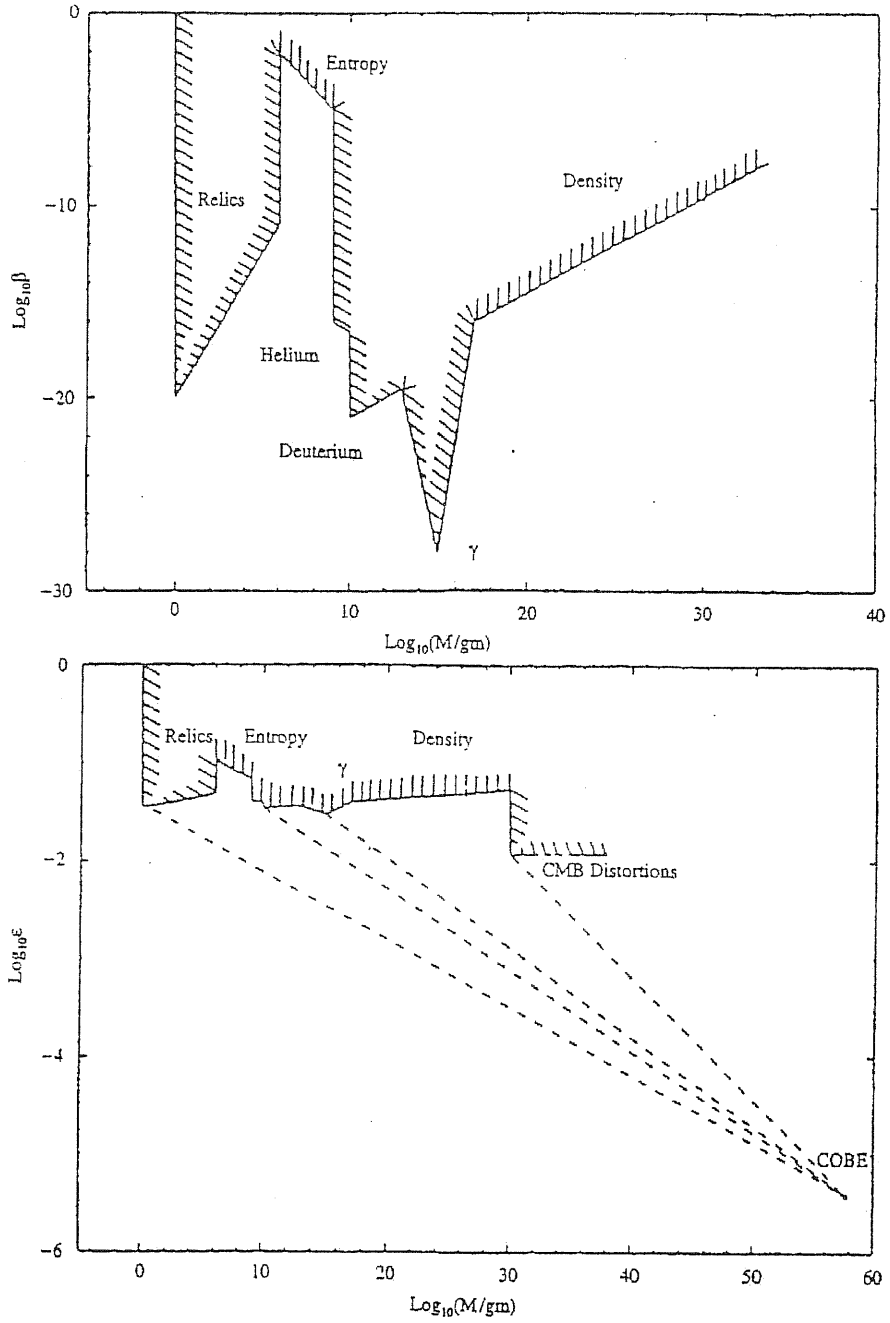

Figure 3.3: The first plot shows a summarise of the different constraints on $\beta(M)$, while the second plot shows the constraints on $\sigma(M)$. These plots have been taken by [46].

3.3.2 PBH and inflation

Connecting PBHs with inflation one gets two important consequences. The first is a minimum mass of the hole related to considering as the earliest time of formation the time of reheating. This is because PBHs formed earlier will be diluted to a negligible density by inflation. We

Constraints	Range	Reason
$\alpha_{\rm evap} < 0.04$	10^9 g $< M < 10^{13}$ g	Entropy per baryon at nucleosynthesis [52, 53]
$\alpha_{\rm evap} < 10^{-26}\left(\frac{M}{M_{\rm Pl}}\right)$	$M \simeq 5 \times 10^{14}$ g	γ-ray from current explosions[47, 48]
$\alpha_{\rm evap} < 6 \times 10^{-10}\left(\frac{M}{M_{\rm Pl}}\right)^{1/2}$	10^9 g $< M < 10^{11}$ g	$n\bar{n}$ production at nucleosynthesis [54]
$\alpha_{\rm evap} < 5 \times 10^{-29}\left(\frac{M}{M_{\rm Pl}}\right)^{3/2}$	10^{10} g $< M < 10^{11}$ g	Deuterium Destruction [55]
$\alpha_{\rm evap} < 1 \times 10^{-59}\left(\frac{M}{M_{\rm Pl}}\right)^{7/2}$	10^{11} g $< M < 10^{13}$ g	He-4 spallation[56]

Table 3.1: Limits on the mass fraction of PBH at evaporation.

have therefore

$$M > M_{\rm P}\left(\frac{T_{\rm rh}}{T_{\rm Pl}},\right)^{-2} \tag{3.14}$$

where $T_{\rm rh}$ is the reheating temperature which is different for the various models of inflation. Using the highest value of $T_{\rm rh} \sim 10^{16}$ Gev we have that the minimum mass related to the horizon scale is 1 g.

Another important limit coming from inflation is related to the slow roll approximation, $\epsilon, \eta \ll 1$ that plays a role in the exact determination of the spectral index n of power spectrum (2.38) written as [6]

$$n = 1 - 6\epsilon + 2\eta \simeq 1\,. \tag{3.15}$$

Because $\sigma(M) \propto M^{(1-n)/4}$ [45], this means that the fluctuations is slightly increasing with scale. To get PBH formation in agreement with the normalisation required for galaxy formation the perturbations should decrease with increasing mass (blue spectrum $n > 1$) and this is possible only with a sufficient acceleration of the scalar field.

These considerations were made for the first time by Carr [57, 58], from where figure 3.4 has been taken, and subsequently they have been refined by Green and Liddle [45]. Similar constraints have been obtained by several other people [59, 60], but an important aspect that

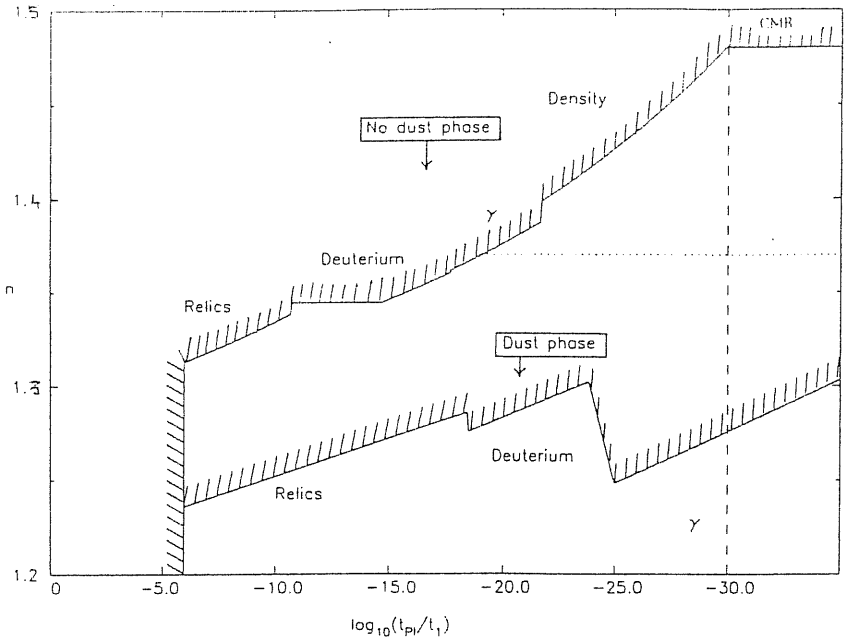

Figure 3.4: Constraints on the spectral index n in terms of reheat time t_1. This figure has been taken by [58].

should be stressed is that completely different conclusions can be obtained by a suitable choice of the field potential $V(\phi)$ [61, 62]. Another aspect investigated recently is the complication arising from a more complicated relation between the mass variance of the perturbations relevant for PBHs and the present day horizon-scale density fluctuations if one assumes a not scale free perturbation $n \neq 1$ [63, 64]. Many different models of inflation have been constrained in relation to possible PBH formation ([17] and references therein).

3.3.3 PBH and dark matter

We know from observations that roughly 30% of the total density of the universe is in the form of cold dark matter. PBHs, if they exists, are a natural candidate for this component of the universe and some interests has been dedicated to holes larger than 10^{15} g, that would not yet have evaporated. For example they can play a role in the formation of large scale structure in particular in the (sublunar) mass range of $10^{20} - 10^{26}$ g ([17] and references therein).

One interesting possibility is that PBHs may have formed during the quark hadron phase transition, profiting from the temporary softening of the equation of state at around 10^{-5} s [65]. The order of mass associated to these PBHs is about $1\,M_{\odot}$ and therefore they were been suggested as candidates to explain the MACHO micro lensing results [66]. Niemeyer & Jedamzik have performed numerical simulations of PBH formation during the QCD phase transition assuming it to be first order [65]. They obtained a significant reduction in the threshold value of δ_c with respect the value that they found just for the radiation case [39] This implies that PBH formation would be strongly enhanced during this epoch with a mass

distribution concentrated around 1 $M_{\odot}$. Their calculation is anyway just preliminar because they have assumed a very simplified model to describe the phase transition and so it is possible that one would obtain different results with a more sophisticated treatment. An implication for PBHs formed in this way is the existence in the galactic halo of a population of binary PBHs which at the present epoch would emit gravitational waves as they inspiral and coalesce (see [17] and reference therein).

As we have just mentioned in the previous section, another possibility is that the evaporation of PBHs stops near the Planck scale leaving stable remnants as a possible cold dark matter candidate. PBH production is also possible during inflation and this imposes limits on $\beta(M)$ included in figure 3.4, requiring that their density is less then the critical value. To produce a relevant density of relics needs a fine tuning of $n \simeq 1.3$ [33] which is on the limit of compatibility with the WMAP results. Chen has also argued that hybrid inflation could produce relics from $\sim 10^5$ g PBHs formed at $\sim 10^{32}$ s (see [17] and references therein).

3.3.4 PBH and high energy physics

If one considers with more attention the emission of particles during black hole evaporation it should be taken into account that the process is strongly dependent on the model of elementary particles used. One reasonable assumption made is that the effect of possible charge and angular momentum associated with the hole would be lost through quantum emission on a shorter time scale than the mass evaporation rate, so that the hole can be considered as non rotating and uncharged during the most important stages of evaporation [67]. Taking this into account, expression (3.4) and (3.5) can be rewritten as

$$\frac{dM}{dt} = -5 \cdot 10^{25} \left(\frac{M}{1g}\right)^{-2} f(M) \text{g s}^{-1}, \tag{3.16}$$

$$t_{\text{evap}} M = 6 \cdot 10^{-27} \frac{1}{f(M)} \left(\frac{M}{1g}\right)^{3} \text{s}, \tag{3.17}$$

where the function $f(M)$ depends on the number of particles specie which are light enough to be emitted by a hole of mass M. In the range of black holes larger than 10^{17} g only massless particles like photons, neutrinos and gravitinos can be emitted. In the range of 10^{15} g $< M <$ 10^{17} g it is also possible to emit electrons, and for 10^{14} g $< M < 10^{15}$ g particles such as muons are emitted, which subsequently will decay into electrons and neutrinos. When the mass falls below 10^{14} g, the process enters the scale of energy needed to emit hadrons and therefore QCD should be taken into account [68]. Many simplifications can be applied to describe this process and the result obtained is that black holes would emit quark and gluon jets that will subsequently decay into hadrons over a distance where the gravitational attraction of the hole is negligible. Other decays can then transform the hadrons into stable particles through weak and electromagnetic interactions. In studying all of these processes one should take into account that smaller holes will evaporate at an earlier cosmological epoch and therefore the energy of the particles emitted will have been redshifted by the present epoch.

If the emission of particles is homogeneously distributed throughout the universe, it is possible to calculate with good precision the background spectra [69]. If this is not the case as

for the evaporation of PBHs in the galactic halo at the present epoch, the description of the process is different [70].

Gamma ray bursts and cosmic rays emission might also be connected with Hawking evaporation and different constraints have been worked out in relation of the observations of these phenomena [71].

3.4 Open questions

As one can see from this synthetic overview, there are still many aspects that are not clear and need further investigation. In our perspective there are three key problems that we think have priority. First there is the question about the value of δ_c that a perturbation must exceed in order to give rise to PBH formation. The reason for the discrepancy between the value of $\delta_c \simeq 0.7$ obtained by Niemeyer & Jedamzik [39] and the interval of $0.3 \lesssim \delta_c \lesssim 0.5$ found by Green et al. [43] needed to be understood. Knowledge of a precise value of δ_c is very important for calculating the mass fraction of the universe that could be in the form of PBHs. Second, there is the issue of knowing the extent to which the possibility of forming PBHs is dependent on the particular choice of initial conditions and which kind of profiles best describe actual cosmological perturbations. It would be very useful to go beyond the Press-Schecter-like approach and connect the initial conditions directly with the statistics of vacuum fluctuations coming from inflation. Third it is also important to clarify the question of the real impact of critical collapse in the scenario of PBH formation, to know if PBH masses are all on roughly the horizon scale at the time of formation or if the scaling law is preserved all the way down to very small masses. These problems represent the challenge for the original contributions of this work that we are going to present in the following three chapters.

Chapter 4

Computations of primordial black hole formation

With this chapter we start to describe the original contributions that we have made to studies of PBHs with our work. As we have said at the end of the previous chapter, we think that there is not a good link between a realistic cosmological scenario of cosmological perturbations coming from inflation with a Gaussian spectrum and the initial conditions used in the numerical simulations recently performed [3]. As pointed out by Shibata & Sasaki [44], the initial conditions should describe a pure growing mode solution. Lack of consistency with this may have been the reason for the discrepancy observed between the results obtained by Niemeyer & Jedamzik and those obtained by Shibata & Sasaki, as pointed out by Green et al. [43]. The work of Shibata & Sasaki used a very complicated formulation of the equations, because they were written generically to study also non-spherical collapse. When we started to be interested in this subject we were able to profit from having available a pre-existing code developed by John Miller to study isolated collapse in vacuum, with a similar formulation of the equations to that used by Niemeyer & Jedamzik . This formulation is simpler to handle than that used by Shibata & Sasaki, because the set of equation is specifically written in spherical symmetry. For these reasons we have started by using this code, making necessary modifications to move from an isolated collapse in vacuum to collapse of a cosmological perturbation within the FRW background.

In the first section of this chapter we introduce the set of equations used to write the code, describing the strategy of the simulations, and pointing out the modifications that we have introduced to use the code in a cosmological context.

In the second section we describe in some detail in the numerical method used to run the calculations, explaining how the equations are numerically integrated and how we have chosen the initial conditions. We show also the agreement between the analytical and numerical solution representing the background as a proof of the correct behaviour of the numerical code in that case.

In the third section we give a description of the results, where the initial conditions used are very similar to those considered by Niemeyer & Jedamzik , but we introduce a fundamental

improvement that allows us to explain the discrepancy observed by Green et al.[43], decreasing the effective value of δ_c below that seen by Niemeyer & Jedamzik . Attention is dedicated to the hydrodynamical features of the collapse, and to the scaling law relation, analysing also the changes that occur when a cosmological constant component is included in the equations. Finally we describe in detail the hydrodynamical processes that we observe in a subcritical collapse, when the value of δ is slightly less that than threshold δ_c.

The order of the presentation in this part of the thesis follows the order in which the work was done. In this chapter we present calculations made with a simple method for imposing approximate growing-mode initial conditions in terms of δ and δU which represents a step forward with respect to previous work, and allows several issues to be clarified. However this treatment of initial conditions is still not optimal and in Chapter 5 we introduce a new and more precise way for doing this in terms of curvature perturbations which enables a better link to be made with a perturbation spectrum coming from inflation.

4.1 Mathematical formulation of the problem

As with most of the other literature on this subject, we are restricting attention here to spherical symmetry, which very greatly simplifies the calculations, and we have used the formulations of the relativistic hydrodynamical equations given by Misner & Sharp (1964) [72] and Hernandez & Misner (1966) [73]. Both of these are Lagrangian formulations, the first using a diagonal metric (with the time referred to as "cosmic time" which reduces to the familiar FRW time coordinate in the absence of perturbations), and the second using an outward null slicing where the time coordinate is an "observer time" (the clock time as measured by a distant fundamental observer). The cosmic-time formulation is particularly simple and has the advantage of using a slicing which many people find intuitive; this was the approach used by May & White (1966) [35] in their classic paper studying spherically-symmetric gravitational collapse. However this approach has a well-known drawback for studying black hole formation in that singularities that are typically formed rather early in calculations of continuing collapse and it is not then possible to follow the subsequent evolution. We will look at this in more detail in Section 4.1.2.

The outward null slicing approach is particularly convenient for calculations involving black hole formation in spherical symmetry: anything which could not be seen by a distant observer (e.g. singularity formation) does not occur within the coordinate timespan, while all observable behaviour can be calculated. This is, in some sense, the optimal approach for studying black hole formation in spherical symmetry as seen by an outside observer (being linked directly to potential observations) although more sophisticated slicing conditions have advantages for calculations away from spherical symmetry.

Following the introduction of the observer-time approach by Hernandez & Misner in 1966 [73], it was implemented soon afterwards in unpublished calculations. A brief presentation of some results was given by Miller & Sciama (1980) [74] and a full discussion of the technique used and of results obtained was given subsequently by Miller & Motta (1989) [75]. A problem with the use of this method concerns the satisfactory specification of initial conditions which is not natural to do on a null slice. Because of this, Miller & Motta [75] made a preliminary

calculation using the Misner & Sharp [72] formulation in order to construct data on an outgoing null slice from initial conditions specified on a space-like slice; the observer-time calculation then proceeded from the null-slice data constructed in this way. Subsequently, Baumgarte, Shapiro & Teukolsky (1995) [76] made calculations using a similar technique and it was these which were used as a reference point by Niemeyer & Jedamzik [39].

4.1.1 The Misner-Sharp equations

For calculations in spherical symmetry, it is convenient to divide the collapsing matter into a system of concentric spherical shells and to label each shell with a Lagrangian co-moving radial coordinate which we will denote with r. The metric can then be written in the form

$$ds^2 = -a^2\,dt^2 + b^2\,dr^2 + R^2\left(d\theta^2 + \sin^2\theta d\varphi^2\right), \tag{4.1}$$

where R (the Schwarzschild circumference coordinate), a and b are functions of r and the time coordinate t. This was the form used Misner & Sharp (1966) [72].

For a classical fluid, composed of particles with nonzero rest-mass, it is convenient to use the rest-mass μ contained interior to the surface of a shell (or, equivalently, the baryon number) as its co-moving coordinate r. For the case of a radiation fluid (as studied here), rest-mass and baryon number are not available as conserved quantities to be used in this way but a similar procedure can still be followed by introducing the concept of a conserved number of unit co-moving fluid elements (Miller & Pantano 1990) [77]. Denoting a "relative compression factor" for these fluid elements by ρ (equivalent to the rest-mass density in the standard treatment), one then has

$$d\mu = 4\pi\rho R^2 b\,dr, \tag{4.2}$$

and identifying μ and r then gives

$$b = \frac{1}{4\pi R^2\rho}. \tag{4.3}$$

Following the notation of [72], we write the equations in terms of the operators

$$D_t \equiv \frac{1}{a}\left(\frac{\partial}{\partial t}\right), \tag{4.4}$$

$$D_r \equiv \frac{1}{b}\left(\frac{\partial}{\partial \mu}\right), \tag{4.5}$$

and applying these to R gives

$$D_t R \equiv U, \tag{4.6}$$

$$D_r R \equiv \Gamma, \tag{4.7}$$

where U is the radial component of the four-velocity in the associated Eulerian frame, using R as the radial coordinate, and Γ is a generalization of the Lorentz factor.

In this thesis we are dealing with processes involving a perfect fluid described by (1.20), where in general the parameter γ can be time dependent. In this chapter we focus on the radiation dominated era of the Universe for which $\gamma = 1/3$. For one-parameter equations of

state of the form $p = p(e)$, the system of Einstein and hydrodynamic equations can then be written as:

$$D_t U = -\left[\frac{\Gamma}{(e+p)} D_r p + \frac{M}{R^2} + 4\pi R p\right], \tag{4.8}$$

$$D_t \rho = -\frac{\rho}{\Gamma R^2} D_r (R^2 U), \tag{4.9}$$

$$D_t e = \frac{e+p}{\rho} D_t \rho, \tag{4.10}$$

$$D_r a = -\frac{a}{e+p} D_r p, \tag{4.11}$$

$$D_r M = 4\pi \Gamma e R^2, \tag{4.12}$$

where M is a measure of the mass-energy contained inside radius μ and Γ can be calculated either from (4.12) or from the constraint equation

$$\Gamma^2 = 1 + U^2 - \frac{2M}{R}. \tag{4.13}$$

4.1.2 Using Misner-Sharp approach for studying black hole formation

As mentioned above, using the cosmic time approach throughout for making calculations of gravitational collapse leading to black hole formation has the well-known drawback that singularities appear after a finite time in the calculation, before an event horizon has formed as far as this time-slicing is concerned. Once a singularity has formed, the calculation cannot be continued further and so parts of the evolution which could potentially be seen by an outside observer cannot be followed in this way. In particular, it is not possible to follow all of the process of the formation of the event horizon. This drawback is the reason for the observer-time formulation being used in the present work for cases where a black hole is formed rather than continuing to use the cosmic time formulation throughout.

The present work is concerned with black hole formation in a radiation fluid, for which the behaviour is rather different from that in a more standard fluid and it is useful to see this first in the more familiar context of collapse of a destabilised isolated matter distribution rather than of an over-density within an expanding background. In Figure 4.1 below, we show results from a calculation of collapse leading to black-hole formation using the cosmic time formulation throughout in the case of a fluid with a polytropic equation of state given by $p = k\rho^{5/3}$, following the paper by Miller & Motta (1989) [75]. The initial model is an isolated equilibrium configuration which has been destabilised by reducing the internal energy, using the same value of k as that used by May & White (1966) in their classic paper on this subject. The behaviour during the collapse of the radius R, energy density e and the generalised Lorentz factor Γ are shown as functions of the co-moving coordinate μ at a succession of times during the calculation. The time ordering of the curves goes from top to bottom in the figures for R and Γ and from bottom to top in the figure for e; μ is normalised so as to be equal to unity at the surface of the configuration. The well-known formation of an off-centre singularity can be seen occurring after a finite time, with $R \to 0$ and $e \to \infty$ at $\mu \simeq 0.115$, the region where R decreases with increasing μ corresponding to negative values of Γ. The behaviour

represents the progressively increasing distortion of the space-like hypersurfaces of constant t as the collapse proceeds and their eventual pinching off at finite μ. Figures 4.2 show the same quantities in an equivalent calculation for the radiation equation of state $p = e/3$, with the initial model here having the same profile of pressure as a function of μ as in the polytropic case (calculations for the same profile of e as in the polytropic case do not lead to collapse of the entire configuration). It can be seen that the singularity now forms much closer to the centre in terms of μ, appearing to be completely central here in the case of e. However, it seems that the fundamental off-centre location of the singularity always continues to be seen whenever the grid resolution in the central zones is made fine enough.

Our calculations for black-hole formation from over-densities within an expanding universe are using a similar radiation equation of state and a similar phenomenology is seen as for the

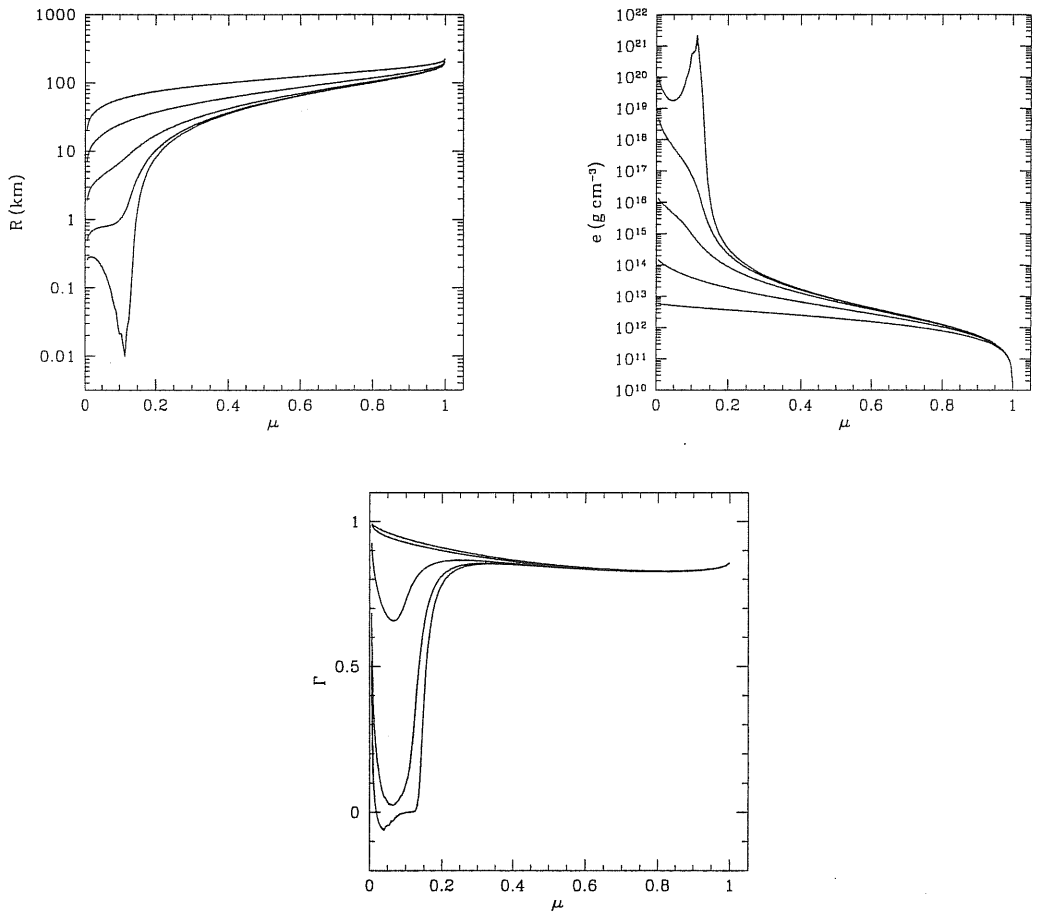

Figure 4.1: These plots show the evolution in cosmic time of R, e and Γ for an isolated collapse leading to black hole formation, using the polytropic equation of state $p = k\rho^{5/3}$. Note the formation of an off-centered singularity, where R is going to 0 and e tends toward infinity.

isolated collapse with the radiation fluid if the cosmic-time approach is used for all of the calculation, except that the singularity now appears to form completely centrally with our grid spacing. However, the fundamentally off-centred singularity formation probably always occurs in fact, as discussed above. These considerations are interesting for having a more complete picture of what is going on but since we are concentrating on using the observer-time slicing in our present calculations for collapses leading to black hole formation, they are a side issue here.

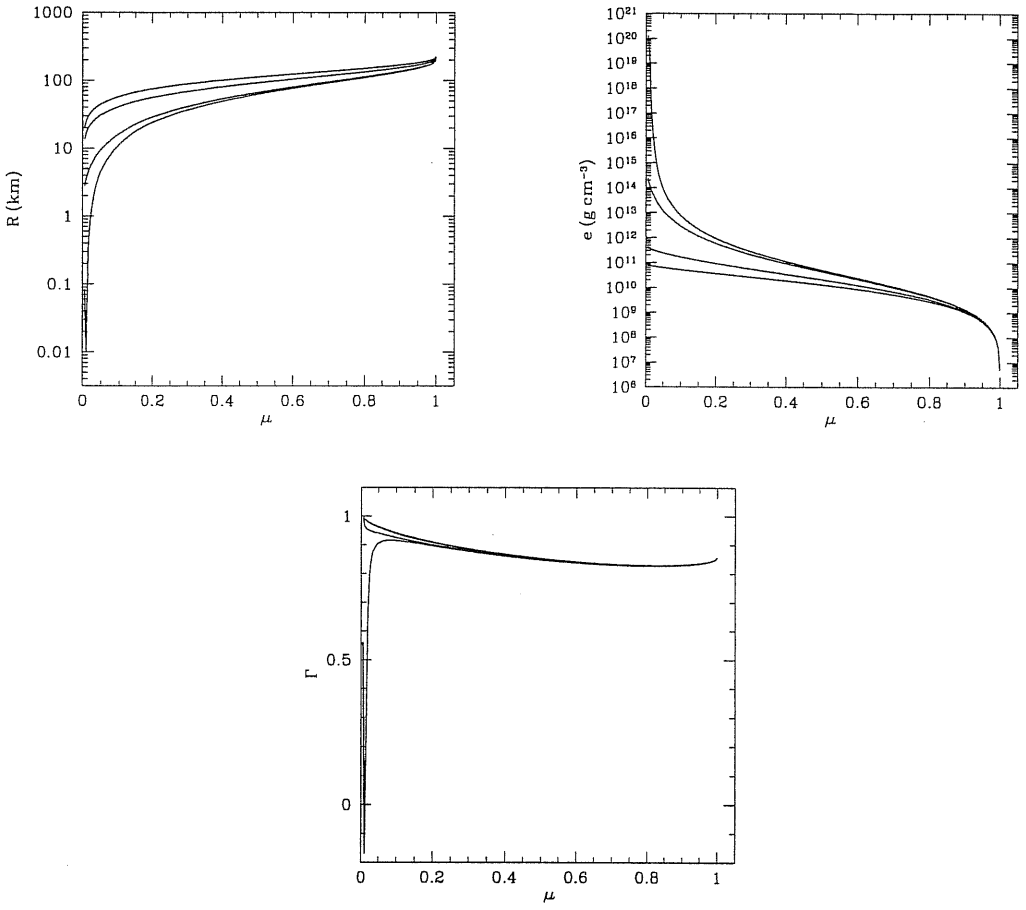

Figure 4.2: These plots show the evolution in cosmic time of R, e and Γ for an isolated collapse leading to black hole, using the radiation equation of state $p = e/3$. The initial model here has the same profile of pressure as a function of μ as in the polytropic case. Note the formation of a singularity located almost at the centre with a similar behaviour to that in the previous case.

4.1.3 The Hernandez-Misner Equations

Because of the problems mentioned above, Hernandez & Misner [73] introduced the concept of "observer time", using as the time coordinate the time at which an outgoing radial light ray emanating from an event reaches a distant observer[1]. In the original formulation, this observer was placed at future null infinity but for calculations in an expanding cosmological background we use an FRW fundamental observer sufficiently far from the perturbed region to be unaffected by the perturbation. Along an outgoing radial null ray we have

$$a\,dt = b\,dr, \tag{4.14}$$

and we define the observer time u by

$$f\,du = a\,dt - b\,dr, \tag{4.15}$$

with f being an integrating factor which needs to be determined. In terms of this, the metric becomes

$$ds^2 = -f^2\,du^2 - 2fb\,dr\,du + R^2\left(d\theta^2 + \sin^2\theta d\varphi^2\right), \tag{4.16}$$

which is no longer diagonal. The operators equivalent to (4.4) and (4.5) are now

$$D_t \equiv \frac{1}{f}\left(\frac{\partial}{\partial u}\right), \tag{4.17}$$

$$D_k \equiv \frac{1}{b}\left(\frac{\partial}{\partial r}\right) = 4\pi\rho R^2\left(\frac{\partial}{\partial \mu}\right), \tag{4.18}$$

where D_k is the radial derivative in the null slice and the corresponding derivative in the Misner-Sharp space-like slice is given by

$$D_r = D_k - D_t. \tag{4.19}$$

The observer-time equations replacing the cosmic-time ones (4.8) - (4.12) are then:

$$D_tU = -\frac{1}{1-c_s^2}\left[\frac{\Gamma}{(e+p)}D_kp + \frac{M}{R^2} + 4\pi Rp + c_s^2\left(D_kU + \frac{2U\Gamma}{R}\right)\right], \tag{4.20}$$

$$D_t\rho = \frac{\rho}{\Gamma}\left[D_tU - D_kU - \frac{2U\Gamma}{R}\right], \tag{4.21}$$

$$D_te = \left(\frac{e+p}{\rho}\right)D_t\rho, \tag{4.22}$$

$$D_kf = \frac{f}{\Gamma}\left(D_kU + \frac{M}{R^2} + 4\pi Rp\right), \tag{4.23}$$

$$D_kM = 4\pi R^2[e\Gamma - pU], \tag{4.24}$$

[1]We note that a somewhat similar approach, but based on a double null foliation, has recently been used by Harada et al. [78, 79, 80] for studying some different aspects of PBH formation.

where $c_s = \sqrt{(\partial p/\partial e)}$ is the sound speed, which is equal to $1/\sqrt{3}$ in the radiative era. The quantity Γ is given by equation (4.13), as before, and also by

$$\Gamma = D_k R - U \,. \tag{4.25}$$

Using equations (4.23), (4.24) and (4.13), it is possible to derive the following alternative equation for f:

$$D_k \left[\frac{(\Gamma + U)}{f} \right] = -4\pi R(e+p)f \,. \tag{4.26}$$

In calculations concerning collapse of an isolated object surrounded by vacuum in an asymptotically flat space time, the observer time is taken to be the clock time of a static observer at future null infinity and so $(\Gamma + U)/f = 1$ at the location of that observer (since $\Gamma = 1$, $U = 0$ and $f = 1$ there). It then follows from equation (4.26) that $(\Gamma + U)/f = 1$ also at the surface of the collapsing object, since the right hand side of (4.26) is zero in vacuum. The condition

$$f = \Gamma + U, \tag{4.27}$$

at the surface is used as a boundary condition for f and the values of f internal to that are then calculated from equation (4.23).

The general condition for a trapped surface is $D_k R \leq 0$. With outgoing null slicing, $D_k R = 0$ should be reached only asymptotically in the future, accompanied by the lapse f going to zero, and $D_k R$ should never become negative. In practice, care is required in order to achieve the exact synchronization of $D_k R \to 0$ and $f \to 0$ in a numerical solution where the equations are discretized; if the synchronization is not achieved, negative values of $D_k R$ do appear and the evolution becomes unphysical.

In the case of an isolated collapsing object surrounded by vacuum, using boundary condition (4.27) together with equation (4.23) ensures the correct behaviour. However, for the present situation, where the surroundings are not vacuum and the space time is not asymptotically flat, it is necessary to proceed in a different way. We are wanting to synchronize the "observer time" with the clock time of a co-moving FRW fundamental observer at the outer edge of the grid (setting $f = 1$ there) and then to calculate f elsewhere using this as a boundary condition. For doing this, we found it essential to use equation (4.26), which guarantees synchronization of $D_k R \to 0$ and $f \to 0$, rather than equation (4.23), which always eventually gave rise to unphysical behaviour with $D_k R < 0$. We think that this is a crucial point in using an outward null slicing technique for any situation regarding black hole formation within non-vacuum surroundings. It will apply equally to calculations of black hole formation from core-collapse of high-mass stars.

4.2 The calculation method

As mentioned above, our calculations of PBH formation have been made using an explicit Lagrangian hydrodynamics code based on that of Miller & Motta (1989) [75] but with the grid organised in a way similar to that in the code of Miller & Rezzolla (1995) [74], which was

designed for calculations in an expanding cosmological background. The method described by Niemeyer & Jedamzik [39], following from the Baumgarte et al. code [76], is similar in most respects.

4.2.1 Calculation scheme

For collapses leading to black hole formation, our calculations proceed in two stages: first, initial data is specified on a space-like slice at constant cosmic time, specifying the energy density e and the four-velocity component U as functions of R at an initial time t_i. This data is then evolved using the Misner-Sharp equations of Section 4.1.1 so as to generate a second set of initial data on a null slice (at constant observer time). To do this, an outgoing radial light ray is traced out from the centre and parameter values are noted as it passes the boundary of each grid zone. The second set of initial data, constructed in this way, is then evolved using the Hernandez-Misner equations of Section 4.1.3. For sub-critical cases, which end eventually with dispersal of the perturbation into the surrounding uniform medium, we have continued with the Misner-Sharp cosmic-time approach throughout. Figure 4.3 shows schematically the two different foliations with cosmic time t and observer time u.

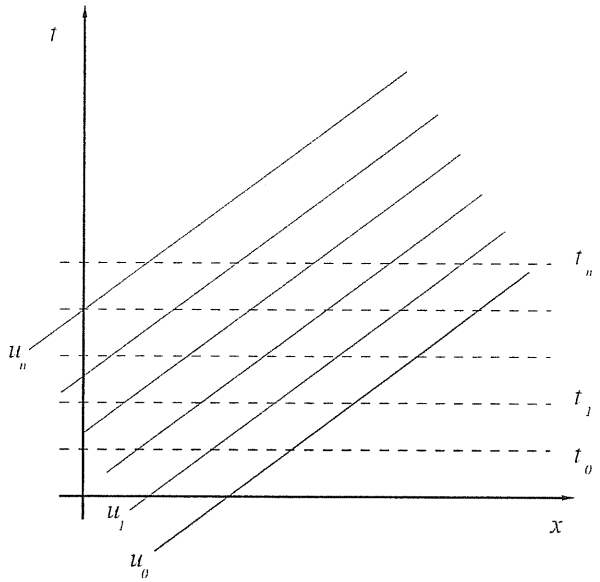

Figure 4.3: This diagram shows the space time foliation for the two different prescriptions used in the numerical simulations: t_i represents the cosmic time levels, while u_i represents the observer time ones.

The unperturbed background model is taken as a spatially-flat FRW model, for which $\Gamma = 1$ (giving $U = \sqrt{2M/R}$) with $e(r) =$ constant at any particular cosmic time t. The perturbations of e and U are then superimposed on this background in the way described in the next section. During the following evolutions, the metric functions a (for cosmic time) and f (for observer time) are set equal to unity at the outer boundary of the grid, thus synchronising the cosmic and observer times with local clock time there as measured by the local co-moving FRW fundamental observer.

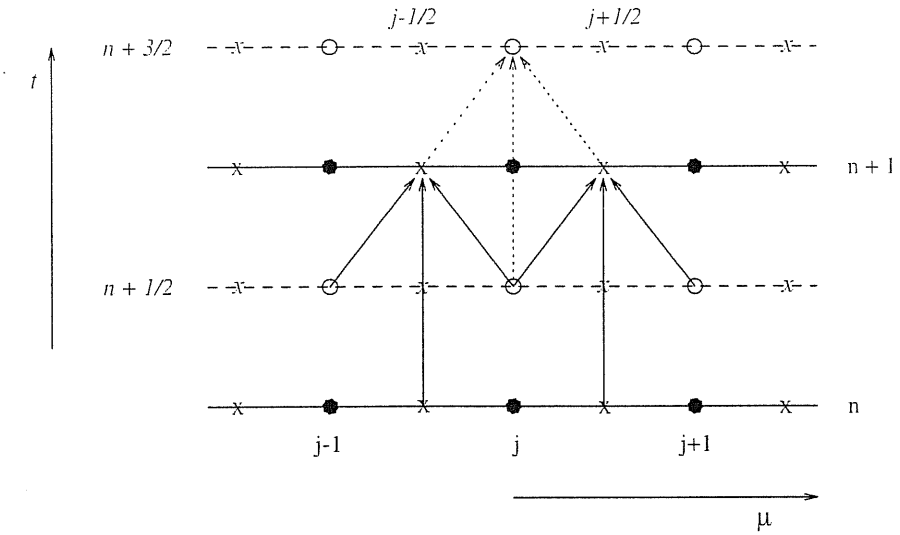

Figure 4.4: Schematic representation of the numerical evolution as represented in the gridding scheme with two offset interlocking grids. Spatial gridpoints are numbered outward from the centre.

The numerical integration of both Misner-Sharp and Hernandez-Misner equations is done using an explicit finite difference scheme using intermediate time levels, giving approximately second order accuracy in space and time. Using two different overlapping grid-schemes we can calculate the spatial and time derivatives correctly centered at each time-level. Figure 4.4 shows a schematic representation of the structure of the calculation on the grid. In the standard methodology for Lagrangian hydrodynamics, intensive quantities are calculated at zone centres and extensive quantities are calculated at zone boundaries. Figure 4.4 shows the basic scheme used to obtain the centering of the time derivatives. A mid-zone quantity calculated at the time-level n is evolved to level $n+1$ using the space derivative calculated at level $n+1/2$ (solid lines). In the same way a zone-boundary quantity calculated at the level $n+1/2$ is evolved to $n+3/2$ using the spatial derivative at level $n+1$ (dashed lines). As an example of this we write the explicit expression used in the code to evolve the radial velocity U from level $n-1/2$ to $n+1/2$ in the Misner-Sharp scheme

$$U_j^{n+1/2} = U_j^{n-1/2} - \Delta t^n a_j^n \cdot \left(4\pi \left(R_j^n\right)^2 \frac{\Gamma_j^n}{w_j^n} \frac{p_{j+1/2}^n - p_{j-1/2}^n}{\Delta\mu_j} + \frac{M_j^n}{\left(R_j^n\right)^2} + 4\pi p_j^n R_j^n \right) \tag{4.28}$$

where

$$w = (e+p)/\rho \tag{4.29}$$

is the specific enthalpy,

$$w_j^n = \frac{w_{j-1/2}^n \Delta\mu_{j-1/2} + w_{j+1/2}^n \Delta\mu_{j+1/2}}{2\Delta\mu_j} \tag{4.30}$$

and

$$p_j^n = \frac{p_{j-1/2}^n \Delta\mu_{j-1/2} + p_{j+1/2}^n \Delta\mu_{j+1/2}}{2\Delta\mu_j}. \tag{4.31}$$

For maintaining numerical stability, the time-step needs to satisfy the Courant Condition. In the cosmic time scheme this is given by

$$\Delta t < \frac{b}{a}\left(\frac{\Delta\mu}{c_s}\right) = \frac{1}{4\pi R^2 \rho a}\left(\frac{\Delta\mu}{c_s}\right), \tag{4.32}$$

where the second equality is obtained using (4.3). We set the timestep equal to the minimum value of

$$\Delta t = \frac{k}{4\pi R^2 \rho a}\left(\frac{\Delta\mu}{c_s}\right) \tag{4.33}$$

across the grid and have found that $k = 0.2$ is satisfactory for giving numerical stability in our case. To maintain accuracy, the time-step is also controlled so as to limit changes, in ρ and e, to at most 2% per time-step at any comoving location.

In the observer time scheme the equivalent of (4.33) is

$$\Delta t = k\frac{1}{4\pi R^2 \rho f}\left(\frac{\Delta\mu}{c_s}\right), \tag{4.34}$$

and experiments have shown that a value of $k = 0.1$ is satisfactory to achieve stability. We have also added a timestep constraint for changes in the lapse f so that it will not change by more than $2 \times 10^{-3}\%$ per timestep at any comoving location. This low value is needed in order to follow the asymptotic approach to $D_k R = 0$ with care.

In order to achieve good grid coverage, we have used a composite prescription for the grid spacing, with $\Delta\mu$ increasing exponentially going outward through the inner and outer parts of the grid but remaining constant in an intermediate region. For the exponential part of the grid we have used an increment $\Delta\mu_i = 1.024 \times \Delta\mu_{i-1}$. We need to have a grid extending sufficiently far out to describe perturbations also outside the overdensity region. We started our perturbations in the linear regime with length-scales R_0 larger than the cosmological horizon radius R_H, and had the grid reaching out to $10\,R_0$ with around 2000 grid points.

4.2.2 Evolving the background solution

The pre-existing code that we have used as a basis for developing the present one has been widely tested and we will not go into details of this here. It was important to make an additional test, however, to ensure that the new code could satisfactorily evolve the unperturbed background FRW solution.

Figure 4.5 shows results from a calculation using the cosmic time formulation. In the top frames we see the very good agreement obtained between the analytical and numerical solutions for the energy density e and the Hubble parameter H, given analytically by

$$e(t) = e(t_i)\left(\frac{t}{t_i}\right)^{-2} \tag{4.35}$$

$$H = \frac{1}{2t}. \tag{4.36}$$

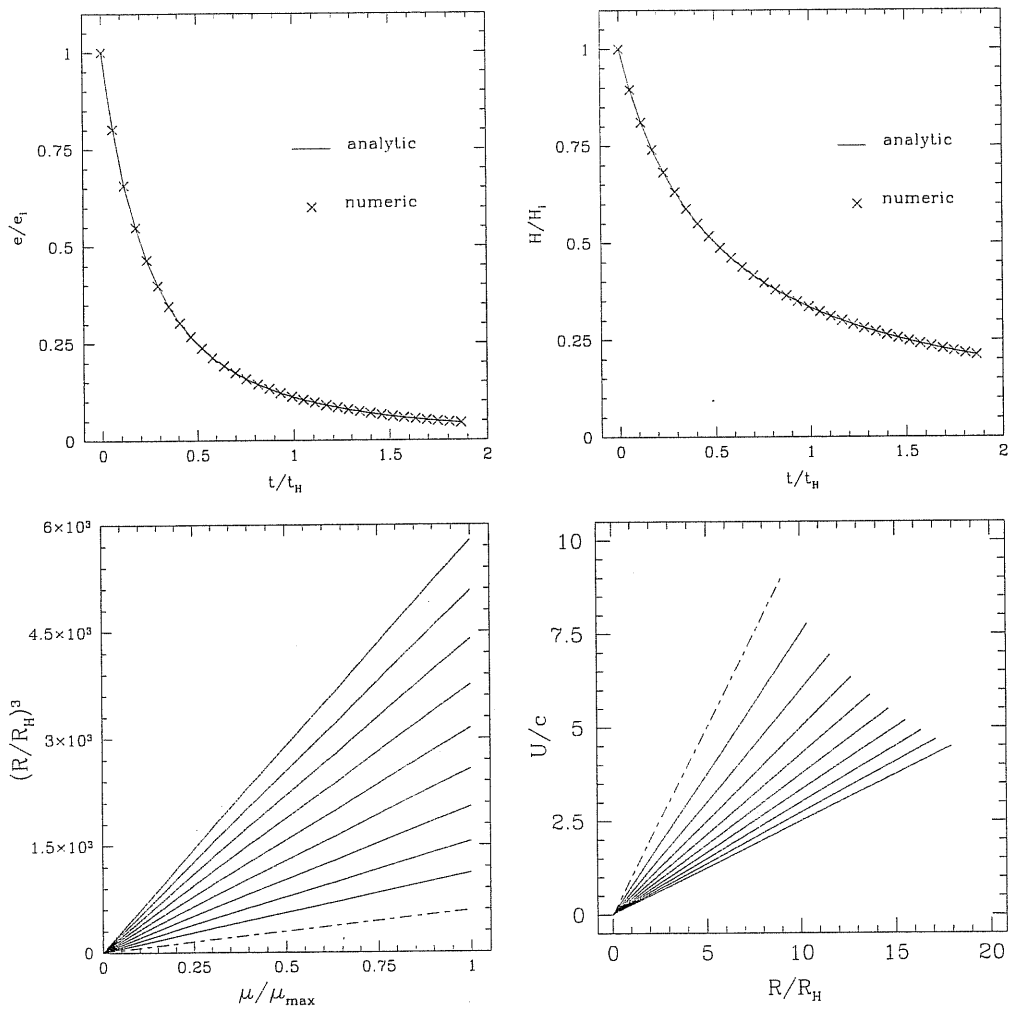

Figure 4.5: These plots show the agreement between the analytical and numerical solutions for the background quantities. In the top plots the evolution off the energy density e_b calculated at a particular location, is plotted in the left panel, while the Hubble parameter H_b is plotted in the right panel. In the bottom plots the behaviour of the cube of the circumferential coordinate R_b^3 is plotted in the left panel against the Lagrangian coordinate μ at successive times, while the radial velocity U is plotted against R_b/R_H in the right panel. The dashed lines represent the initial profile in the bottom panels.

The energy density remains uniform across the grid, to within deviations less than 10^{-6}. The analytical solution for R as a function of μ is given by integrating equation (4.2) that when $\rho(R)$ is constant, gives

$$R_\mathrm{b} = \left(\frac{\mu}{4\pi\rho}\right)^{1/3} \tag{4.37}$$

This means that R^3 plotted as function of μ should give a series of straight lines with the gradients increasing with time. The numerically-calculated behaviour is shown in the left bottom panel of figure 4.5 where the correct behaviour is reproduced to very high accuracy. A

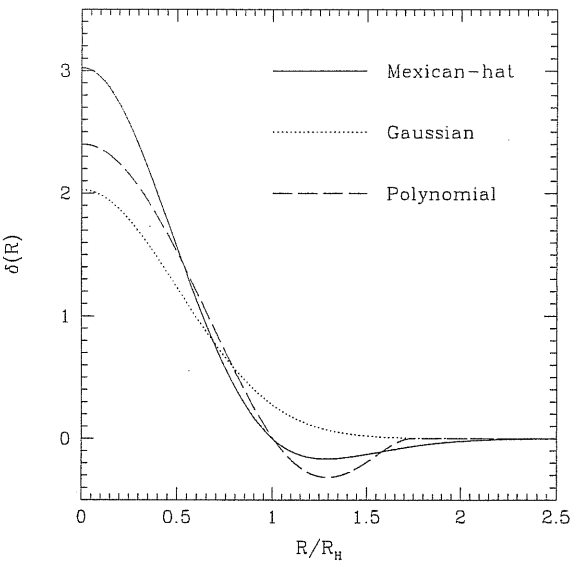

Figure 4.6: Profiles of the perturbations. The amplitudes plotted corresponds to the threshold values measured at horizon crossing time, as given by Niemeyer & Jedamzik [39].

similar test consists of verifying preservation of the Hubble law $U = HR$. The right bottom panel of Figure 4.5 shows the behaviour of the radial velocity U plotted against R and we can observe a series of straight lines with decreasing gradient, consistently with expression (4.36).

In the observer-time slicing, we have no simple analytic solution for the background against which to check the numerical code. However the quantity Γ is gauge invariant and $\Gamma = 1$ to within one part in 10^6 for unperturbed-spatially flat solutions, for both of the schemes used here.

4.2.3 Initial conditions

To specify the initial conditions we have decided to use the same prescription as [39], where the perturbations were specified in terms of the dimensionless quantity

$$\delta_e(R) \equiv \frac{e - e_b}{e_b} = \frac{\delta e}{e_b} \tag{4.38}$$

where e_b is the uniform background density given, for $\gamma = 1/3$, by $e_b = 3/32\pi t$ at any particular time t. In [39] three different types of expression for δ_e have been used, and these are shown in Figure 4.6, measured at horizon crossing time (when they were imposing their initial conditions), for the threshold amplitude. The mathematical expression for these expression different types of perturbations are:

Gaussian:

$$\delta_e(R) = A \exp\left(-\frac{2R^2}{(LR_H)^2}\right), \tag{4.39}$$

Mexican hat:

$$\delta_e(R) = A\left(1 - \frac{R^2}{L^2 R_H^2}\right)\exp\left(-\frac{3R^2}{2L^2R_H^2}\right), \tag{4.40}$$

Polynomial:

$$\delta_e(R) = \begin{cases} \dfrac{A}{9}\left(1 - \dfrac{R^2}{L^2R_H^2}\right)\left(3 - \dfrac{R^2}{L^2R_H^2}\right) & \text{if } R < \sqrt{3}\,(LR_H) \\ 0 & \text{if } R \geq \sqrt{3}\,(LR_H) \end{cases} \tag{4.41}$$

where the parameters A and L set the amplitude and length-scale of the perturbation. For the Mexican-hat and polynomial perturbations, the excess energy in the overdense region is exactly balanced by the deficit in the outer underdense region (i.e. $\int_0^\infty 4\pi\delta_e R^2 dR = 0$), whereas the Gaussian ones have only an excess, decreasing asymptotically to the background value. The latter is not very satisfactory for cosmological perturbations because it violates the energy conservation with respect the unperturbed solution, and so we concentrate here on the first two types.

We follow the previous literature in also using an "integrated" perturbation δ which represents the mass-energy excess in the overdense region with respect to that in a corresponding uniform solution:

$$\delta \equiv \frac{\displaystyle\int_0^{R_0} 4\pi\,\delta_e\,R^2 dR}{\dfrac{4}{3}\pi R_0^3}, \tag{4.42}$$

where R_0 is the radius of the overdensity. (In the case of the Gaussian, R_0 is defined as the radius at which δ_e has fallen to $1/e^2$ of its value at $R = 0$.)

Niemeyer & Jedamzik started their simulations exactly at horizon crossing time, when $L = 1$, and this implies nonlinear amplitude of the initial δ in order to get black hole formation. As was noted by Shibata & Sasaki [44], perturbing just energy density corresponds to the initial conditions with comparable components of growing and decaying modes, and this seriously affects the evolution of the perturbation. To investigate this we mostly started with perturbations which were still on length-scales much larger than the horizon scale [$R_0/R_H \geq 5$] and were well within the linear regime [typically $\delta \sim 10^{-2}$]. Setting initial conditions within the linear regime makes it easy to specify consistent density and velocity perturbations representing better a purely growing mode: δ_e grows linearly with time and the associated velocity perturbation is given roughly by

$$\delta_U(R) \simeq -\frac{\delta_e}{4}, \tag{4.43}$$

where δ_U is defined in the same way as for δ_e in equation (4.38):

$$\delta_U(R) \equiv \frac{U - U_b}{U_b} = \frac{\delta U}{U_b} \tag{4.44}$$

with $U_b(R) = H_b R_b$ being the velocity field of the background Hubble flow. (We are here considering adiabatic perturbations with a Newtonian gauge, in which the perturbations do

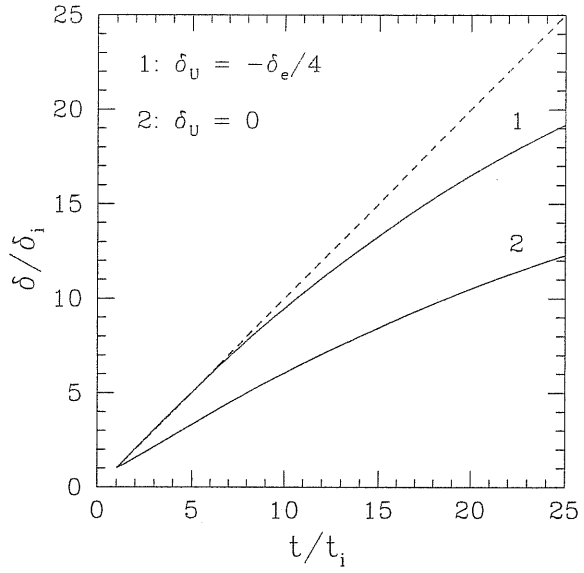

Figure 4.7: This plot shows the time evolution of energy density perturbation amplitude with (line 1) and without (line 2) an initial perturbation of the radial velocity U, as given by 4.43. The solid line is a straight line with gradient equal to 1, representing the theoretical linear evolution of a pure growing mode.

not generate off-diagonal components of the metric.) Expression (4.44) is obtained from (2.49)

$$\delta H = -\frac{1}{3(1+\gamma)}\left[\dot{\delta e} - 3H_b\gamma\delta e\right] \tag{4.45}$$

with the perturbation in R here being neglected because δe and δU are expressed as functions of the spatial coordinate R that in this approach is considered as an independent quantity. Although this is not completely correct, it allows us to get a very reasonable description of a pure growing mode in the linear regime, considering $U = U_b + \delta U = (H_b + \delta H)R_b$.

In Figure 4.7 we see more in detail the importance of including the perturbation δ_U given by (4.43), plotting the amplitude evolution against time, with δ being normalized to its initial value. The perturbation used has an initial length scale $R_0 = 5R_H$ while the final time corresponds to the horizon crossing time, when $R_0 = R_H$ (remember that $R_0/R_H \propto t^{1/2}$). The linear regime is represented by the first part of the evolution plotted in Figure 4.7 (until $t/t_i \sim 10$) and the straight dashed line represents the linear behaviour that a pure growing mode has in the linear regime. The solid line 1 represents an energy density perturbation with an associated initial perturbation also in the radial component of the four velocity. The solid line 2 instead, represents the same energy density perturbation without perturbing the four velocity at the initial time. The difference between the solid line 1 (with initial gradient $\simeq 1$) and solid line 2 (with initial gradient $\simeq 1/2$) is very clear showing explicitly that, without perturbing U by use of (4.43), a significant component of decaying mode is present, giving later with the evolution a completely different value of the amplitude later in the evolution.

4.3 Description of the calculations

4.3.1 Evolution of supercritical perturbations ($\delta > \delta_c$)

In this sub-section, we describe results from representative evolutions leading to black hole formation, carried out using the null-slicing formulation.

Before moving on to new calculations, we first needed to check on whether our code did reproduce the results of Niemeyer & Jedamzik [39] when we used their choice of initial conditions and a simple exponential grid similar to theirs. We found extremely close agreement. For perturbations with the initial δ only slightly larger than the critical value δ_c, the masses of the black holes produced, M_{BH}, follow a scaling law:

$$M_{BH} = K(\delta - \delta_c)^{\gamma} M_H(t_H), \tag{4.46}$$

where K and γ are constants and $M_H(t_H)$ is the cosmological horizon mass at the horizon-crossing time t_H (i.e. when $R_0(t_H) = R_H(t_H)$). The type of behaviour given by (4.46) is familiar from the literature on critical collapse (which, however, is generally considering collapse under simpler circumstances and not within the context of an expanding universe). Our results match very closely with those of [39], with $\delta_c \simeq 0.67$ for the Mexican-hat profile and $\simeq 0.71$ for the polynomial and Gaussian profiles and with γ between $0.36 - 0.37$ in each case. These values for γ are very close to the value 0.356... calculated semi-analytically for the same equation of state within the standard critical collapse scenario [81].

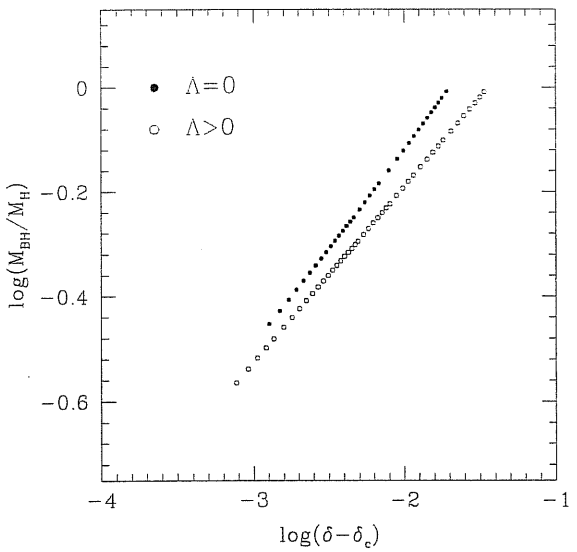

Figure 4.8: Scaling behaviour for M_{BH} as a function of $(\delta - \delta_c)$ calculated for growing-mode Mexican-hat perturbations specified within the linear regime. The filled circles refer to the standard calculation discussed in section 3.2, while the open circles are for a calculation including a non-zero cosmological constant Λ, as discussed in section 3.3, giving $y = 3.0 \times 10^{-3}$.

Following these initial calculations to reproduce previous results, we then carried out further ones starting from approximate growing-mode perturbations specified within the linear regime

and with length-scales larger than the cosmological horizon. These perturbations were evolved with the Misner-Sharp code until the moment when they entered the horizon and the current value of δ was then calculated for use as our measure of perturbation amplitude in the discussion of scaling laws. Having done this, we switched to the Hernandez-Misner code for completing the calculation.

Plotting the eventual black hole mass against $(\delta - \delta_c)$, we obtained scaling curves very similar to those of [39] (and with almost identical values of γ) but with substantially different values for δ_c: for Mexican-hat perturbations, we found $\delta_c \simeq 0.43$ and for polynomial perturbations, $\delta_c \simeq 0.47$. Our scaling-law results for Mexican-hat perturbations are shown as the $\Lambda = 0$ curve in Figure 4.8. The reason for the changed values of δ_c is clear: in [39] the initial perturbations, specified at the horizon-crossing time, had part of their amplitude contributed by a decaying-mode component which then rapidly decreased leaving only the growing-mode part visible. Only the part of the perturbation amplitude corresponding to the growing mode is relevant for the black hole formation and so the effective δ is smaller than that calculated in [39].

Noting the work of Hawke & Stewart (2002) [42] and the fact that the horizon-scale is an important length-scale in the problem, we do not know if the linear scaling law would continue to indefinitely small values of M_{BH} and $(\delta - \delta_c)$ or, instead, if it would level off at some minimum value of M_{BH}. Confirming this behaviour in the case of growing-mode perturbations starting in the linear regime is of great interest but requires refinement of our present code to increase resolution and understanding better the reason for the appearing of strong shocks when δ is sufficiently close to δ_c. We return to this in Chapter 6, with the fundamental change in the initial conditions described in the following chapter.

Figure 4.9 shows some more detailed results for a particular representative case within the linear scaling regime. This run starts from a growing-mode Mexican-hat perturbation with $R_0/R_H = 5$ giving $(\delta - \delta_c) = 2.37 \times 10^{-3}$ at horizon crossing, which leads to formation of a black hole with $M_{BH} = 0.4415\, M_H(t_H)$. The top two panels show the evolution of the lapse f and the corresponding behaviour of the fluid worldlines. The interpretation of the collapse of the lapse is particularly clear when an observer-time formulation is used: as $f \to 0$, the redshift of outgoing signals increases and the evolution as seen by a distant observer becomes frozen, corresponding to black hole formation (see also the small inset where $\log f$ is plotted). Note, however, that strictly "black hole formation" occurs only asymptotically in the future according to this formulation. In the plot for the worldlines, one can see the separation between the matter which goes to form the black hole and the matter which continues to expand, with a semi-evacuated region being formed between them. Note that some of the outer material first decelerates but then accelerates again before crossing this semi-evacuated region to fall into the black hole. The bottom left-hand panel of Fig. 4.9 shows the behaviour of the ratio $2M/R$, plotted against R at successive times. The event horizon corresponds to the asymptotic location of the outermost trapped surface, where $D_k R = 0$ and $R = 2M$. For the present purposes, we need an operational definition for calculating M_{BH}, bearing in mind that the black hole is only formed asymptotically and that further material may continue to accrete. The bottom left-hand panel of Fig. 4.9 shows the approach of $2M/R \to 1$: our operational definition for M_{BH} is to set it equal to the value of M at the maximum of this curve when $(1 - 2M/R)$

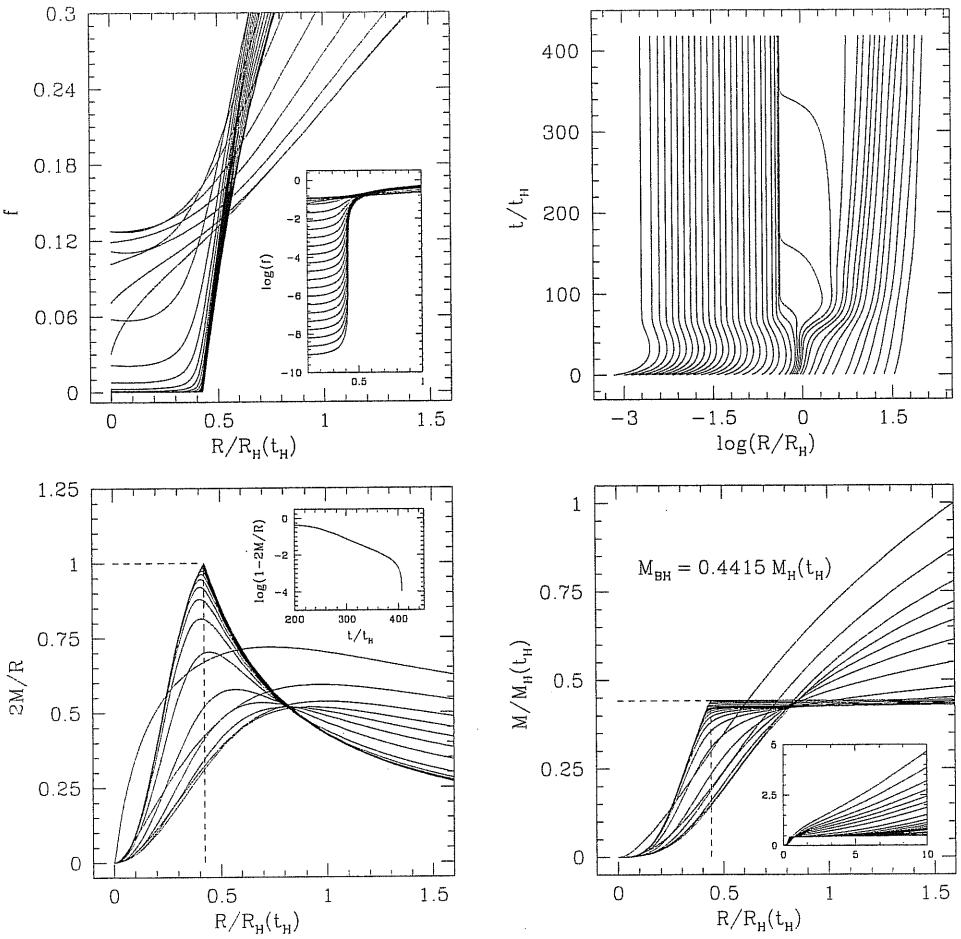

Figure 4.9: A typical evolution leading to black hole formation: the initial perturbation had a Mexican-hat profile and gave $(\delta - \delta_c) = 2.37 \times 10^{-3}$ at the horizon crossing time. The top left-hand panel shows the behaviour of the lapse function (the time sequence of the curves goes from bottom to top on the right hand side); the top right-hand panel shows the fluid-element worldlines (the time is measured in units of the horizon-crossing time t_H). The bottom left-hand panel shows the profile of $2M/R$ at different times; the bottom right-hand panel shows the corresponding evolution of the mass-energy (in both of these panels, the time sequence of the curves goes from top to bottom on the right hand side).

first becomes smaller than 10^{-4}. The bottom right-hand panel shows a corresponding plot for M against R. It can be seen that the profiles for M become very flat just outside the black hole region at late times, a consequence of the very low densities being reached there (less than 10^{-4} of the background density at the horizon-crossing time). The small inset shows the continuation of this figure up to larger radial scales. For calculations with δ closer to δ_c, the rarefactions formed become increasingly deep, and one sees strong shock waves appearing at the outer edge of the under-dense region.

4.3.2 Evolution of super-critical perturbations when $\Lambda > 0$

We were also interested to investigate the effect for PBH formation of including a cosmological constant large enough to affect the dynamics. We recognize that this is a highly idealised scenario since the present-day cosmological constant would have had negligible effect in the early universe and other vacuum energies present after inflation are unlikely to have been constant in time (e.g. quintessence). However, it is of conceptual interest to find out what the behaviour would be in this hypothetical case. A cosmological constant Λ is equivalent to a false vacuum with energy density $e_v = \Lambda/8\pi$ and pressure $p_v = -\Lambda/8\pi$. Its effect can be included by adding these terms onto the standard energy density e and pressure p wherever those appear.

A positive Λ eventually causes the expansion of the universe as a whole to start accelerating and acts against the growth of overdensities, while a negative Λ would aid general collapse. (The equations governing the background expansion when $\Lambda \neq 0$ are summarised in the Appendix A.) As the background density decreases with time, the cosmological constant becomes progressively more important until, when e_v becomes greater than e, the deceleration is reversed and becomes an acceleration [see equation (A.2)]. It is convenient to introduce a quantity y, the ratio between the vacuum energy and the total energy in the uniform background

$$y \equiv \frac{e_v}{e + e_v}, \tag{4.47}$$

which can then be written as

$$y = \frac{4}{3}\Lambda M_H^2, \tag{4.48}$$

since $M_H = \frac{4}{3}\pi {R_H}^3 (e + e_v)$ with $R_H = 2M_H$ (Note that this type of relation holds for the cosmological horizon in the same way as for a black hole event horizon)[2]. In the following, we will use y as a general measure of the importance of the Λ term, with M_H being measured at the horizon-crossing time for a perturbation with $\delta = \delta_c$. The influence of Λ during formation of a black hole of mass M_{BH} can similarly be characterised by the quantity ΛM_{BH}^2 and so, for a given Λ, is greatest for large black holes.

In making computations with $\Lambda > 0$, it is particularly important to start the calculation at an early time when the perturbation has a length-scale larger than the horizon. For appreciating its effects, one wants Λ to be sufficiently large so as to make a significant difference for the collapse, but not so large that it creates a problem for constructing the null-slice initial data. By starting the calculation sufficiently early, this can be achieved although the values of y which we will be considering are all very small (in the range $10^{-3} - 10^{-2}$).

The qualitative picture of collapses leading to black hole formation is not changed very greatly by the presence of a Λ term but there are significant differences in the parameters of the scaling law. We started all of these calculations with perturbations at five times the horizon scale (i.e. $R_0/R_H = 5$).

[2]Both are trapped surfaces. A black hole event horizon is the asymptotic location of the outermost trapped surface for outgoing light-rays whereas the cosmological horizon is the innermost trapped surface for incoming light rays.

The impact of Λ on the scaling law can be seen in Figure 4.8: γ decreases for $\Lambda > 0$ and for sufficiently small Λ is found to follow a linear relationship

$$\gamma(\Lambda) \simeq \gamma(0) - 8.3\, y. \tag{4.49}$$

The critical amplitude δ_c *increases* with increasing Λ and also follows a linear relationship:

$$\delta_c(\Lambda) \simeq \delta_c(0) + 0.98\, y. \tag{4.50}$$

This behaviour can be interpreted as follows: a positive Λ acts against collapse, so that corresponding black hole masses will be lower and the threshold amplitude δ_c will be raised. For a given Λ, its influence is greater for larger black-hole masses than for smaller ones ($\propto M_{BH}^2$) and this gives rise to the observed decrease in γ.

4.3.3 Evolution of subcritical perturbations ($\delta < \delta_c$)

For subcritical perturbations with δ considerably less than δ_c, the perturbation initially grows but then subsides back into the surrounding medium in an uneventful way. However, for perturbations with δ sufficiently close to δ_c, some very interesting behaviour is seen and we present results from a representative case of this in the present subsection. Our calculations for subcritical perturbations use only the Misner-Sharp code.

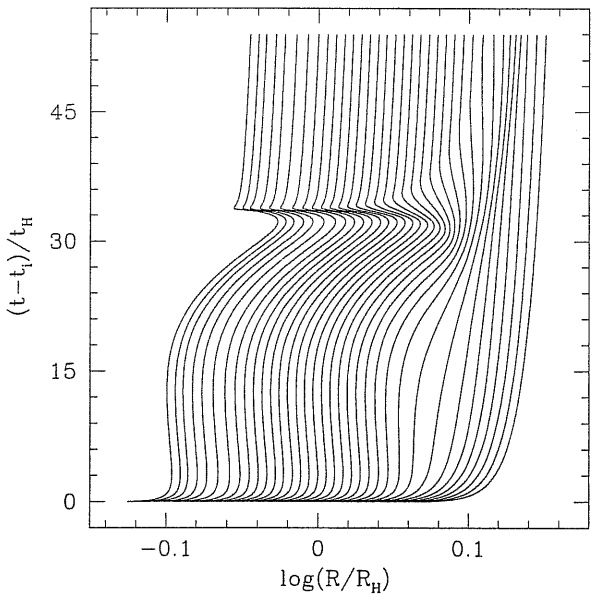

Figure 4.10: Worldlines for a Mexican-hat perturbation with $(\delta - \delta_c) = -3.0 \times 10^{-3}$). This plot shows alternating collapse and expansion of the perturbed region while the outer material continues to expand uniformly. The "cosmic" time is measured in units of the time at horizon crossing.

The run presented starts with a Mexican-hat perturbation specified in the linear regime, with $(\delta - \delta_c = -3 \times 10^{-3})$. In Figure 4.10, the fluid worldlines are plotted and the main features of interest can already be seen from this. Figures 4.11 and 4.12 then show details of

the evolution of the energy density e and the radial velocity U. Figure 4.11 shows a sequence of snap-shots of these quantities, plotted as a functions of R, at key moments during the evolution. Figure 4.12 shows the time evolution of these quantities at three (comoving) locations: near the centre of the perturbation, at an intermediate region (mid-way through the collapsing matter) and at the edge of the grid where the fluid is unperturbed.

The evolution can be summarized in terms of the following steps (see particularly Figures 4.10 and 4.11):

1. Initially, the perturbation has very small amplitude ($\delta_e \sim 10^{-2}$) and its length-scale is five times the horizon scale; the perturbation amplitude then grows within the expanding fluid. The deceleration in the perturbed region is larger than that in the unperturbed region and its expansion lags progressively behind that of the outer matter until eventually it starts to re-contract shortly after horizon crossing. The maximum infall velocity reached is, however, rather small [see row (a) of Figure 4.11] which is for a time considerably after horizon crossing, when the perturbation has become very nonlinear]. The infall can be clearly seen in Figures 4.10 and 4.11 but is only just visible in the third frame of Figure 4.12.

2. The contraction is not strong enough to produce a black hole and the fluid bounces out again [row (b)], expanding until it encounters the surrounding matter which did not participate in the contraction. A compression wave forms where the two regions of fluid meet, while the density becomes very low at the centre of the perturbation [row (c)].

3. The compression wave proceeds out into the surrounding material [row (d)] but also some matter is sent back into the middle of the rarefaction where it undergoes a second bounce which is much more extreme than the first with a very abrupt change of velocity in the central regions (as can be seen from Figure 4.12). Whereas the outward moving compression is damped geometrically as it proceeds to spherical surfaces with progressively larger areas, the inward-moving wave of material is geometrically amplified by the inverse process. The reason for the second collapse and bounce being more violent than the first is that while the first is a collapse of an overdensity which is resisted throughout by internal pressure, the second is essentially the collapse of a "shell" with near vacuum inside it and is hence close to free-fall until just before the bounce.

4. The compression wave formed by the second bounce propagates out into the surrounding medium following the first one [row (e)]. Both proceed to damp geometrically and eventually the medium returns to a uniform state. Note that the second compression wave is very steep fronted (see Figure 4.11) but is not quite a shock. It is likely that that genuine shocks would be seen for perturbations with δ closer to δ_c.

It is useful to make some further comments about the plots in Figure 4.12. The left-hand plot shows the density normalized to its initial value at the same comoving location: this shows the variation of the local density against the background of the general decrease in density as the universe expands and allows one to see clearly the local contraction and expansion of

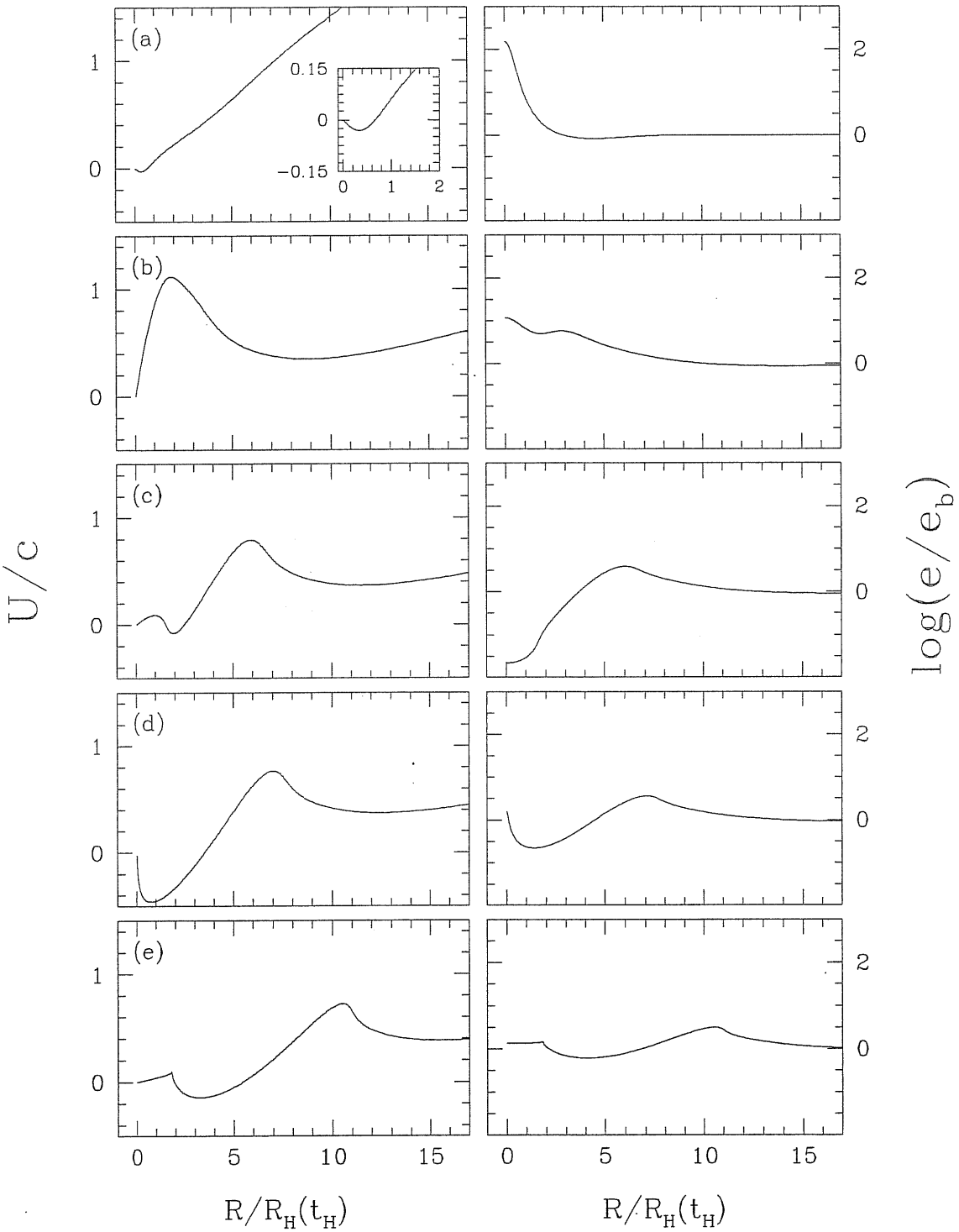

Figure 4.11: Plots of local quantities as functions of $R/R_H(t_H)$: the velocity U/c is shown in the left-hand column and the energy density e/e_b in the right-hand column. The frames correspond to the following values of $(t - t_0)/t_H$: (a) 7.02; (b) 25.92, (c) 31.67; (d) 33.64; (e) 40.11. Note that R_H is increasing with time and so points with $R/R_H(t_H) > 1$ can be within the current horizon scale at times after horizon-crossing.

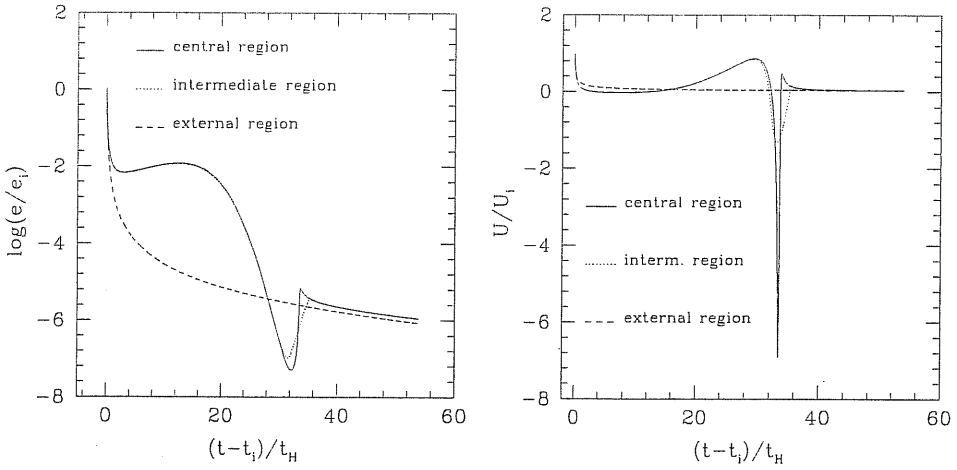

Figure 4.12: Evolution of the energy density e and radial velocity U at three (comoving) locations: near to the centre of the perturbation, at an intermediate region and at the edge of the grid where the fluid is unperturbed. Each quantity is measured in units of its initial value at the same comoving location.

the fluid. Initially, the perturbed region is also still expanding but it then starts to contract when the perturbation amplitude has reached a high enough value. The right-hand plot shows the local value of the radial velocity also normalized to its initial value at the same co-moving location. This has a very different behaviour from that of the energy density, with the inward velocity during the second collapse being very much greater than that during the first and the second bounce being far more abrupt. We see just two bounces in our calculation: after this the expansion of the universe prevents further ones, although we expect that more bounces would be seen for an initial perturbation with δ closer to δ_c.

In this chapter the treatment used to set the initial conditions gives an approximate description of pure growing mode perturbations. This has been useful to clarify the discrepancy observed by Green et. al [43]. In the next chapter we will present a more sophisticated treatment that will allow us to describe pure growing mode perturbations more accurately.

Chapter 5

Initial conditions in terms of a curvature perturbation

In this chapter we will present an analytical calculation to reformulate the problem of imposing initial conditions for PBH formation introducing the perturbations as functions of only one component, the curvature profile. We will see that this enables us to specify a purely growing mode more precisely than in Chapter 4, that is very useful to connect our initial conditions with conditions coming from inflation.

5.1 Introducing a Curvature perturbation

We will now rewrite the Misner-Sharp equations in a perturbative form to derive how the different variables depend on a specified curvature perturbation imposed at an initial time. To explain the idea, we start by writing the Friedmann metric that describes the homogeneous and isotropic background of the universe,

$$ds^2 = -dt^2 + s^2(t)\left[\frac{dr^2}{1-Kr^2} + r^2\left(d\theta^2 + \sin^2\theta d\phi^2\right)\right] \tag{5.1}$$

where $s(t)$ is the scale factor and K is the curvature parameter that is equal to 0, $+1$ and -1 for flat, closed and open universes.

From the linear theory of cosmological perturbations [6] we know that a comoving curvature perturbation $\mathcal{R}$ is related to a corresponding density perturbation and that, when the length scale of the perturbation is much larger than the horizon scale, the curvature perturbation is time independent, because pressure gradients are negligible. (Later we give a brief review of the main relations for curvature perturbations, as found in the literature). In two recent papers, Lyth et al. [82] and Langlois & Vernizzi [83] have shown that a quantity connected with curvature perturbations is constant in time even away from the linear regime. Our method is closely related to those results.

Remembering the general metric in spherical symmetry of the Misner-Sharp scheme, given by expression (4.1)

$$ds^2 = -a^2\,dt^2 + b^2\,dr^2 + R^2\left(d\theta^2 + \sin^2\theta d\varphi^2\right), \tag{5.2}$$

we want to consider here PBH formation in a spatially flat universe with $K = 0$. To do this one can see that, introducing a profile $K = K(r)$ into (5.1), the FRW metric modified in this way is still a solution of the Einstein equations if we perturb consistently the quantities a, b and R in (5.2), which in the background are equal to 1, $s(t)$ and $s(t)r$ respectively. The perturbations of these quantities tend to 0 in the limit of time $t \to 0$. This makes the modified FRW metric with $K = K(r)$ an asymptotic solution of the Einstein equations in the limit $t \to 0$, because $K(r)$ is time independent by definition, and so it should be built inside the geometry of the space time from the beginning. Therefore it seems to us an intuitive and natural choice to represent the curvature perturbation described in Chapter 2 with the function $K(r)$ for perturbations with scales much larger than the horizon length, and to solve the system of perturbed differential equations in order to calculate how the set of variables depends on $K(r)$ in this regime.

To develop the perturbative analysis for all the quantities appearing in the Misner-Sharp equations we need to solve the following system of differential equations:

$$\dot{R} = aU \tag{5.3}$$

$$\frac{\dot{b}}{b} = a\frac{U'}{R'} \tag{5.4}$$

$$\frac{a'}{a} = -\frac{\gamma}{1+\gamma}\frac{e'}{e} \tag{5.5}$$

$$\dot{M} = -4\pi\gamma e R^2 \dot{R} \tag{5.6}$$

$$M' = 4\pi e R^2 R' \tag{5.7}$$

$$\frac{R'^2}{b^2} = 1 + U^2 + \frac{2M}{R} \tag{5.8}$$

where the dot and dash denote differentiation with respect to t and r respectively, and we have used the equation of state (1.20) to express the pressure as function of energy density, (4.7) to give an expression for Γ, and ρ can be calculated later with equation (4.9). We will treat the parameter γ generally, as $\gamma = \gamma(t)$, focusing later on the simplest case of one fluid component described by constant γ.

The background value of the energy density (indicated with the suffix "b") is calculated with the Friedmann equation

$$\left(\frac{\dot{s}}{s}\right)^2 = H_{\mathrm{b}}^2 = \frac{8\pi}{3} e_{\mathrm{b}}\,, \tag{5.9}$$

while the background value of the other quantities is derived from the FRW metric and the above set of equations (5.3 - 5.8).

$$a_{\mathrm{b}} = 1 \tag{5.10}$$

$$b_{\mathrm{b}} = s(t) \tag{5.11}$$

$$R_{\mathrm{b}} = s(t) r \tag{5.12}$$

$$M_{\mathrm{b}} = \frac{4}{3}\pi e_{\mathrm{b}} R_{\mathrm{b}}^3 \tag{5.13}$$

$$U_{\mathrm{b}} = H_{\mathrm{b}} R_{\mathrm{b}} = \dot{s}(t)\, r \tag{5.14}$$

When the perturbation length scale is well outside the horizon, the perturbations of all quantities, except for curvature, are taken to be very small with respect to the background

values and can be treated in terms of first order perturbations. It is useful to parametrise the scale of the perturbations using an adimensional parameter ϵ defined as the ratio of two physical distances, the physical length scale of the overdensity in the perturbation $R_0 = s(t)r_0$ and the horizon scale $R_H = H_{\rm b}^{-1}$.

$$\epsilon \equiv \left(\frac{R_H}{R_0}\right)^2 = \left(\frac{1}{H_{\rm b} s r_0}\right)^2 = \frac{1}{\dot{s}^2 r_0^2} << 1 \tag{5.15}$$

By definition, ϵ is related only to the background quantities and is a function only of time, with the behaviour of its time derivative being given by

$$\frac{\dot{\epsilon}}{\epsilon} = -2\frac{\dot{s}}{s} - \frac{\dot{e}_{\rm b}}{e_{\rm b}} = -2\frac{\dot{s}}{s} + 3(1+\gamma)\frac{\dot{s}}{s} = (1+3\gamma)\frac{\dot{s}}{s}\,, \tag{5.16}$$

$$\xi \equiv \ln(s)\,, \quad \frac{s}{\dot{s}}\frac{\partial}{\partial t} \equiv \frac{\partial}{\partial \xi} \equiv (\,)^{\cdot}\,, \quad \frac{\partial}{\partial r} \equiv (\,)'\,. \tag{5.17}$$

In particular it is important to point out that expression (5.16) is a consequence of energy conservation law and that it holds also when γ is a general function of time.

Introducing ϵ explicitly, we now define the perturbations of each quantity as:

$$R = R_b(1+\epsilon\tilde{R}) \tag{5.18}$$

$$U = H_b R(1+\epsilon\tilde{U}) \tag{5.19}$$

$$b = \frac{R'}{\sqrt{1-K(r)r^2}}(1+\epsilon\tilde{b}) \tag{5.20}$$

$$a = 1+\epsilon\tilde{a} \tag{5.21}$$

$$e = e_b(1+\epsilon\tilde{e}) \tag{5.22}$$

$$M = \frac{4}{3}\pi e_b R^3(1+\epsilon\tilde{M}) \tag{5.23}$$

where it should be noted that the quantities outside the brackets in the expressions for U, b and M on the left hand side are not just the background quantities. Although this choice might seem non-intuitive at first sight, we find that it simplifies the final form of the equations. If the value of ϵ is small enough, we are allowed to make a linear perturbation analysis, apart from the amplitude of the curvature perturbation profile $K(r)$ which represents the source of perturbations in this description. The aim is to express all of the tilda-quantities as functions of $K(r)$.

We can start to solve the problem perturbing equation (5.3), and using expressions (5.16) and (5.17) we get,

$$\frac{\dot{R}}{R} = \frac{aU}{R}$$

$$\frac{\dot{s}}{s} + (\epsilon\tilde{R})^{\cdot} = \frac{\dot{s}}{s}(1+\epsilon\tilde{a})(1+\epsilon\tilde{U})$$

$$\frac{s}{\dot{s}}\frac{\dot{\epsilon}}{\epsilon}\tilde{R} + \frac{\partial\tilde{R}}{\partial\xi} = \tilde{a} + \tilde{U}$$

$$(1+3\gamma)\tilde{R} + \frac{\partial\tilde{R}}{\partial\xi} = \tilde{a} + \tilde{U}\,. \tag{5.24}$$

Perturbing equation (5.4) we get

$$\dot{R}' = (aU)'$$
$$(\epsilon\tilde{b})^{\cdot} = -\frac{a'U}{R'}$$
$$\dot{\epsilon}\tilde{b} + \epsilon\dot{\tilde{b}} = -\epsilon\tilde{a}'\frac{\dot{s}}{s}r$$
$$(1+3\gamma)\tilde{b} + \frac{\partial\tilde{b}}{\partial\xi} = -r\tilde{a}'\,. \tag{5.25}$$

Perturbing equation (5.5) we get

$$\tilde{a}' = -\frac{\gamma}{1+\gamma}\tilde{e}'\,,$$

which is simply integrated as

$$(1+\gamma)\tilde{a} + \gamma\tilde{e} = 0\,. \tag{5.26}$$

Perturbing equation (5.6) we get

$$\frac{1}{3}(1+\epsilon\tilde{M})\left[\frac{\dot{e}_b}{e_b} + 3\frac{\dot{R}}{R} + (\epsilon\tilde{M})^{\cdot}\right] = \gamma(1+\epsilon\tilde{e})\frac{\dot{R}}{R}\,,$$

that, using (5.16), we can write as

$$\frac{\dot{e}_b}{e_b} = -3(1+\gamma)\frac{\dot{s}}{s}$$
$$-3(1+\gamma)\frac{\dot{s}}{s} + 3(1+\gamma)\frac{\dot{R}}{R} - 3(1+\gamma)\frac{\dot{s}}{s}\epsilon\tilde{M} + (\epsilon\tilde{M})^{\cdot} +$$
$$+3\frac{\dot{s}}{s}\epsilon\tilde{M} + 3\gamma\frac{\dot{R}}{R}\epsilon\tilde{e} = 0\,.$$

Using now equation (5.3) we get some simplifications

$$\dot{\epsilon}\tilde{M} + \epsilon\dot{\tilde{M}} - 3\gamma\frac{\dot{s}}{s}\epsilon\tilde{M} + 3\gamma\frac{\dot{s}}{s}\epsilon\tilde{e} + 3(1+\gamma)(\dot{\epsilon}\tilde{R} + \epsilon\dot{\tilde{R}}) = 0\,,$$

and finally using equation (5.24) and (5.26) we get

$$\tilde{M} + \frac{\partial\tilde{M}}{\partial\xi} = -3(1+\gamma)\tilde{U}\,. \tag{5.27}$$

Perturbing equation (5.7) we get

$$\frac{1}{3}(1+\epsilon\tilde{M})\left[3\frac{R'}{R} + (\epsilon\tilde{e}')\right] = (1+\epsilon\tilde{e})\frac{R'}{R}\,,$$

that after some algebra can be written as

$$\tilde{e} = \frac{1}{3r^2}(r^3\tilde{M})' . \tag{5.28}$$

Finally we have to perturb equation (5.8)

$$\left[(1-K(r)r^2)(1-2\epsilon\tilde{b})-1\right] = \frac{\dot{s}^2}{s^2}R^2(1+2\epsilon\tilde{U}) - \frac{8\pi e_b R^3}{3R}(1+\epsilon\tilde{M}) ,$$

that using (5.9) becomes

$$-\left[K(r)r^2 + 2\epsilon\tilde{b}(1-K(r)r^2)\right] = R^2\frac{\dot{s}^2}{s^2}\epsilon(2\tilde{U}-\tilde{M}) ,$$

and now using expression (5.15) for ϵ:

$$-\left[K(r)r^2 + 2\epsilon\tilde{b}(1-K(r)r^2)\right] = \frac{r^2}{r_0^2}(2\tilde{U}-\tilde{M}) . \tag{5.29}$$

At this point we use the linear regime approximation for perturbations with length-scales larger than the horizon ($\epsilon \ll 1$) that allows the first order term to be neglected, giving

$$\tilde{U} = \frac{1}{2}\left[\tilde{M} - K(r)r_0^2\right] . \tag{5.30}$$

This is the only equation of the system where, at the end of the algebra, $K(r)$ is appearing explicitly. Expression (5.29) shows that the zero order perturbation in curvature (on the left hand side of the Einstein equations) relates to the first order of the other quantities, because of a cancellation of ϵ on the right hand side of (5.29). From the definition of Γ given in (4.7) one can rewrite (5.30) as

$$K(r) = \frac{1-\Gamma^2}{r^2} , \tag{5.31}$$

which is a useful expression to study later the accuracy of the linear approximation as a function of of ϵ. This relation shows also the connection between the profile $K(r)$ and Γ, which is an invariantly defined quantity representing an energy per unit mass.

Now we can solve the system of perturbative equations composed of the four differential equations (5.25, 5.24, 5.27, 5.28), and two algebraic equations (5.26,5.30). Substituting (5.30) into equation (5.27) we get

$$\frac{\partial\tilde{M}}{\partial\xi} + \frac{5+3\gamma}{2}\tilde{M} = \frac{3}{2}(1+\gamma)K(r)r_0^2 , \tag{5.32}$$

and from this expression we can see that it is possible to separate the variables (r,ξ) because, as we have assumed at the beginning, γ is just a function of time related to the background solution (remember that ξ is the logarithmic time defined by (5.17)). We therefore write

$$\tilde{M} = \Phi(\xi)K(r)r_0^2 , \tag{5.33}$$

that gives the following differential equation for the function $\Phi(\xi)$

$$\frac{d\Phi}{d\xi} + \frac{5+3\gamma}{2}\Phi = \frac{3}{2}(1+\gamma)\,. \tag{5.34}$$

Before entering into a detailed discussion of the particular equation of state, we treat for the moment $\Phi(\xi)$ as a free function and solve the system of perturbed equations. Expression (5.33) is the solution for the mass perturbation $\tilde{M}$ and inserting this into (5.28) and subsequently making all of the consequent substitutions in (5.26) and (5.30) we get the general expression for the energy density perturbation $\tilde{e}$, lapse perturbation $\tilde{a}$ and radial velocity perturbation $\tilde{U}$:

$$\tilde{e} = \Phi(\xi)\frac{1}{3r^2}\left[r^3K(r)\right]' r_0^2 \tag{5.35}$$

$$\tilde{a} = -\Phi(\xi)\frac{\gamma}{1+\gamma}\frac{1}{3r^2}\left[r^3K(r)\right]' r_0^2 \tag{5.36}$$

$$\tilde{U} = \frac{1}{2}\left[\Phi(\xi)-1\right]K(r)r_0^2 \tag{5.37}$$

Substituting these solutions into (5.24) and (5.25) we find two differential equations for the perturbation quantities $\tilde{R}$ and $\tilde{b}$, given by

$$(1+3\gamma)\tilde{R} + \frac{\partial\tilde{R}}{\partial\xi} = -\Phi(\xi)\frac{\gamma}{1+\gamma}\frac{1}{3r^2}\left[r^3K(r)\right]' r_0^2 + \frac{1}{2}\left[\Phi(\xi)-1\right]K(r)r_0^2\,, \tag{5.38}$$

$$(1+3\gamma)\tilde{b} + \frac{\partial\tilde{b}}{\partial\xi} = \frac{\gamma}{(1+\gamma)}r\left[\frac{1}{3r^2}\left[r^3K(r)\right)'\right]'\Phi(\xi)\,, \tag{5.39}$$

that can be solved introducing two new free functions of time $I_1(\xi)$ and $I_2(\xi)$ related to $\Phi(\xi)$,

$$\tilde{R} = -I_1(\xi)\frac{1}{3r^2}\left[r^3K(r)\right]' r_0^2 + I_2(\xi)\frac{K(r)}{2}r_0^2\,, \tag{5.40}$$

$$\tilde{b} = I_1(\xi)r\left[\frac{1}{3r^2}\left(r^3K(r)\right)'\right]' r_0^2\,. \tag{5.41}$$

The relation between $I_{1,2}(\xi)$ and $\Phi(\xi)$ is obtained introducing (5.40) and (5.41) into (5.38) and (5.39).

$$\frac{dI_1(\xi)}{d\xi} + (1+3\gamma)I_1(\xi) = \frac{\gamma}{1+\gamma}\Phi(\xi) \tag{5.42}$$

$$\frac{dI_2(\xi)}{d\xi} + (1+3\gamma)I_2(\xi) = \left[\Phi(\xi)-1\right] \tag{5.43}$$

This completes the general solution of the system of equations that is formed by expressions (5.33), (5.35), (5.36), (5.37), (5.40), (5.41) for the set of perturbations and by the first order differential equations (5.34), (5.42), 5.43) for the free functions. The elegance and simplicity of this solution is in the separation in the perturbed quantities between the time evolution given by ϵ and Φ and the space dependence given by $K(r)$.

Now we discuss the nature of the free functions and can understand explicitly how they are related to the background solution. In general if the matter of the universe is described by

different components (labelled by the index"i") with different behaviours, the function γ is a function of time defined with respect to the composition of the matter of the universe. We can write therefore

$$\gamma(s) \equiv \frac{\sum_i p_i}{\sum_i e_i} = \frac{\sum_i \gamma_i e_i}{\sum_i e_i} = \frac{\sum_i \gamma_i e_i}{e} \tag{5.44}$$

where scale factor s has been used as a time variable for convenience. At the initial time it is possible to express the presence of each component in the universe determining the fractional amount f_i with the correspondent coefficient γ_i, having for each component

$$e_i = f_i e \sim s^{-3(1+\gamma_i)}, \qquad \sum_i f_i = 1, \tag{5.45}$$

where f_i and γ_i are constants, because they are measured at a particular time. Therefore

$$\gamma = \frac{\sum_i f_i \gamma_i s^{-3(1+\gamma_i)}}{\sum_i f_i s^{-3(1+\gamma_i)}} \tag{5.46}$$

$$Q(s) \equiv \textstyle\sum_i f_i s^{-3(1+\gamma_i)} \propto e(s) \propto H^2(s) \tag{5.47}$$

$$s\frac{dQ}{ds} = \frac{dQ}{d\xi} = -3\sum_i f_i s^{-3(1+\gamma_i)} - 3\sum_i \gamma_i f_i s^{-3(1+\gamma_i)} = -3Q - 3\gamma Q$$

$$\frac{dQ}{d\xi} = -3(1+\gamma)Q \quad \text{or} \quad \frac{3(1+\gamma)}{2} = -\frac{1}{2}\frac{dQ}{Qd\xi} = -\frac{1}{H}\frac{dH}{d\xi} \tag{5.48}$$

Using this last equation for γ in equation (5.34) one obtains

$$\frac{d\Phi}{d\xi} + \left(1 - \frac{1}{H}\frac{dH}{d\xi}\right)\Phi = -\frac{1}{H}\frac{dH}{d\xi},$$

and this equation can be solved with a general solution of the form

$$\Phi = Fe^{\mu}.$$

After substitution, it is found that F and μ have to satisfy the following differential equations

$$\frac{dF}{d\xi} = -\frac{1}{H}\frac{dH}{d\xi}e^{-\mu},$$

$$\frac{d\mu}{d\xi} + 1 - \frac{1}{H}\frac{dH}{d\xi} = 0,$$

giving

$$e^{-\mu} = e^{\ln s - \ln H} = \frac{s}{H},$$

$$F = \frac{s}{H} - \int_0^s \frac{ds'}{H},$$

and then

$$\Phi(s) = 1 - \frac{H(s)}{s}\int_0^s \frac{ds}{H(s)}. \tag{5.49}$$

Finally we have to solve the two differential equations for I_1 and I_2 that are both of the same form,

$$s\frac{I(s)}{ds} + (1+3\gamma)I(s) = F(s) \tag{5.50}$$

where $F(s) = \frac{\gamma(s)}{1+\gamma(s)}\Phi(s)$ in the case of $I(s) = I_1(s)$, while $F(s) = \Phi(s) - 1$ when $I(s) = I_2(s)$. From the expression (5.16) it is possible to write

$$1 + 3\gamma = \frac{1}{H\epsilon}\frac{d\epsilon}{dt} = H^2 s^2 \left(s\frac{d(1/H^2 s^2)}{ds} \right) \tag{5.51}$$

and this allows the differential equations (5.50) to be written in a form that can easily be integrated,

$$s\frac{d}{ds}\left[\frac{1}{H^2 s^2} I(s)\right] = \frac{1}{H^2 s^2} F(s) \tag{5.52}$$

therefore

$$I(s) = H^2(s)\, s^2 \int_0^s F(s) \frac{1}{H^2(s)\, s^2} \frac{ds}{s}\,, \tag{5.53}$$

which gives the following expressions for the two functions I_1 and I_2:

$$I_1(s) = H^2(s)\, s^2 \int_0^s \frac{\gamma(s)}{1+\gamma(s)} \Phi(s) \frac{1}{H^2(s)\, s^2} \frac{ds}{s}\,, \tag{5.54}$$

$$I_2(s) = H^2(s)\, s^2 \int_0^s (\Phi(s) - 1) \frac{1}{H^2(s)\, s^2} \frac{ds}{s}\,. \tag{5.55}$$

All of the physical quantities are then related in a general and consistent way with three fundamental degrees of freedom in the choice of initial conditions. The first one depends just on time and is given by the time functions $Q(s)$ or $H(s)$ that specify the various components of particles, scalar fields, cosmic strings, etc., present in the Universe at any particular time. In other words the time functions ($\gamma(s)$, $\epsilon(s)$, $\Phi(s)$, $I_1(s)$, $I_2(s)$), that we can calculate from the particular choice of $H(s)$, contain the background history of the Universe, from the beginning until the time of imposing the initial conditions. The second degree of freedom depends just on space and is given by the particular profile chosen for the spatial curvature function $K(r)$. The last degree of freedom is given by the choice of the initial perturbation scale with respect to the horizon scale, chosen such that $\epsilon \ll 1$ in order to make the perturbative analysis self-consistent. In practice we will use the maximum value of this parameter for which the linear approximation is sufficiently precise.

For the rest of this chapter we will concentrate on the simplest case for the equation of state, with γ constant. (In practice in the simulations we will set it equal to $1/3$ because the radiation epoch of the universe is the standard scenario for PBH formation.) This means that the Hubble parameter behaves as

$$H(s) \sim s^{-\frac{3(1+\gamma)}{2}}, \tag{5.56}$$

and the integrated functions Φ, I_1, and I_2 are just constants

$$\Phi = \frac{3(1+\gamma)}{5+3\gamma} \tag{5.57}$$

$$I_1 = \frac{\gamma}{(1+3\gamma)(1+\gamma)}\Phi = \frac{3\gamma}{(1+3\gamma)(5+3\gamma)} \tag{5.58}$$

$$I_2 = \frac{1}{1+3\gamma}(\Phi - 1) = -\frac{2}{(1+3\gamma)(5+3\gamma)} \tag{5.59}$$

In this case, therefore, the tilda-quantities are time independent and the time evolution is determined just by ϵ. This allows us to reproduce easily the standard solution of cosmological perturbation theory when γ is a constant. From (5.16) we can calculate the time evolution of ϵ

$$\epsilon(t) = \epsilon(t_0)\left(\frac{t}{t_0}\right)^{\frac{2(1+3\gamma)}{3(1+\gamma)}}, \tag{5.60}$$

and this is exactly the standard solution of the perturbation equation (2.59).

5.2 General properties of the curvature profile

One important aspect coming from the definition of b given by (5.20) is the mathematical requirement that the argument inside the square root that must be positive,

$$1 - K(r)r^2 > 1 \quad \Rightarrow \quad K(r) < \frac{1}{r^2} \tag{5.61}$$

otherwise in the range of r where the argument of the square root is negative the comoving radius is not defined. This corresponds to the physical condition that a perturbed spherical region of comoving radius r should not already be causally disconnected from the rest of the Universe at early times. Another important property is the conservation of the total energy of the Universe, when the perturbation is made,

$$\int_0^\infty 4\pi r^2 \tilde{e}(r)dr = 0\,, \tag{5.62}$$

that implies

$$\lim_{r\to\infty} r^3 K(r) = 0\,, \tag{5.63}$$

which means also that the Universe remains spatially flat on a large enough scale. A final property of the profile of curvature is the value of r_0 that specifies the length-scale of the overdensity in the perturbation; from (5.35) we have

$$\tilde{e}(r_0) = 0 \quad \Rightarrow \quad K(r_0) + \frac{r_0}{3}K'(r_0) = 0\,. \tag{5.64}$$

Considering the integrated quantity δ defined in Chapter 4 by (4.42), we can see from equation (5.28), that any spherical integral of $\tilde{e}$ is independent of the particular curvature profile used, but depends just on the value of $K(r)$ at the outer edge of the interval. The explicit expression for δ gives so

$$\delta \equiv \left(\frac{4}{3}\pi r_0^3\right)^{-1} \int_0^{r_0} 4\pi \frac{e - e_b}{e_b} r^2 dr = \epsilon(s)\Phi(s)K(r_0)r_0^2\,, \tag{5.65}$$

and we can appreciate from this expression that δ is gauge independent since it is directly proportional to $K(r_0)r_0^2$ which is an invariantly defined quantity. The elegance of this expression is seen in the perfect separation of the different physical contributions: ϵ specifies the linear evolution of the perturbation amplitude in the long wavelength limit, Φ gives the contribution of the equation of state and $K(r_0)r_0^2$ specifies the spatial profile of the perturbation.

Now we show how to link the curvature profile $K(r)$ to the comoving curvature perturbation $\mathcal{R}$ introduced in Chapter 2. To simplify the discussion and avoid referring continually to expressions introduced in the second chapter, we rewrite here the main expressions that we have seen there in more detail. The definition of $\mathcal{R}$ comes from a linear perturbation of the FRW metric, where the spatial part of the metric tensor is given by

$$g_{ij} = s^2 \left[(1 + 2\mathcal{R})\, \delta_{ij} \right] , \tag{5.66}$$

and the calculation of the spatial scalar curvature $R^{(3)}$ gives

$$R^{(3)} = 4\frac{k^2}{s^2}\mathcal{R} , \tag{5.67}$$

where k is the comoving wavenumber associated with the perturbation. The comoving curvature perturbation $\mathcal{R}$ is also connected with the pure growing mode solution of the perturbation equation for the energy density by

$$\frac{\delta e}{e_{\mathrm{b}}} = \frac{2(1+\gamma)}{5+3\gamma}\left(\frac{k}{sH}\right)^2 \mathcal{R} . \tag{5.68}$$

This relation is obtained using a quantity called the "peculiar gravitational potential" Φ_{G} defined as

$$\frac{\delta e}{e_{\mathrm{b}}} = -\frac{2}{3}\left(\frac{k}{sH}\right)^2 \Phi_{\mathrm{G}} , \tag{5.69}$$

that is linked to $\mathcal{R}$ by a first order differential equation

$$\frac{1}{H}\dot{\Phi}_{\mathrm{G}} + \frac{5+3\gamma}{2}\Phi_{\mathrm{G}} = -(1+\gamma)\mathcal{R} , \tag{5.70}$$

that has a pure growing solution given by

$$\Phi_{\mathrm{G}} = -\frac{3(1+\gamma)}{5+3\gamma}\mathcal{R} . \tag{5.71}$$

In the linear perturbation regime, when the length-scale of a perturbation is much larger than the horizon scale, the pressure gradients are negligible and it turns out that $\mathcal{R}$ and Φ_{G} are time independent. This is also connected with the adiabatic condition, that assumes that the inflaton field has only one component, with negligible effects coming from other fields. These characterise the production during inflation of vacuum fluctuations giving the origin of cosmological perturbations.

If we calculate the spatial scalar curvature (see appendix B) with the curvature profile $K(r)$ explicitly written in the metric, we find that

$$R = 6\left[\frac{\ddot{s}}{s}\left(1 + \epsilon\frac{3\gamma-1}{5+3\gamma}\mathcal{K}\right) + \frac{\dot{s}^2}{s^2}\left(1 - \epsilon\frac{2(2+3\gamma)}{5+3\gamma}\mathcal{K}\right) + \frac{\mathcal{K}}{s^2}\right] , \tag{5.72}$$

where

$$\mathcal{K} = K(r) + \frac{r}{3}K'(r) . \tag{5.73}$$

Because the metric is diagonal the spatial component is perpendicular to the time one and

$$R^{(3)} = \frac{6}{s^2}\left[K(r) + \frac{r}{3}K'(r)\right] . \tag{5.74}$$

If we identify $k = 1/r_0$, which is natural because the wave number is representing the inverse of the wavelength of the perturbation, we see that

$$\epsilon = \left(\frac{k}{sH}\right)^2 . \tag{5.75}$$

Using this and comparing equation (5.67) with (5.74) we see that the two equations are the same if we identify

$$\mathcal{R} = \frac{3}{2}r_0^2\left[K(r) + \frac{r}{3}K'(r)\right] \tag{5.76}$$

and the same result is obtained comparing (5.35) with (5.68). We notice also that equation (5.70) is the same as (5.34), in fact the peculiar gravitational potential defined in (5.69) can be written in our terminology as $\Phi_G = -(2/3)\tilde{e}$ and then we can use equation (5.28) to change the variable $\tilde{M}$ to $\tilde{e}$ in (5.34).

We have therefore shown that the comoving curvature $\mathcal{R}$ is directly linked to the curvature profile $K(r)$ even when $\mathcal{R}$ is not a small quantity. The validity of this direct relation is ensured when the length scale of the perturbation is much larger than the horizon scale. The adiabatic statement has an analogy in our formulation of the problem because in our general solution the choice of a profile for $K(r)$ is the only free component that one needs in order to specify the behaviour of a perturbation. Expression (5.76) is very useful for connecting the perturbation profile to the vacuum fluctuations produced during inflation, with equation 2.11 that we rewrite as

$$\mathcal{R} = -\left[H\frac{\delta\phi}{\dot{\phi}}\right]_{t=t_*} . \tag{5.77}$$

5.3 Numerical implementation of the formalism

In this section we make a particular choice for the profile of $K(r)$ in terms of two free parameters. In section 5.3.1 we discuss this particular choice explaining how the curvature specification is inserted into the code and showing how the shapes of the perturbations are modified when we vary the parameters. In section 5.3.2 we make some numerical tests to calculate how small ϵ should be in order to be small enough to make the linear approximation satisfactory.

5.3.1 Parametrisation of the curvature profile

We specify the initial curvature perturbation by giving K as a function of r. However, both r and K are gauge-dependent quantities and so care is needed when transferring the initial perturbation profile onto the grid used for the numerical calculations. The Schwarzschild circumference coordinate R used in the code is invariantly defined and is related to r by $R_b = s(t)r$, where R_b is the background value of R at a co-moving location before introducing the

perturbation. The particular values of $s(t)$ and r are gauge dependent, but what is important is that their product is invariantly defined. Another gauge invariant quantity is the product $K(r)r^2$. We specify $K(r)$ and this then determines the value of r_0 at the outer edge of the overdensity in the perturbation from equation (5.64). We then specify the physical length scale R_0 of the initial perturbation in terms of the initial horizon scale:

$$R_0 = NR_H\,, \tag{5.78}$$

where N is the number of horizon scales inside the scale of the overdensity. We need to choose N such that the perturbation length scale is much larger than the horizon scale and, from the definition of ϵ in (5.15), we have

$$\epsilon = \frac{1}{N^2}\,. \tag{5.79}$$

To have $\epsilon \ll 1$ we need to have $N \gg 1$ and N will be one of the input parameters used to impose the initial conditions. Expression (5.78) gives also a direct link between the scale factor and the value of r_0

$$s(t) = \frac{NR_H}{r_0}\,, \tag{5.80}$$

and we can use this to define the comoving coordinate as

$$r = \frac{R_{\rm b}}{s(t)} = \frac{r_0}{NR_H}R_{\rm b} \tag{5.81}$$

where the value of the circumferential coordinate $R_{\rm b}$ is calculated with equation (4.2), simply integrated for the background universe as

$$R_{\rm b} = \left(\frac{\mu}{4\pi\rho}\right)^{1/3}\,. \tag{5.82}$$

To decide now how to parametrise $K(r)$ we start by making some physical considerations about what could be a reasonable perturbation shape. For a simple and natural description, it is useful to start with a centrally peaked profile of the energy density that looks similar to the Mexican hat profile used in Chapter 4, which means that outside the region of the overdensity there is an under-dense region that tends asymptotically to the flat solution. To describe an energy density profile with these properties one should choose a centrally peaked profile of curvature that tends asymptotically to zero with a suitable continuous function. The continuity should be ensured at least in the first and second derivatives, because these play a key role in the expressions for the perturbation profiles of the different variables. To conserve the common normalisation used in cosmology where a closed universe has a curvature equal to 1, we choose to normalise the curvature profile to have $K(0) = 1$, and then connect this point asymptotically to zero. This is of purely formal convenience however as the scaling is determined when fixing the gauge by comparison with invariantly defined quantities.

We start with a family of curvature profiles based on a Gaussian shape, described by

$$K(r) = \left(1 + \alpha\frac{r^2}{2\Delta^2}\right)\exp\left(-\frac{r^2}{2\Delta^2}\right) \tag{5.83}$$

where α and Δ are two independent parameters. In the particular case $\alpha = 0$, $K(r)$ is exactly Gaussian. To understand the behaviour of this function as the parameters are varied we need to look at its first derivative given by

$$K'(r) = \frac{r}{\Delta^2}\left[\alpha - \left(1 + \alpha\frac{r^2}{2\Delta^2}\right)\right]\exp\left(-\frac{r^2}{2\Delta^2}\right) \tag{5.84}$$

that we use to calculate the value of r_0 as function of α and Δ using (5.83) and (5.64). We find

$$\alpha x_0^2 - (5\alpha - 2)x_0 - 6 = 0\,, \qquad \text{where} \qquad x_0 \equiv \frac{r_0^2}{\Delta^2} \tag{5.85}$$

with the following solutions

$$r_0^2 = 3\Delta^2 \quad \text{if} \quad \alpha = 0 \tag{5.86}$$

$$r_0^2 = \Delta^2\frac{(5\alpha-2)\pm\sqrt{(5\alpha-2)^2+24\alpha}}{2\alpha} \quad \text{if} \quad \alpha \neq 0 \tag{5.87}$$

If α is positive only the solution of (5.87) with the positive sign is acceptable because the other one gives r_0 being negative. If α is negative, both of the solutions are acceptable in these sense, and the one to associate with r_0 is the smaller one, which is anyway the one with the positive sign in front of the square root. The ratio $(r_0/\Delta)^2$ changes with α and its behaviour is plotted in Figure 5.1. From (5.86) and (5.87) we see that, for a given value of α, r_0 is a linear function of Δ.

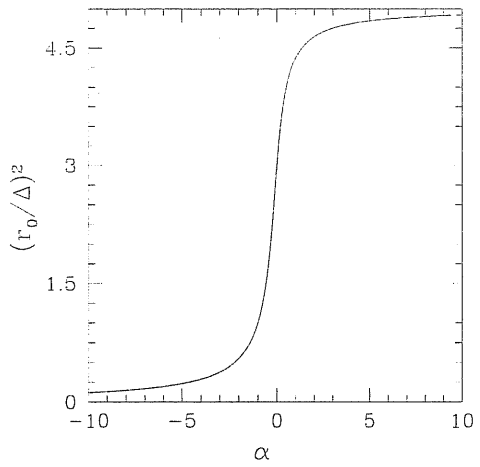

Figure 5.1: The behaviour of $(r_0/\Delta)^2$ with varying α.

The solution for r_0 can now be used in (5.81) to transform the spatial comoving coordinate in the background coordinate R_b.

$$\frac{r^2}{\Delta^2} = \frac{F(\alpha)}{2\alpha}Z^2\,, \qquad \text{where} \qquad Z \equiv \frac{R_\mathrm{b}}{NR_H} \tag{5.88}$$

and

$$F(\alpha) \equiv (5\alpha - 2) + \sqrt{(5\alpha - 2)^2 + 24\alpha} \quad \text{if} \quad \alpha \neq 0 \tag{5.89}$$

$$\frac{F(\alpha)}{\alpha} = 3 \quad \text{if} \quad \alpha = 0 \tag{5.90}$$

The variable Z is normalised with the length scale of the perturbation and therefore it is equal to 1 at the edge of the overdensity. One can notice that the parameter Δ cancels in the expression for r/r_0 in terms of Z, and this makes it simple to interpret the physical meaning of α and Δ. In fact if we write the energy density perturbation profile as a function of Z we get

$$\tilde{e}(Z) = \Phi(\xi)\frac{\Delta^2}{2\alpha}F(\alpha)\left[1 + \left(\frac{5}{6}\alpha - 1\right)\frac{F(\alpha)}{2\alpha}Z^2 - \frac{\alpha}{2}\left(\frac{F(\alpha)}{2\alpha}\right)^2 Z^4\right] \times \\ \times \exp\left(-\frac{F(\alpha)}{4\alpha}Z^2\right) \tag{5.91}$$

and we see that the spatial profile given by the expression inside the parentheses is dependent only on α. The role of Δ, appearing only outside the brackets, is to parametrise the amplitude of the overdensity, increasing with increasing Δ. The separation of components in (5.91) is very useful from the practical point of view. It allows one to have complete control of the values of the input parameters, without a change in one of them affecting the other. For studying the curvature profiles, it is useful also to calculate the value of the second derivative of $K(r)$ at the centre, given by

$$K''(0) = \frac{\alpha - 1}{\Delta^2}, \tag{5.92}$$

and we see that when $\alpha > 1$ the value $K''(0)$ is positive and an off-centred peak appears in the profiles of both curvature and energy density. For $\alpha < 0$, instead, there is a second overdense region, corresponding to the second solution for r_0 found in (5.87). Because we are interested in solutions that represent perturbations centred at $r = 0$ and behaving like a Mexican hat, we restrict the range of shapes to $0 \leq \alpha \leq 1$.

In Figure 5.2 we have plotted corresponding curvature and energy density profiles for three different values of α between 0 and 1, taking the same value of Δ. The particular case of $\alpha = 0$ in (5.91) coincides with the Mexican hat shape used in the previous chapter during the radiation dominated epoch, where $\Phi = 2/3$:

$$\tilde{e}(Z) = \Delta^2\left[1 + \frac{3}{2}Z^2\right]\exp\left(-\frac{3}{2}Z^2\right), \tag{5.93}$$

where the parameter Δ appears with the same meaning as the quantity used there to parametrise the perturbation amplitude.

A great advantage of this description is the possibility to calculate the perturbation amplitude δ defined in (5.65), directly from the curvature profile. For a general value of α (in the radiation epoch) this gives

$$\delta = \frac{1}{3N^2}\frac{\Delta^2}{\alpha}F(\alpha)\left(1 + \frac{F(\alpha)}{4}\right)\exp\left(-\frac{F(\alpha)}{4\alpha}\right). \tag{5.94}$$

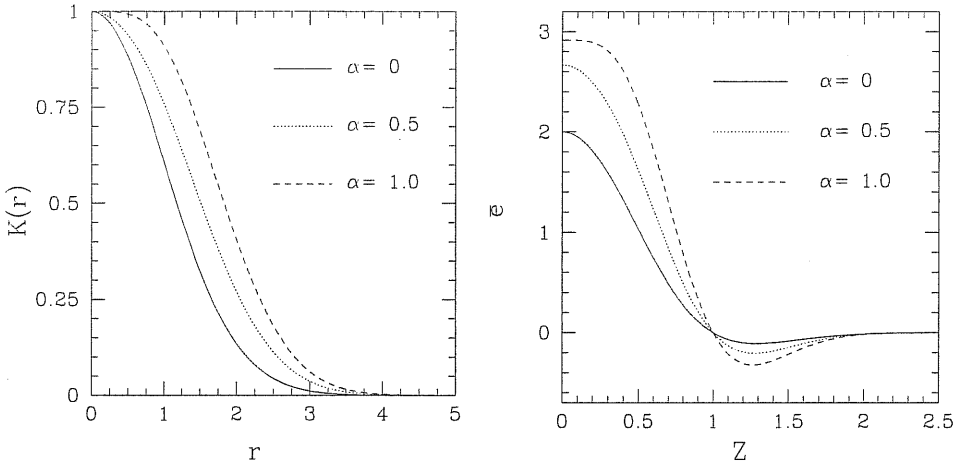

Figure 5.2: The left hand plot shows the curvature profile $K(r)$ as function of the comoving coordinate for three different value of α (0, 0.5 and 1). The right hand plot shows the corresponding profiles of energy density perturbation $\tilde{e}$ plotted as functions of Z. These cases and those described in the next figures have been calculated with $\gamma = 1/3$ (equivalent to $\Phi = 2/3$.)

Condition (5.61) should be taken into account to calculate the maximum allowed value of the perturbation amplitude for each shape. Therefore one needs to calculate the maximum value of Δ for each α and this is shown in Figure 5.3 for two different cases ($\alpha = 0$ and $\alpha = 1$). We can see clearly how an increment of Δ in the profile of $K(r)$ corresponds to an increment in the perturbation amplitude.

It is interesting to look also at the perturbation profiles of other quantities, in particular the radial velocity $\tilde{U}$ and the circumferential radius $\tilde{R}$. Together with the energy density $\tilde{e}$ these form the set of perturbations that we need to insert into the numerical code in order to specify the initial conditions. All of the other quantities instead are then calculated directly by the code using the set of Misner-Sharp equations. Rewriting the initial conditions used in Chapter 4 in terms of the tilda-quantities, expression (4.43) becomes

$$\tilde{U} \simeq \tilde{H} \simeq -\frac{1}{4}\tilde{e}. \tag{5.95}$$

A difference between this approximation and the more precise solution obtained with $K(r)$ is that the perturbation $\tilde{U}$ calculated with (5.37) is always negative if the curvature profile is always positive, while using (5.95) $\tilde{U}$ is negative in the region of the overdensity and positive in the region of the underdensity. The behaviour of $\tilde{U}$ and $\tilde{R}$ is plotted in Figure 5.4, for the same values of parameters as used in Figure 5.3.

For completeness, we show in Figure 5.5 the behaviour for the two cases $\alpha > 1$ and $\alpha < 0$. The left hand panels show the behaviour of $K(r)$ while the right hand panels show the corresponding behaviour of $\tilde{e}(r)$. The top panels show cases with $\alpha > 1$ and we can see that increasing α enhances the off centred peak creating a kind of shell perturbation with spherical symmetry. The bottom panels show the behaviours of $K(r)$ and $\tilde{e}(r)$ for $\alpha < 0$ where the curvature profile is similar to a Mexican hat. This leads to the appearance of a new overdensity region outside the central perturbation, and the energy density profile tends asymptotically to

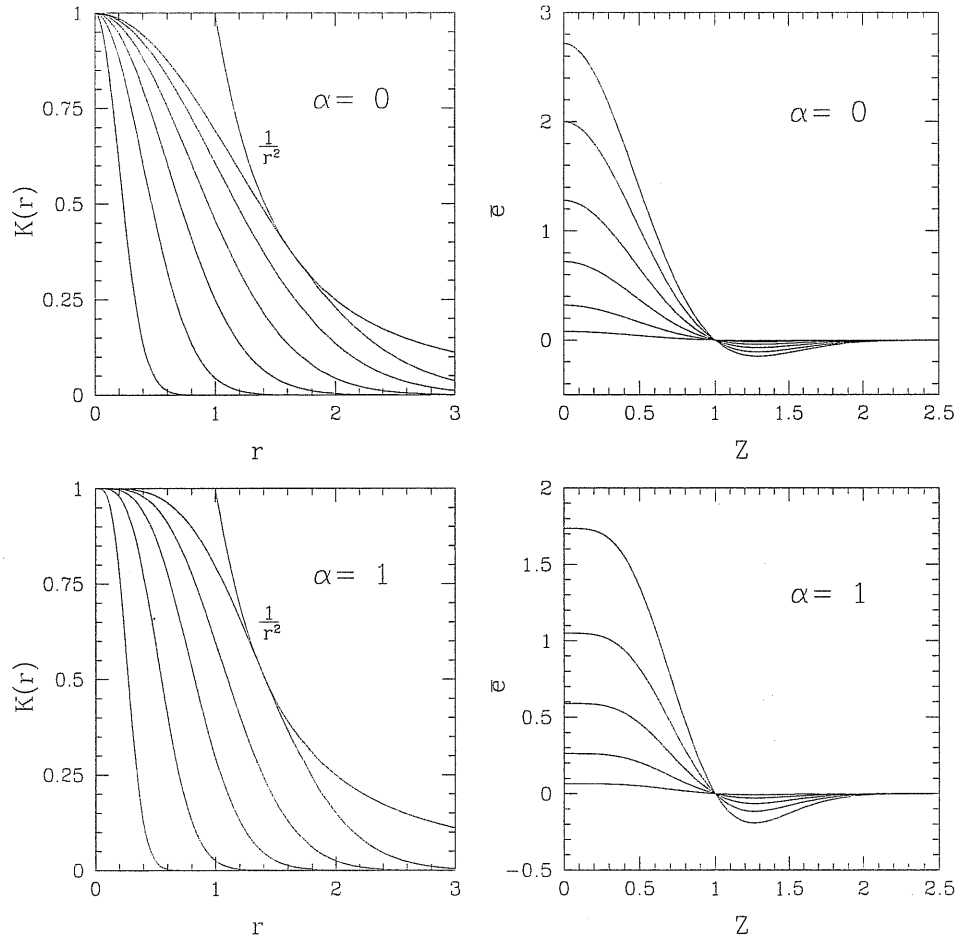

Figure 5.3: The left hand plots show the curvature profiles $K(r)$ as functions of the comoving coordinate r, while the right hand plots show the corresponding profiles for the energy density perturbation $\tilde{e}$ plotted as functions of Z. For $\alpha = 0$ (upper plots) the different profiles correspond to Δ between 0.2 and 1.1658, which is the maximum value allowed by (5.61). The values of Δ are higher for the higher curves. For $\alpha = 1$ (lower plots), the values of Δ used are between 0.15 and 0.77156.

the background from positive values, and not from negative ones as in the case of $\alpha \geq 0$. These types of profile are, of course, quite exotic and unlikely to happen, therefore we do not pay any more attention to them in the present work.

It is useful to consider also a different expression for the curvature that in some respects is similar to the one analysed until now in the range $0 \leq \alpha \leq 1$. We consider the following expression:

$$K(r) = \begin{cases} 1 & \text{if} \quad r \leq \Delta_* \\ \left(1 + \dfrac{(r-\Delta_*)^2}{2\Delta^2}\right) \exp\left(-\dfrac{(r-\Delta_*)^2}{2\Delta^2}\right) & \text{if} \quad r > \Delta_* \end{cases} \tag{5.96}$$

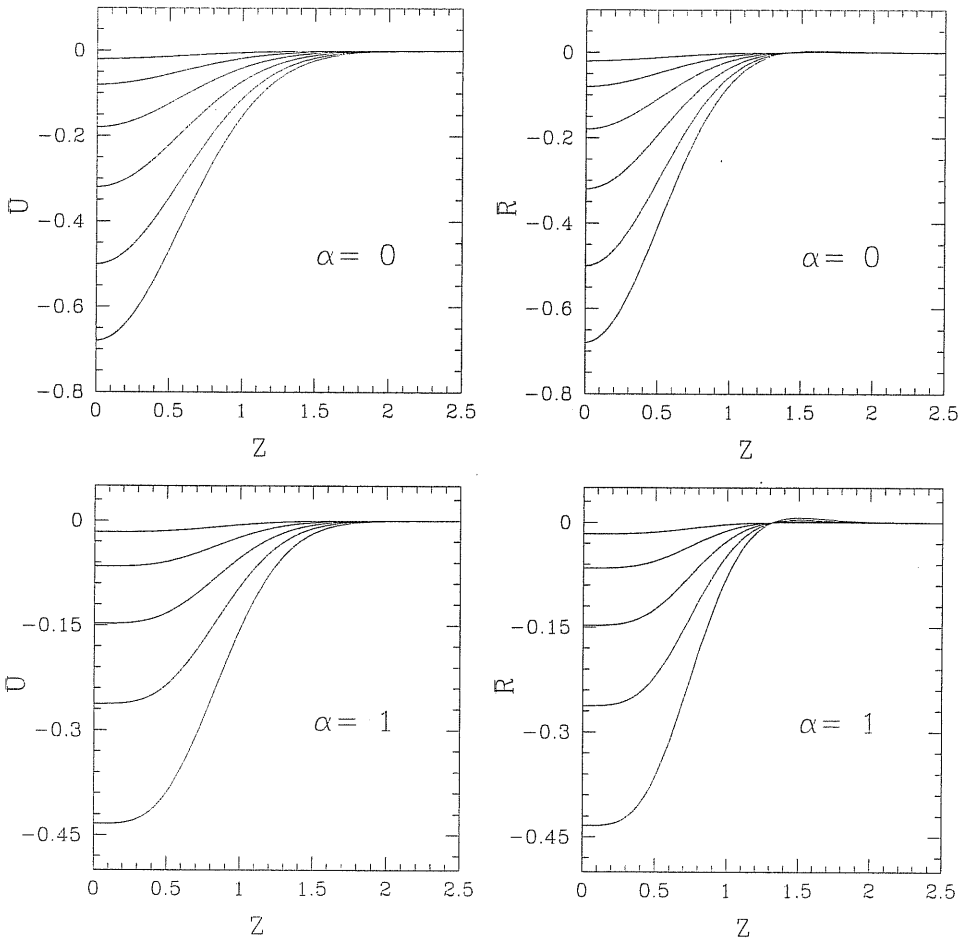

Figure 5.4: The left hand plots show the behaviour of $\tilde{U}$ corresponding to the curvature profiles of figure 5.3. The right hand plots show the corresponding behaviour of $\tilde{R}$.

where the first derivative is

$$K'(r) = \begin{cases} 0 & \text{if} \quad r \leq \Delta_* \\ -\dfrac{(r-\Delta_*)^3}{2\Delta^4} \exp\left(-\dfrac{(r-\Delta_*)^2}{2\Delta^2}\right) & \text{if} \quad r > \Delta_* \end{cases} \tag{5.97}$$

In the left panel of figure 5.6 we show the behaviour of this new parametrisation of curvature showing explicitly the two different parameters Δ and Δ_*: Δ_* specifies the length of the plateau where $K(r) = 1$, while Δ gives the sharpness of the profile that connects the plateau to 0 at infinity. In the particular case of $\Delta_* = 0$ the curvature profile coincides with case in the previous chapter. Applying the condition given by (5.64) we obtain the equation to calculate the value of r_0:

$$x_0^4 + \Delta_* x_0^3 - 3\Delta^2 x_0^2 - 6\Delta^4 = 0\,, \qquad \text{where} \qquad x_0 \equiv \frac{(r_0-\Delta_*)^2}{2\Delta^2} \tag{5.98}$$

The analytical solution for x_0 in this case is complicated and so we have used the Newton-Rapson method to find the first positive root numerically. The behaviour of r_0 as function of

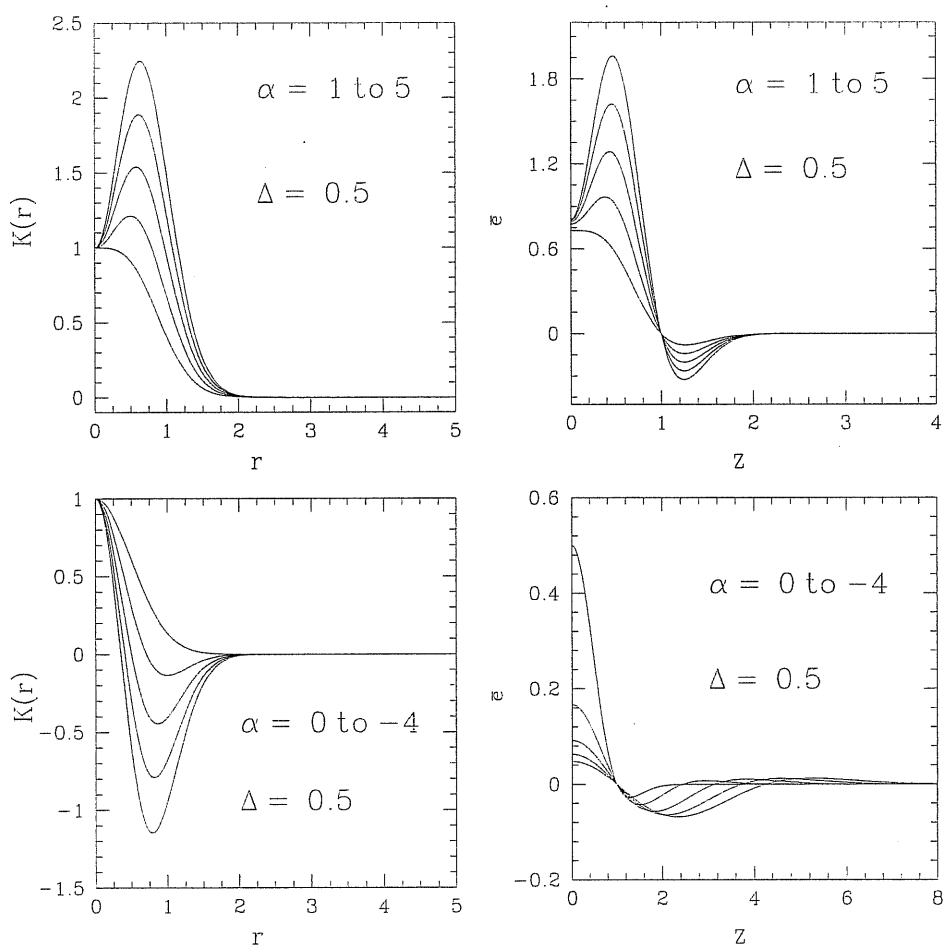

Figure 5.5: The left panel shows the behaviour of $K(r)$ for $\alpha \geq 1$ in the top row and for $\alpha \leq 0$ in the bottom row. The right panels show the corresponding behaviour of the energy density perturbation $\tilde{e}$.

Δ has been plotted in the right panel of Figure 5.6 for $\Delta_* = 0, 0.5$ and 1 and we can see that the value of Δ_* represents the lower limit for r_0 when $\Delta = 0$, corresponding to a square wave curvature profile. Increasing Δ, the value of r_0 grows roughly linearly, in a similar way as in the previous formulation for a fixed value of α. The maximum value of Δ_* acceptable for the condition (5.61) is 1 when $\Delta = 0$, with the $1/r^2$ curve touching the corner of the square wave at $K(r_0) = r_0 = 1$. The value of Δ_*, giving the length of the plateau, gives the minimum value of the perturbation amplitude δ, corresponding to $\Delta = 0$. The value of Δ is then specifying the sharpness of the perturbation similarly to α in the previous case.

In Figure 5.7 we show in the left top panel, how the profile of $K(r)$ is changing when Δ_* is constant and Δ is varying up until the limit given by (5.61), while in the left bottom panel we show the simulation when Δ is constant and Δ_* is changing. In the right panels we show the corresponding behaviours of $\tilde{e}(r)$.

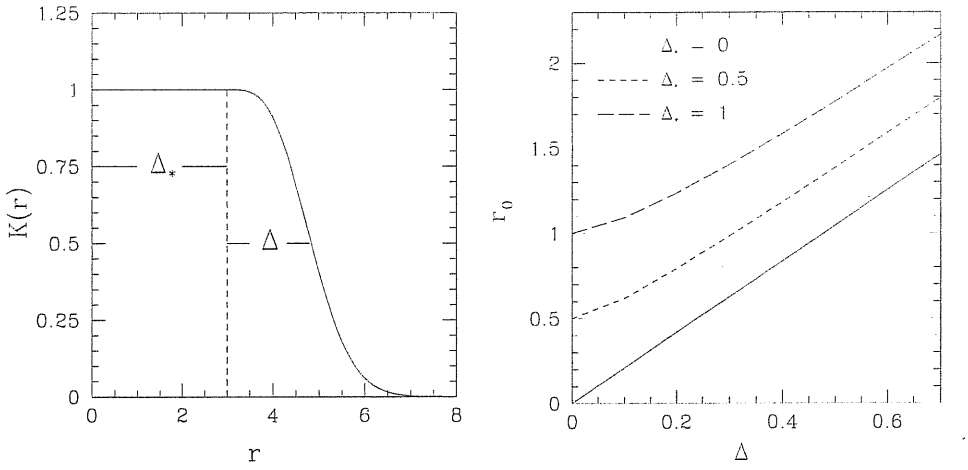

Figure 5.6: The left panel shows the general behaviour of $K(r)$ given by (5.96), indicating explicitly the meaning of the two parameters Δ and Δ_*. The right panel shows the value of r_0 with varying Δ, for three fixed values of Δ_*.

5.3.2 Numerical tests

Now we discuss the numerical tests that we have made in order to be confident that the perturbation profile $K(r)$ has been introduced consistently into the code. We need to study the approximation of imposing a perturbation with a length scale much larger then the horizon length, in order to determine when ϵ is small enough to make higher order terms negligible. One test is to use equation (5.29) to re-derive $K(r)$ after calculating the initial conditions for the various quantities. This expression is valid when the higher order terms are negligible, therefore we expect to find some difference between the profile of $K(r)$ calculated with (5.29) and the original ones used to build the initial conditions. In Figure 5.8 and in the left panel of Figure 5.9 we plot the result of this test using both expressions for $K(r)$ with $\alpha = 0$, $\alpha = 1$ and $\Delta_* = 0.5$. In both cases we use a value of Δ very close to the maximum, corresponding to $K(r)r^2 = 1$, in order to make the test harder. The solid lines are the analytical profiles of $K(r)$, while the dashed lines correspond to the derived profiles of $K(r)$ with different values of N. The first value used was $N = 1$, that we know is not large enough as is also clear from the picture, and we then increase N progressively. We can appreciate the progressive approach to the analytical solution obtained in this way, where the most precise case shown in the plots corresponds to $N = 10$. The centre of the perturbation is the region where there is the largest difference because it corresponds to the part of the perturbation that is initially inside the horizon. It is therefore useful to quantify precisely the error in the centre of the perturbation and study how it varies with respect to N. (The difference between the values of the integrated δ will give a weaker estimate than this because their calculation takes into account also regions outside the horizon where the convergence is easier, as one can see from Figure 5.8 and Figure 5.9.)

In the right panel of Figure 5.9 the difference between the central values of the analytical and numerical solutions for $K(r)$ is plotted as a function of N. The white and black triangles differ

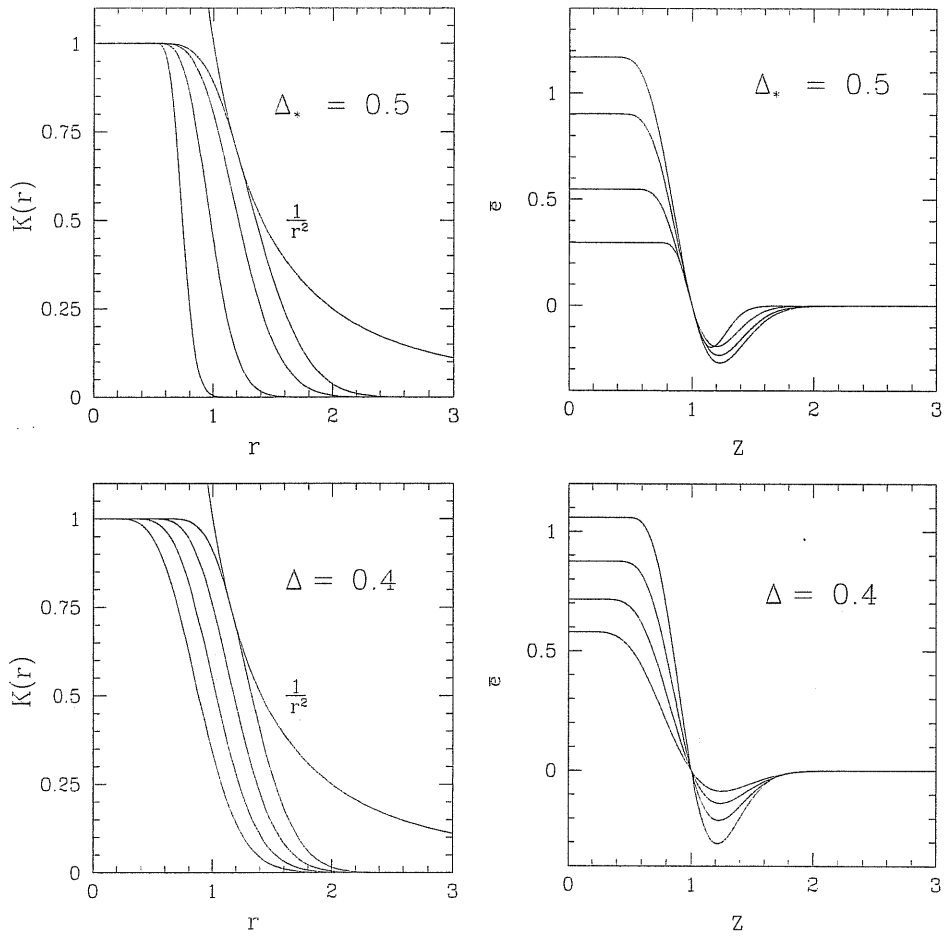

Figure 5.7: The left panels show the curvature profile $K(r)$ for Δ_* constant and varying Δ in the the top row and for Δ constant and varying Δ_* in the bottom row. The corresponding behaviour of the energy density perturbation $\tilde{e}$ is plotted in the right panels.

in the value of α, while the black dots refer to $\Delta_* = 0.5$, and we can see clearly that the error is behaving like $\epsilon = 1/N^2$, represented by the dotted curve, with a slight difference between the different cases considered. This test is consistent with the scheme of the perturbative analysis that considers higher order terms behaving like ϵ^2.

To be completely sure of the accuracy, we have done also one more test for the same $K(r)$, comparing the evolutions of a perturbation obtained with the same curvature profiles but using different initial values of N, and in Figure 5.10 we show the value of δ calculated during the evolution and plotted against $1/N$. It can be seen that there is no significant difference between initial values of $N = 10$ and $N = 20$, we therefore feel confident in using an initial value of $N = 10$ to build the initial conditions with $K(r)$ given by (5.83), corresponding to an error of $\sim 1\%$ in the inner region. The test for $\alpha = 1$ corresponds also to the second formulation with $\Delta = 0$ and in this case too $N = 10$ is a satisfactory choice.

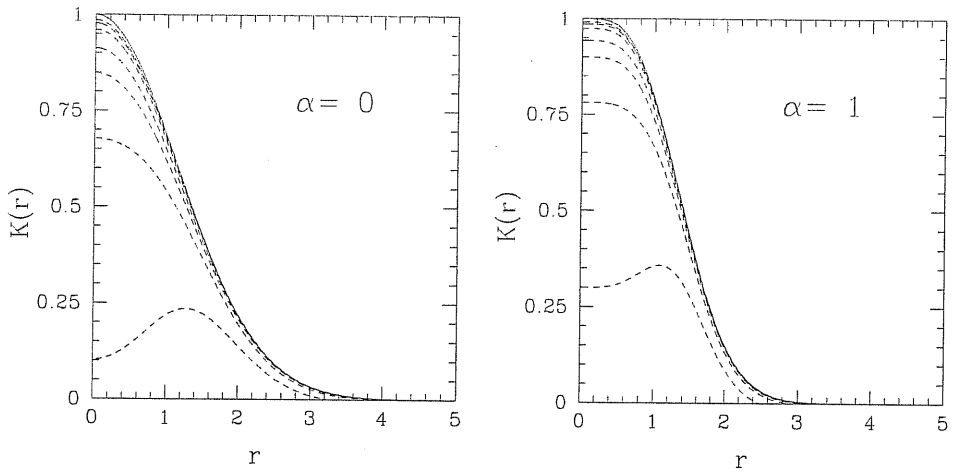

Figure 5.8: These plots show the comparison between the analytical (solid line) and the numerical (dashed lines) profiles of curvature given by (5.83). The different dashed lines correspond to $N = 1, 2, 3, 4, 6, 8, 10$ with the higher curves corresponding to the higher values of N. The profiles in the left hand plot are characterised by ($\alpha = 0$, $\Delta = 1.15$), and the profiles in the right hand plot by ($\alpha = 1$, $\Delta = 0.77$).

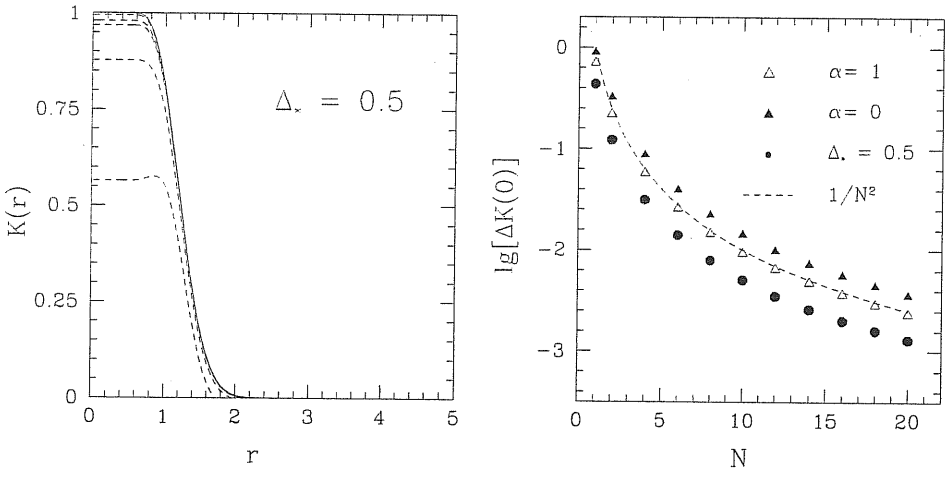

Figure 5.9: In the left panel we show the comparison between the analytical (solid line) and the numerical (dashed lines) profiles of curvature given by (5.96). The different dashed lines correspond to $N = 1, 2, 4, 5, 7, 10$ with the higher curves corresponding to the higher values of N. In the right panel we show the difference between the central value of the analytical and numerical profiles of $K(r)$ in Figure 5.8 and in the left panel, plotted as a function of N.

5.4 Description of the numerical calculations

Calculations of black hole formation with these new initial conditions are for the most part very similar to those presented in the previous chapter. Therefore we show just a sample case in Figure 5.11, remembering that when using the observer-time slicing, black hole formation occurs when the lapse $f \to 0$ and $\Gamma + U \to 0$ together, (see equation (4.26)). The left hand plot shows the behaviour of $2M/R$ and we see the asymptotic approach to 1 of the maximum

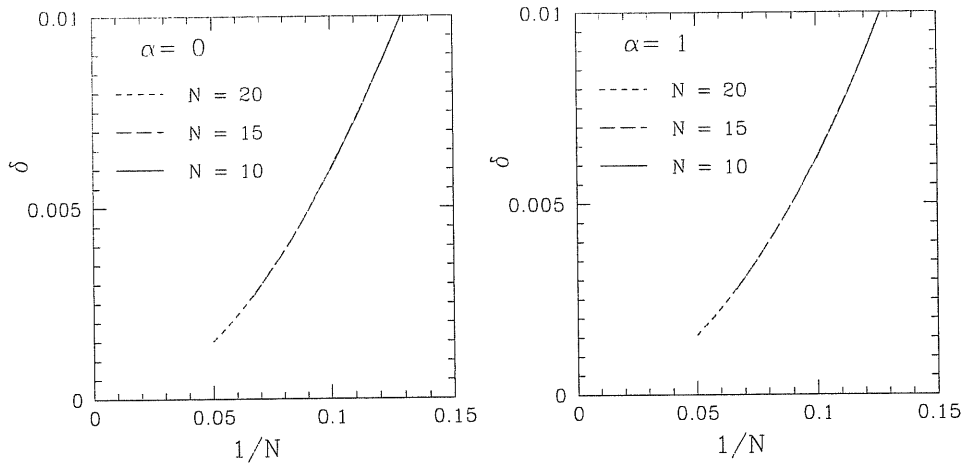

Figure 5.10: These plots show three time evolutions of δ calculated with the same profiles of $K(r)$ studied in figure 5.8 and 5.9; the three evolutions have different initial values of N.

of this curve, that determines the exact location on the grid at which the apparent horizon is forming. The right hand plot shows the corresponding behaviour of the mass, as a function of R, giving value of the mass of the hole. In figure 5.11 the circumferential radius R and mass M have been normalised with respect to the values for the horizon scale at the horizon crossing time.

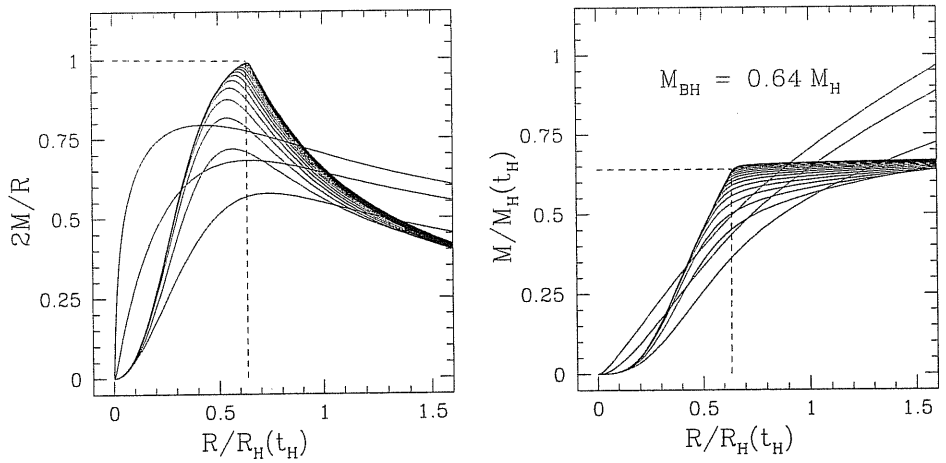

Figure 5.11: A typical evolution leading to black hole formation: the initial curvature profile used is characterised by $\alpha = 0$ and $\Delta = 1.02$, which give $(\tilde{\delta} - \tilde{\delta}_c) = 1.3 \times 10^{-2}$. The left-hand panel shows the profile of $2M/R$ at different times with the approach to 1 of the maximum value; the right-hand panel shows the corresponding evolution of the mass.

The only significant difference with respect to the earlier calculations is that we have not seen any appearance of shock behaviour during the formation of black holes, for any of the profiles used so far. In Chapter 4 we were observing the formation of shocks when the amplitude of the perturbation was very close to the threshold δ_c for black hole formation ($(\delta - \delta_c) \lesssim 10^{-4}$).

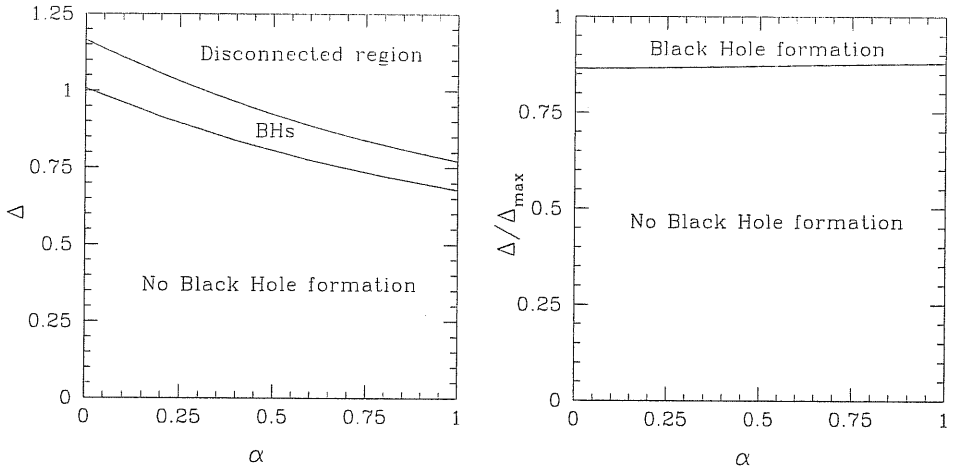

Figure 5.12: These plots show which values of α and Δ lead to black hole formation or, in the left panel, to an initial perturbation already disconnected from the rest of the Universe.

As we said earlier, the initial conditions with $\alpha = 0$ give the same Mexican hat shape of perturbation used in the previous calculations, and so it is plausible to think that the shock behaviour was caused by a small residual decaying mode component which was still present in the previous calculations but is avoided in the present ones.

It is useful to introduce at this stage a measure of δ independent of the initial scale used to impose the initial conditions, in other words independent of the particular value of N used. Looking at expression (5.65), we can see that in the case of constant γ, if we define $\tilde{\delta} \equiv N^2\delta$, the expression becomes time independent, giving in the radiation epoch

$$\tilde{\delta} = \frac{2}{3}K(r_0)r_0^2 . \tag{5.99}$$

Comparing this value with the value of δ at horizon crossing, we find that it is of the same order (with a small correction due to the non linear growth near to the horizon crossing). We therefore use $\tilde{\delta}$ to characterise the amplitude of a perturbation for the rest of the discussion.

The most important result of this calculation is in establishing the parameter ranges giving black hole formation. Using the first curvature formulation, what we did in practice was to fix successive particular values of α and find the corresponding threshold values of Δ. In Figure 5.12 we see a synthesis of these calculations. The left hand panel shows the results obtained for each value of Δ and α used in parametrisation (5.83), and this divides the plane into three different regions: the first corresponding to no black hole formation, the second to black hole formation and the third to a disconnected initial perturbation ($K(r)r^2 \geq 1$). The right hand panel shows the same results but with Δ normalised with respect to the maximum value $\Delta_{\max}$, corresponding to the boundary of the third region of the plane. In both ways of presenting this, we see that the range of parameters leading to black-hole formation is narrow with respect the range of no black hole formation, and this shows that black hole formation is difficult to achieve, needing an amplitude of the perturbation near to the maximum value.

The same results are shown also plotting $\tilde{\delta}$ with respect to α in Figure 5.13. This shows

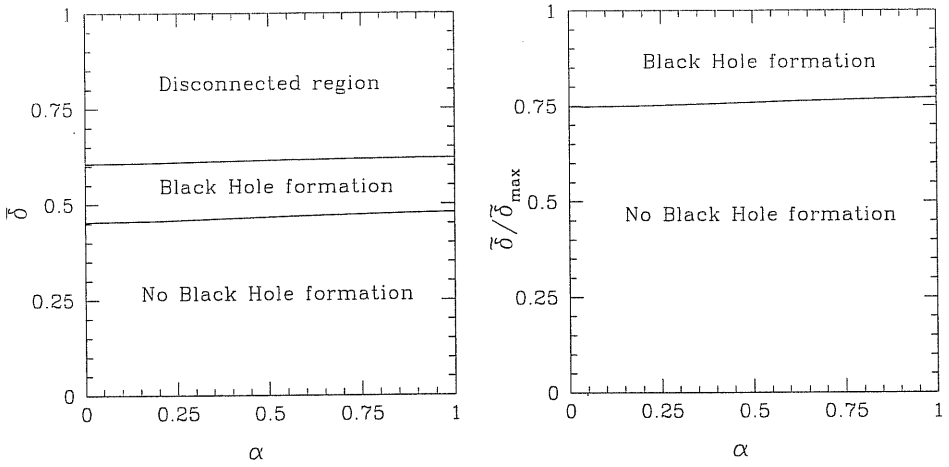

Figure 5.13: These plots show how $\tilde{\delta}_c$, the threshold amplitude for black hole formation, varies with α. The left panel also shows when the value of $\tilde{\delta}$ is able to disconnect the perturbation from the rest of the Universe.

an interesting feature that is the small change in $\tilde{\delta}_c$ and $\tilde{\delta}_{\max}$ when the shape of perturbation changes with changing α. We have found $\tilde{\delta}_c \simeq 0.45$ and $\tilde{\delta}_{\max} \simeq 0.60$ for $\alpha = 0$ and $\tilde{\delta}_c \simeq 0.47$ and $\tilde{\delta}_{\max} \simeq 0.62$ for $\alpha = 1$. This is consistent with figure 5.12, where the increasing of α is balanced by the decreasing of the threshold value of Δ, making the final values of $\tilde{\delta}_c$ and $\tilde{\delta}_{\max}$ almost unchanged. The value of $\tilde{\delta}_c$ found is consistent with the result of Chapter 4, where we found $\delta_c \simeq 0.43$ at horizon crossing for a Mexican-hat profile. The slight difference occurs just because of the difference between $\tilde{\delta}_c$ and δ_c calculated at the horizon crossing time.

We can see this behaviour looking also at figure 5.14 where the variation of the curvature and energy density profiles for the different threshold solutions is plotted. For the curvature we see that there is a region where the values of $K(r)$ for different values of α are nearly the same and this corresponds, in fact, to the location of r_0. The energy density profile shows that the difference is just in the shape of the central part, with almost the same profile for $Z \gtrsim 0.5$.

We can then conclude that the variations in the parametrisation of curvature given by (5.83) have not played a large role in the determination of the threshold amplitude $\tilde{\delta}_c$ for black hole formation. However, it is not clear from this that $\tilde{\delta}_c$ is in general not strongly dependent on perturbation shape; we need to compare the results obtained with other different expressions for $K(r)$ in order to really understand how strongly the threshold for black hole formation is dependent on the initial perturbation shape.

In Figure 5.15 we show the parameter space for the second curvature parametrisation given by (5.96). In the left panel we show the parameter space for Δ and Δ_*, and we see the three different regions of no black hole, black hole formation and disconnected perturbation seen also in Figure 5.12. In the right panel we plot the same results using the parameters Δ_* and $\tilde{\delta}$ calculated with (5.99), and in this case we have a region of parameters that is mathematically forbidden from the definition (5.99). The reason is due to the minimum value of r_0 given by Δ_* (see right panel of figure 5.6), and the curve that corresponds to the boundary of the

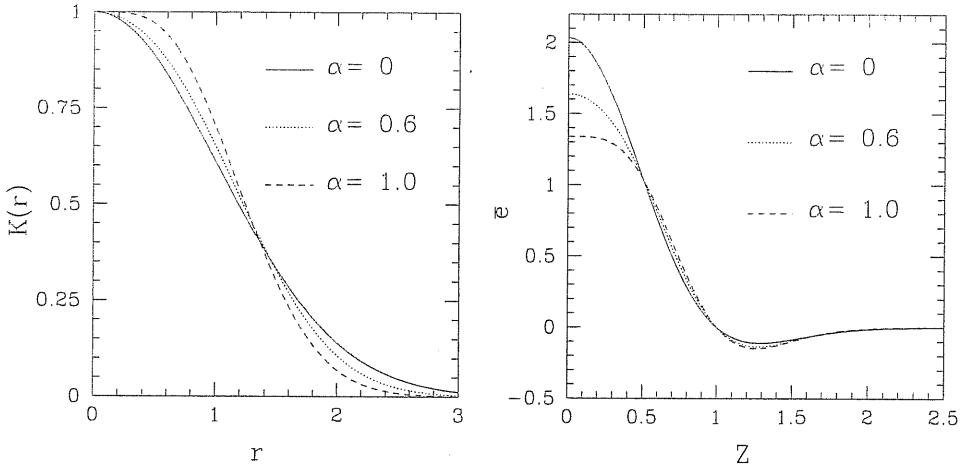

Figure 5.14: These plots show the curvature and energy density profiles corresponding to the threshold solutions for black hole formation, where the different lines correspond to different values of α.

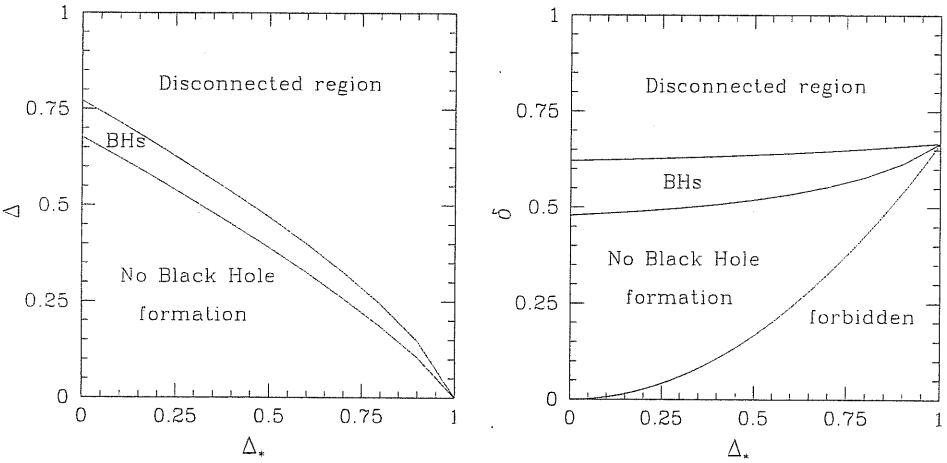

Figure 5.15: These plots show the range of parameters Δ, Δ_*, δ referred to $K(r)$ given by (5.96) that gives origin to black hole formation.

forbidden region is given by $\tilde{\delta} = 2/3\,\Delta_*^2$. Equation (5.99) also shows that the maximum value of the "disconnected region condition" is when $K(r_0)r_0^2 = 1$, and this is exactly the value corresponding to the edge of the right plot where $\Delta_* = 1$. The curve given by $\tilde{\delta} = 2/3\,\Delta_*^2$ corresponds to square-wave perturbations. In general we can see that, when the profile is very sharp (corresponding to Δ being small), the formation of black holes is more difficult, until the limit of square-wave perturbations that never give black hole formation.

It is clear that the choice of perturbation shape significantly affects the results as regards the possibility for having black hole formation and should be made on the basis of physical considerations. The idea of connecting the curvature parametrisation to the power spectrum coming from inflation is likely to be the right way to proceed. Another important aspect is that we have observed no formation of shocks during black hole formation, for all of the range of

parameters that we have explored. We suspect that this is a general feature for PBH formation from purely growing mode initial conditions, and that the strong shock formation observed in the past [42] was connected with the presence of a non-linear decaying mode component in the initial conditions. Analysing this aspect in connection with other features of critical collapse is the subject of the next chapter.

Chapter 6

PBHs and critical collapse

This final chapter is dedicated to the particular feature of critical collapse in the context of PBHs. The discussion is divided in two sections, the first one gives a review of the previous work of Hawke & Stewart [42], the second presents the numerical simulations that we have performed with an improved numerical scheme, discussing the nature of the critical solutions with our simulations and presenting a sequence of different scaling laws obtained using different numerical resolutions. Our results suggest a different possibility from that proposed by Hawke & Stewart.

This work is very challenging from the numerical point of view, and to get the results presented here we have improved the numerical scheme by inclusion of adaptive mesh refinement. The numerics play a key role in this work and we want to be prudent in saying that what we have observed seems to indicate a different result from but from before, to be more certain, it is necessary to have a more extended analysis. This discussion is located at the end of this thesis because the new formulation for imposing initial conditions, developed in the previous chapter, is crucial for it.

6.1 The problem of a minimum mass in the PBH mass spectrum

As we have seen in Chapter 4, the formation of PBHs is characterised by a scaling law behaviour given by (4.46) when the amplitude δ of the perturbation is quite close to the critical threshold δ_c. This behaviour, if conserved all the way down to δ_c, allows production of very small PBHs during all of the the early Universe, and the standard picture of the PBH masses being given roughly by the horizon scale at the time of formation should be dropped. If this is really the case, it would make an important difference from the standard scenario, because small PBHs able to evaporate within the timescale of the Universe will be produced also later and the mass spectrum of PBHs will change considerably. Therefore the question about the range of applicability of a scaling law within the scenario for PBHs is an important problem that needs to be clarified.

As we have seen in Chapter 4, in agreement with what has been obtained by Niemeyer &

Jedamzik , the scaling law behaviour is appearing at least in the mass range $M_{\rm BH} = (0.1 - 1)M_H$. For smaller masses the initial conditions used there were giving rise to strong shocks that created a problem for the numerical scheme. This issue has been deeply investigated by Hawke & Stewart [42] with a specially built code implemented with a modern high-resolution shock capturing scheme, written in an Eulerian frame. Within their scheme they needed to consider, as initial conditions, density profiles well within the horizon. Their results are summarised in Figure 6.1, where, for black holes with $M_{\rm BH}/M_H \geq 10^{-3}$, they have the numerical evidence of scaling as described by (4.46), with a value of the $\gamma \simeq 0.36$, consistent with what was observed previously. However, for smaller black holes the scaling breaks and there is a minimum black hole mass $M_{\rm BH} \simeq 10^{-3.5} M_H$. The parameter C used here is the initial amplitude of the pressure perturbation with C_* being the critical value for black hole formation. The values for $log(C - C_*)$ are very similar to ones for $log(\delta - \delta_c)$, differing just by a small additive constant which depends on the shape of the perturbation. The value of M_H used here is that at the initial time of the Hawke and Stewart calculations and not at the horizon crossing time as in our work. The horizon mass varies roughly as $M_H \propto (R_0/R_H)^{-2}$, where (R_0/R_H) is the radius of the initial overdensity in units of the initial horizon scale. While precise details of the initial conditions are not given in the Hawke and Stewart paper, their minimum mass probably corresponds to about $10^{-2} M_H$ in our units.

In their simulations they saw the combination of two different effects: the initial collapse of

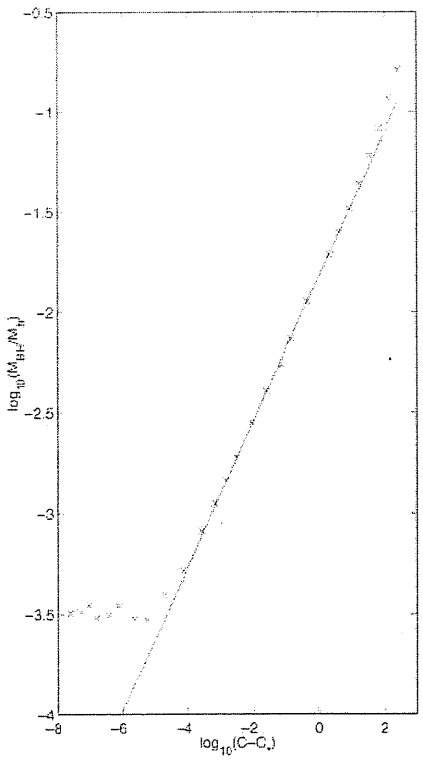

Figure 6.1: Results obtained by Hawke & Stewart [42] for black hole mass as a function of the parameter C using an initially Gaussian perturbation profile.

the overdensity and an initial outward motion leaving behind a deepening void and eventually fronted by a shock wave in nearly critical cases which then reflects back off the surrounding medium. The shock produces a nonlinear perturbation of an otherwise roughly self similar solution for the collapsing matter, that at a certain mass scale is able to break the self-similarity. For their initial data they have seen that black holes with masses $\geq 10^{-3}\, M_H$ form before the perturbations caused by the shocks can affect the solution (studied by Evans-Coleman in the radiation fluid [84]), while for smaller black hole masses the shocks perturb this solution, breaking the scaling law. They consider this perturbation of the self similarity as a kink mode that, as shown by Harada, arises in spherically symmetric self-similar solutions when there is the formation of high pressure gradients [85].

Following our earlier discussion here, we wanted to pay close attention to the initial conditions used because, as we have seen, they can strongly affect the final result of the simulations. We have noticed in the simulations of the previous chapter that imposing initial conditions that describe a perfectly pure growing mode, we do not observe the shocks that we were observing before in Chapter 4, where the growing mode solution was described with less precision. It can seem surprising that an imprecision, that in the growing solution for the amplitude of δe was giving an error of a few percent (see Figure 4.7) can be responsible for the appearance of shocks when the evolution becomes non linear. However we have to take into account that the linear theory of perturbations is described by the Fourier components of the perturbed quantities. A small deviation of the initial solution with respect to the pure growing mode amplitude measured in the space-time is transformed in the Fourier space into a non-linear component that, after horizon crossing, when the region becomes causally connected, can give rise to significant hydrodynamical effects. Hawke and Stewart have considered initial conditions well within the horizon and did not perturb the velocity field. Cases where a black hole is formed then correspond to strongly non linear initial perturbations with a serious decaying mode component.

6.2 Description of the numerical calculations

To proceed with our analysis and investigate black hole masses smaller that $10^{-1} M_H$ we needed to modify the code, giving the numerical resolution necessary to treat the regions of strong rarefaction and compression that we have with these simulations. In fact the form of the gridding introduced in Chapter 4 was satisfactory for cases where δ was not extremely close to δ_c but for cases extremely close to critical, problems arise because of the appearance of regions with extremely low density in which the co-moving Lagrangian grid becomes severely overstretched giving poor spatial resolution. An obvious remedy for this is to introduce adaptive gridding, with additional zones being added wherever necessary to improve resolution.

6.2.1 The adaptive grid

We have implemented a form of adaptive gridding using a fully-threaded-tree algorithm. It is still in the process of being further developed but is already working well and giving greatly

improved results for nearly-critical cases. We give just a brief overview here of the methodology used.

Every 100 time-steps, a check is carried out to see whether the fractional zone spacing $\Delta R/R$ is greater than 9% for any zone. If it is, that zone is sub-divided introducing a new grid-point at its centre (in terms of the co-moving radial coordinate μ) and quantities at the new grid-point and in the two newly-created zones to either side of it are calculated by means of linear interpolation. Only one zone is sub-divided at a time, allowing the solution to relax before performing any subsequent sub-division. Doing this, we have not found it necessary to introduce any additional diffusion into the code for suppressing numerical noise, an important point for interpreting the appearance or absence of shocks. Also every 100 time steps (but offset by 50 timesteps), we carry out a check to see whether $\Delta R/R$ has become less than 4% across any zone resulting from a previous subdivision. If so, then it is merged with the zone from which it was previously separated if that zone has the same $\Delta\mu$. Again linear interpolation is used and only one merging is carried out at a time to allow relaxation. A key feature of the fully-threaded-tree algorithm is to retain the possibility of reversing the sub-division history when previously sub-divided zones become narrower than necessary. For doing this, history arrays are introduced keeping a record of the number of sub-divisions of each zone and of the identity of the zone from which it was separated at each stage.

Testing this algorithm we have realised that it is convenient to apply the merging zone conditions also in regions that have never been subdivided. This because we use a simple exponential grid in order to have a satisfactory resolution in the innermost region were the collapse would occur, but in doing so we tend to have too many grid points at certain times of the hydrodynamics, when the outermost region will be strongly compressed. We have therefore allowed the code to merge zones outside the collapsing region, applying the same algorithm explained above. After some experimentation we have been able to make this scheme work efficiently.

A further development that can be interesting to investigate is to replace the linear interpolation with a piecewise cubic interpolation, however it is not clear whether this would give a significantly more stable and precise solution than the one obtained with simple linear interpolation.

6.2.2 The behaviour of the critical solution

As seen in Chapter 4, an efficient way to understand whether a solution is going to give black hole formation is to look, for example, at the behaviour of the ratio $2M/R$ and see if the maxima of these curves, after the collapse in the centre has occurred, is increasing to 1 or is decreasing to zero. The increasing behaviour, which is giving rise to black hole formation, has been discussed previously in Chapter 4, and is shown in the top left panel of Figure 6.3. The decreasing behaviour, shown in the top right panel of figure 6.3, is instead corresponding to the subcritical solution.

The critical solution is represented by the balance between these two cases and is shown in the bottom panel of figure 6.3; note how the relative maximum of the different curves is

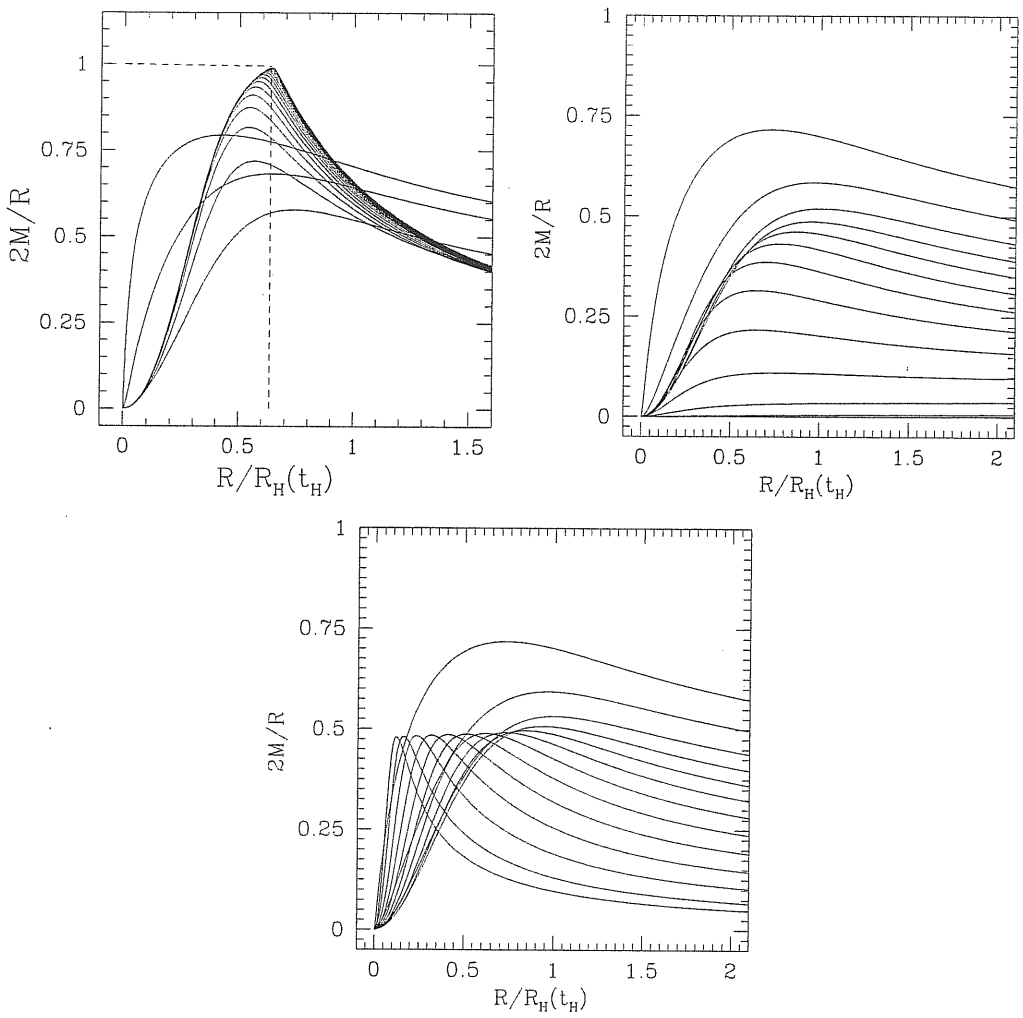

Figure 6.2: These three plots show the behaviour of the ratio $2M/R$. The top left panel is for the supercritical case corresponding to $\delta > \delta_c$; the top right panel is for the subcritical case corresponding to $\delta < \delta_c$, and the bottom panel is the critical solution with $\delta = \delta_c$. The time ordering of the curves goes from top to bottom on the right hand side.

moving with a constant value $\simeq 0.48$ towards the centre. This solution represents a clear dividing line between the collapses that lead to black hole formation and those that are then dispersed again into the background. The equilibrium of the peak is clearly understandable as a perfect balance between the gravitational potential of the fluid and the internal pressure support. We can observe, in fact, that the points corresponding to the maxima of the curves of this critical solution is coincide with the edge of the collapsing region ($U = 0$). Instead in the supercritical solution, the value of U is negative at that gridpoint, while in the subcritical solution the corresponding value of U is positive.

The critical solution for the collapsing region should be characterised by a self similar behaviour and so it should be possible to find an appropriate renormalisation of the curves at every time step, giving an effectively time independent solution. Plotting the profiles at each

time with respect to $R/R_{\max}$, where $R_{\max}$ is the location at each time of the maximum of the curves, we have verified this property in the collapsing region. This is a proof of the self similar behaviour, and therefore of the critical nature, of the collapsing solutions with $\delta = \delta_c$.

6.2.3 The scaling behaviour with different resolution

With the adaptive grid described above we have been able to get a satisfactory resolution for studying black hole formation with $(\delta - \delta_c)$ down to 10^{-7}, decreasing the previous limit obtained in Chapter 4 by three orders of magnitude. We are still not observing any shock formation, although the behaviour of the fluid outside the collapsing region is becoming more and more extreme as $(\delta - \delta_c)$ is decreased. As we can see from Figure 6.3 at late times we have a rapid expansion just outside the black hole producing a very rarefied region there. Getting closer and closer to δ_c, this hydrodynamical process becomes more extreme and we can appreciate the efficiency of our adaptive scheme that is now able to resolve hydrodynamical behaviours that we could not follow before.

In Figure 6.4 we have plotted our results for the scaling law obtained with $(\delta - \delta_c)$ going down to 10^{-7} (almost the same scale investigated by Hawke & Stewart as shown in Figure 6.1). The three curves correspond to the same type of initial Mexican-hat perturbation profile studied with three different initial resolutions of the grid-spacing, (with central values of $\Delta\mu = (2.5, 2.8, 3.5) \cdot 10^{-2}$ in our units, corresponding respectively to $630, 777, 864$ zones). This is a change of grid spacing at the initial time that is not related to the subsequent adaptive mesh refinement. The figure shows that the scaling law behaviour is broken at a certain point, levelling off the values to a minimum mass. Now, however, the reason for this behaviour, which looks rather similar to that obtained by Hawke & Stewart, is different. Here the value of the minimum mass depends on the initial resolution used to characterised the innermost region of

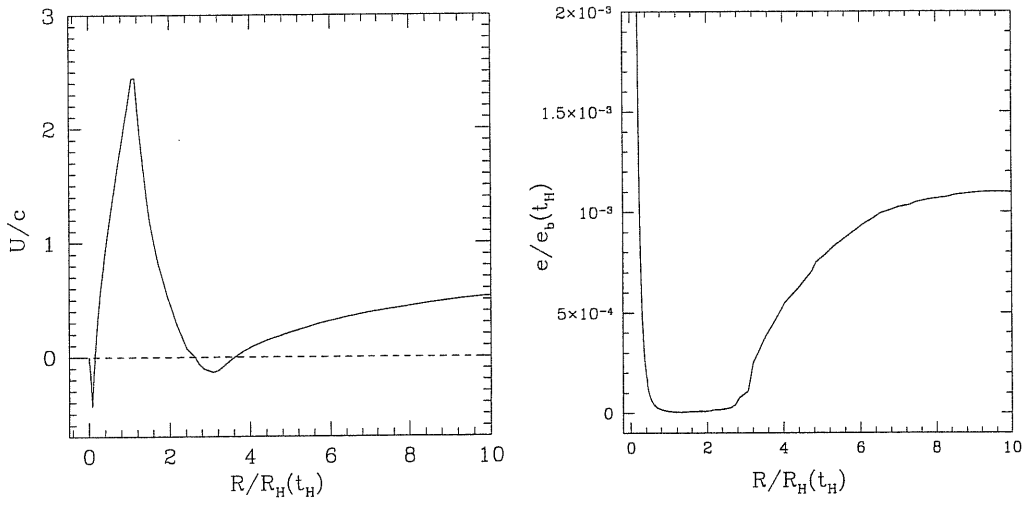

Figure 6.3: These two plots show the behaviour of velocity U/c and energy density $e/e_b(t_H)$ plotted against $R/R_H(t_H)$ at a late time in a collapse with $(\delta - \delta_c) = 10^{-6}$. In the left panel we can appreciate the quite extreme behaviour of velocity within the very underdense region see in the right panel.

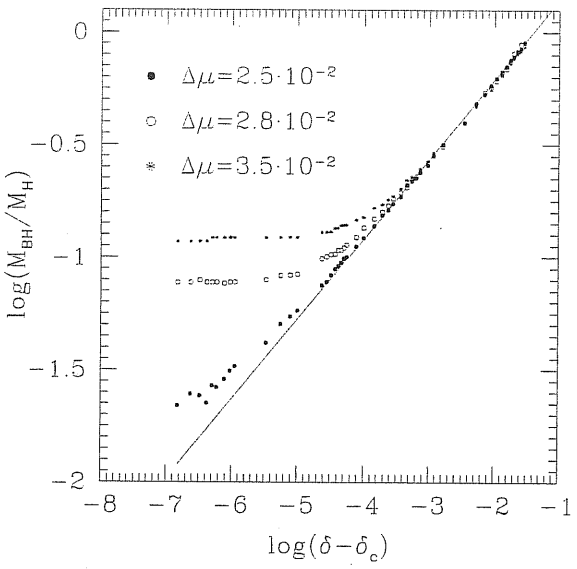

Figure 6.4: The plot shows results obtained with different resolutions of the initial grid-spacing, expressed in our notation by $\Delta\mu$, with the same type of initial Mexican-hat perturbation. The solid line represents the analytic fit for a scaling law behaviour with exponent $\gamma = 0.355$.

the grid and the effect is clearly due to discretization error depending on the initial resolution. For the finest resolution, the results stay close to the scaling law down to extremely low masses but with some deviation which remains to be examined further after some more refinements have been made to the code.

In conclusion we do not observe any shocks, and the scaling law behaviour is preserved down to values of $(\delta - \delta_c)$ which are comparable with those used by Hawke & Stewart. The fact that the scale of the masses is different is probably due to the different normalisation, although we have not yet been able to check this precisely. This seems to indicate that the scaling behaviour may be preserved and that, with sufficient resolution, it may be possible to get smaller and smaller PBHs. Of course we do not know yet whether some change could eventually arise, changing the solution, and it is true that numerically we will never be sure that there might not be a change at some point. However, the fact the we do see the shocks, that Hawke and Stewart were observing (and that they interpreted as being responsible for the breaking of the scaling law) seems to be an indication that the continued scaling behaviour may be a genuine characteristic of the PBH formation scenario if the initial conditions are represented by pure growing modes.

This is work in progress and we are currently investigating further improvements to the code in order to make this discussion more solid.

Conclusions

This thesis has analysed the possibilities for PBH formation in the early universe, focusing on the radiation-dominated era. In the first part (Chapters 1 - 3) we have given a review of the background to the subject. Chapter 1 was dedicated to describing the properties of the unperturbed cosmological background and in Chapter 2 we have then described the origin, properties and evolution of cosmological perturbations in modern inflationary theory. Then, in Chapter 3, we have specifically reviewed the literature on PBHs, discussing in some detail the aspects that play an important role for the original contributions of this thesis, presented in Chapters 4 - 6.

In Chapter 4, we have introduced the hydrodynamical scheme used for our calculations, discussing all of the equations used to write the computer codes. We then presented results from numerical simulations performed with these codes. Growing-mode perturbations were specified within the linear regime and their subsequent evolution was then followed as they become nonlinear both in the case of super-critical perturbations, which go on to produce black holes, and of sub-critical perturbations, for which the overdensity eventually disperses into the background medium. For super-critical perturbations, we revisited the results of previous work concerning scaling-laws, noting that the threshold amplitude for a perturbation to lead to black-hole formation is substantially reduced when the initial conditions are taken to represent purely growing modes. For sub-critical cases, where an initial collapse is followed by a subsequent re-expansion, strong compressions and rarefactions are seen for perturbation amplitudes near to the threshold.

The method used for specifying growing-mode perturbations which we used in that work remained rather approximate, however, and was not completely satisfactory for making a proper link with the cosmological spectrum of perturbations coming from inflation. In Chapter 5, we presented a more sophisticated reformulation of the problem, introducing a new prescription for setting up initial conditions, using time-independent curvature perturbations that can be defined in a gauge-invariant way.

Finally, in Chapter 6, we have focused attention again on critical collapse and the related scaling-law behaviour. Introducing adaptive mesh refinement into our code allowed us to investigate PBH formation nearer to the critical limit and to re-examine the suggestions by Hawke & Stewart about the scaling law behaviour being broken near to the critical limit, giving rise to a minimum mass for PBHs formed at any given epoch. With our formulation of the initial conditions, we have not seen evidence for the formation of strong shocks in connection with PBH formation which was a key feature of their work and we tentatively suggest that the

scaling laws may continue down to very small masses, in contrast with the previous results. This is work still in progress, however.

For future work we have a detailed plan of aspects that we think that it would be very interesting to analyse. Starting from the description of the initial conditions with the curvature perturbation, we intend then to make a further step to determine the probability associated with different shapes of perturbation, which means connecting explicitly the curvature parametrisation to the parameters that characterise the cosmological perturbation spectrum. These calculations should give a meaningful result which can then be used to calculate the abundances of PBHs in the current Universe.

Up to this stage, the analysis of the problem is being considered within the assumption of spherical symmetry. It is, in fact, usually assumed that deviations away from spherical symmetry will be negligible in this context. We want to check on this by calculating the evolution of deviations away from spherical symmetry using the formalism developed by C. Gundlach and J.M. Martin-Garcia [86]. This formalism, which was originally developed for studying gravitational wave emission from stellar collapse, is a good starting point for us because it uses an expansion in spherical harmonics, keeping a treatment based on an underlying spherically symmetric calculation complemented by terms representing the sequence of spherical harmonics.

Another problem concerning PBHs which we want to address concerns their possible formation during phase transitions in the early universe. The role of phase transitions in the early universe is to soften the equation of state, which can in principle favour gravitational collapse [87, 65]. PBH formation at around the time of cosmological nucleosynthesis may give rise to some very interesting consequences. The mass scale of 10^5 solar masses (often claimed as the seed mass for later large-scale-structure formation) is also that characterising PBHs forming at this time. To have a good treatment of PBH formation at this epoch, it is necessary to take into account both e^+e^- production/annihilation and the diffusion of neutrinos (whose mean free path is of the same order as the horizon scale at this time). For these simulations we intend to use the methodology developed at SISSA by Miller and Rezzolla [88, 89]. By investigating subsequent accretion onto PBHs with the aid of our analytical and numerical techniques, developed in the work described above, we expect to clarify the possible significance of PBHs for the formation of QSOs and AGNs, as well as for the formation of large-scale structure. Other interesting questions concern the possible contribution of PBHs to dark matter and whether the observed Intermediate Mass Black Holes might have their origin as PBHs.

The final aspects which we would like to address concern the evaporation of PBHs and comparison of the predicted abundances of PBHs with observations. This is a key point that would link the theoretical work described above with observations, with the results obtained being confronted with the observed gamma-ray bursts, cosmic rays and products of cosmological nucleosynthesis. A possible constraint to be considered is the entropy bound/holographic principle argument, related to the thermodynamical properties of black holes. Up to now, this has been considered only within a very simple scenario [90], without using realistic models for the gravitational collapse of cosmological perturbations.

The objective in studying these constraints is to develop a powerful tool for constraining

key parameters of the early universe, relevant on scales much smaller than those disclosed by the CMB and large-scale structure. Taking into account that PBH formation is tightly linked with the primordial perturbation spectrum, we expect that this will be effective for placing informative constraints on models for inflation or any other models giving a prescription for primordial cosmological perturbations.

Appendix A

Friedmann model with non-zero Λ

We present here some of the analytic expressions describing an expanding universe with $\Lambda \neq 0$ in the radiation-dominated era. These equations are certainly not being presented here for the first time but they are not easy to find in the usual cosmology textbooks and we think that it may be useful to present them together here. In this part only, we use physical units and do not set $c = G = 1$.

First, we note the forms taken by the Friedman equation and the associated acceleration equation (we are taking the spatially flat case):

$$\left(\frac{\dot{a}}{a}\right) = \frac{8\pi G}{3c^2}e + \frac{\Lambda c^2}{3}, \tag{A.1}$$

$$\left(\frac{\ddot{a}}{a}\right) = -\frac{8\pi G}{3c^2}\left(e - \frac{\Lambda c^4}{8\pi G}\right), \tag{A.2}$$

where e is the energy density of radiation which scales as

$$e = e_i\left(\frac{a_i}{a}\right)^4, \tag{A.3}$$

(here the subscript i refers to a fiducial initial time). Inserting this into (A.1), we obtain the integral equation

$$\int_0^{(a_i/a)} \frac{\frac{a_i}{a'}\, d\left(\frac{a_i}{a'}\right)}{\sqrt{\frac{8\pi G}{3c^2}e_i + \frac{\Lambda c^2}{3}\left(\frac{a_i}{a'}\right)^4}} = \int_0^t dt'. \tag{A.4}$$

If $\Lambda > 0$, the solution for the scale factor is

$$a(t) = a_i\left(\frac{8\pi G e_i}{\Lambda c^4}\right)^{1/4}\left[\sinh\left(2\sqrt{\frac{\Lambda}{3}}ct\right)\right]^{1/2}, \tag{A.5}$$

Using (A.5) in (A.1) we get the Hubble parameter

$$H(t) = \sqrt{\frac{\Lambda}{3}}c\coth\left(2\sqrt{\frac{\Lambda}{3}}ct\right), \tag{A.6}$$

which, in the limit $\Lambda \to 0$, reduces to the standard expression $H(t) = 1/2t$. Inserting (A.6) into (A.1) we get the expression for $e(t)$

$$e(t) = \frac{\Lambda c^4}{8\pi G}\left[\sinh\left(2\sqrt{\frac{\Lambda}{3}}ct\right)\right]^{-2}. \tag{A.7}$$

Another useful expression is the inverse of (A.6)

$$t = \left(4\sqrt{\frac{\Lambda}{3}}c\right)^{-1} \ln\left(\frac{H + \sqrt{\frac{\Lambda}{3}}c}{H - \sqrt{\frac{\Lambda}{3}}c}\right)., \tag{A.8}$$

which we have used in the cosmic time code to calculate the initial time for the calculation.

Finally, for completeness, we calculate the expression for the two cosmological horizons. From (A.6) we get a straightforward the expression for the Hubble horizon $R_H \equiv c/H$,

$$R_H(t) = \left(\frac{\Lambda}{3}\right)^{-\frac{1}{2}} \tanh\left(2\sqrt{\frac{\Lambda}{3}}ct\right). \tag{A.9}$$

For the particle horizon, the calculation is more complicated. From the definition

$$R_h(t) \equiv a(t)\int_0^t \frac{cdt'}{a(t')}, \tag{A.10}$$

we get

$$R_h(t) = \left[\sinh\left(2\sqrt{\frac{\Lambda}{3}}ct\right)\right]^{1/2}\int_0^t \frac{du}{\left[\sinh\left(2\sqrt{\frac{\Lambda}{3}}cu\right)\right]^{1/2}}, \tag{A.11}$$

and, with the aid of integral tables, we get the final form of the solution

$$R_h(t) = \left(2\sqrt{\frac{\Lambda}{3}}\right)^{-1}\left[\sinh\left(2\sqrt{\frac{\Lambda}{3}}ct\right)\right]^{1/2} F(\phi, k) \tag{A.12}$$

where $F(\phi, k)$ is an incomplete elliptic integral of the first type:

$$F(\phi, k) \equiv \int_0^\phi \frac{d\theta}{(1 - k^2\sin^2\theta)^{1/2}}, \tag{A.13}$$

with

$$\phi = \arccos\left[\frac{1 - \sinh\left(2\sqrt{\frac{\Lambda}{3}}ct\right)}{1 + \sinh\left(2\sqrt{\frac{\Lambda}{3}}ct\right)}\right], \tag{A.14}$$

and

$$k = \frac{1}{\sqrt{2}}. \tag{A.15}$$

When $\Lambda < 0$, relations (A.5), (A.6) and (A.7) are unchanged apart from replacing the hyperbolic functions by the corresponding trigonometric ones. This is consistent with the oscillating behaviour of a universe with $\Lambda < 0$, characterized by a sequence of expanding and contracting phases.

Appendix B

Ricci Scalar calculations for curvature

The general spherically symmetric metric in the cosmic time coordinate is

$$ds^2 = -a^2 dt^2 + b^2 dr^2 + R^2 d\Omega^2 \tag{B.1}$$

where the the metric tensor $g_{\alpha\beta}$ is diagonal and a, b and R are, in general, functions of r and t. The Christoffel symbols different from zero are calculated from

$$\Gamma^{\alpha}_{\beta\gamma} = \frac{1}{2} g^{\alpha\alpha} \left(\frac{\partial g_{\beta\alpha}}{\partial x^{\gamma}} + \frac{\partial g_{\gamma\delta}}{\partial x^{\beta}} - \frac{\partial g_{\beta\gamma}}{\partial x^{\delta}} \right), \tag{B.2}$$

and making the whole calculation one obtains

$$\Gamma^0_{00} = \frac{1}{a}\frac{\partial a}{\partial t} \qquad \Gamma^0_{01} = \frac{1}{a}\frac{\partial a}{\partial r} \qquad \Gamma^0_{02} = 0 \qquad \Gamma^0_{03} = 0$$

$$\Gamma^0_{10} = \frac{1}{a}\frac{\partial a}{\partial r} \qquad \Gamma^0_{11} = \frac{b}{a^2}\frac{\partial b}{\partial t} \qquad \Gamma^0_{12} = 0 \qquad \Gamma^0_{13} = 0$$

$$\Gamma^0_{20} = 0 \qquad \Gamma^0_{21} = 0 \qquad \Gamma^0_{22} = \frac{R}{a^2}\frac{\partial R}{\partial t} \qquad \Gamma^0_{23} = 0$$

$$\Gamma^0_{30} = 0 \qquad \Gamma^0_{31} = 0 \qquad \Gamma^0_{32} = 0 \qquad \Gamma^0_{33} = \frac{R}{a^2}\frac{\partial R}{\partial t}\sin^2\theta$$

$$\Gamma^1_{00} = \frac{a}{b^2}\frac{\partial a}{\partial r} \qquad \Gamma^1_{01} = \frac{1}{b}\frac{\partial b}{\partial t} \qquad \Gamma^1_{02} = 0 \qquad \Gamma^1_{03} = 0$$

$$\Gamma^1_{10} = \frac{1}{b}\frac{\partial b}{\partial t} \qquad \Gamma^1_{11} = \frac{1}{b}\frac{\partial b}{\partial r} \qquad \Gamma^0_{12} = 0 \qquad \Gamma^0_{13} = 0$$

$$\Gamma^1_{20} = 0 \qquad \Gamma^1_{21} = 0 \qquad \Gamma^1_{22} = -\frac{R}{b^2}\frac{\partial R}{\partial r} \qquad \Gamma^1_{23} = 0$$

$$\Gamma^0_{30} = 0 \qquad \Gamma^1_{31} = 0 \qquad \Gamma^1_{32} = 0 \qquad \Gamma^1_{33} = -\frac{R}{b^2}\frac{\partial R}{\partial r}\sin^2\theta$$

$$\Gamma^2_{00} = 0 \qquad \Gamma^2_{01} = 0 \qquad \Gamma^2_{02} = \frac{1}{R}\frac{\partial R}{\partial t} \qquad \Gamma^2_{03} = 0$$
$$\Gamma^2_{10} = 0 \qquad \Gamma^2_{11} = 0 \qquad \Gamma^2_{12} = \frac{1}{R}\frac{\partial R}{\partial r} \qquad \Gamma^2_{13} = 0$$
$$\Gamma^2_{20} = \frac{1}{R}\frac{\partial R}{\partial t} \qquad \Gamma^2_{21} = \frac{1}{R}\frac{\partial R}{\partial r} \qquad \Gamma^2_{22} = 0 \qquad \Gamma^2_{23} = 0$$
$$\Gamma^2_{30} = 0 \qquad \Gamma^2_{31} = 0 \qquad \Gamma^2_{32} = 0 \qquad \Gamma^2_{33} = -\sin\theta\cos\theta$$
$$\Gamma^3_{00} = 0 \qquad \Gamma^3_{01} = 0 \qquad \Gamma^3_{02} = 0 \qquad \Gamma^3_{03} = \frac{1}{R}\frac{\partial R}{\partial t}$$
$$\Gamma^3_{10} = 0 \qquad \Gamma^3_{11} = 0 \qquad \Gamma^3_{12} = 0 \qquad \Gamma^3_{13} = \frac{1}{R}\frac{\partial R}{\partial r}$$
$$\Gamma^3_{20} = 0 \qquad \Gamma^3_{21} = 0 \qquad \Gamma^3_{22} = 0 \qquad \Gamma^3_{23} = \frac{\sin\theta}{\cos\theta}$$
$$\Gamma^3_{30} = \frac{1}{R}\frac{\partial R}{\partial t} \qquad \Gamma^3_{31} = \frac{1}{R}\frac{\partial R}{\partial r} \qquad \Gamma^3_{32} = \frac{\sin\theta}{\cos\theta} \qquad \Gamma^3_{33} = 0$$

In the FRW metric the metric components are simpler

$$a = 1 \quad b = \frac{s(t)}{\sqrt{1-Kr^2}} \quad R = s(t)r \tag{B.3}$$

where the curvature K is a constant equal to 0, ± 1 and the non-zero Christoffel Symbols are

$$\Gamma^0_{11} = \frac{s\dot{s}}{1-Kr^2} \qquad \Gamma^0_{22} = s\dot{s}r^2 \qquad \Gamma^0_{33} = s\dot{s}r^2\sin^2\theta$$
$$\Gamma^1_{11} = \frac{Kr^2}{1-Kr^2} \qquad \Gamma^1_{22} = -\left(1-Kr^2\right)r \qquad \Gamma^1_{33} = -\left(1-Kr^2\right)r\sin^2\theta$$

$$\Gamma^1_{10} = \Gamma^1_{01} = \Gamma^2_{20} = \Gamma^2_{02} = \Gamma^3_{30} = \Gamma^3_{03} = \frac{\dot{s}}{s}$$
$$\Gamma^2_{21} = \Gamma^2_{12} = \Gamma^3_{31} = \Gamma^3_{13} = \frac{1}{r}$$
$$\Gamma^2_{33} = -\sin\theta\cos\theta$$
$$\Gamma^3_{31} = \Gamma^3_{13} = \frac{\sin\theta}{\cos\theta}$$

The components of the Ricci Tensor are given by

$$R_{\alpha\beta} = \Gamma^\gamma_{\delta\gamma}\Gamma^\delta_{\alpha\beta} - \Gamma^\gamma_{\delta\beta}\Gamma^\delta_{\alpha\gamma} + \frac{\partial\Gamma^\gamma_{\alpha\beta}}{\partial x^\gamma} - \frac{\partial\Gamma^\gamma_{\alpha\gamma}}{\partial x^\beta} \tag{B.4}$$

and to calculate the Ricci scalar we need to take into account only the diagonal components $R_{\alpha\alpha}$. In the background universe with the FRW metric we have that

$$R_{00} = 3\frac{\ddot{s}}{s} \tag{B.5}$$

$$R_{11} = \frac{s\ddot{s} + 2\dot{s}^2 + 2K}{1-Kr^2} \tag{B.6}$$

$$R_{22} = (s\ddot{s} + 2\dot{s} + 2K)\, r^2 \tag{B.7}$$

$$R_{33} = R_{22} \sin^2\theta \tag{B.8}$$

and these are used to calculate the scalar curvature

$$R = 6\left(\frac{\ddot{s}}{s} + \frac{\dot{s}^2}{s^2} + \frac{K}{s^2}\right). \tag{B.9}$$

The three curvature is obtained by removing the terms with the time derivatives and so

$$R^{(3)} = 6\frac{K}{s^2} \tag{B.10}$$

In the case of the general metric given by (B.1), the diagonal components of the Ricci tensor are

$$R_{00} = \frac{1}{a}\frac{\partial a}{\partial t}\left(\frac{1}{b}\frac{\partial b}{\partial t} + \frac{2}{R}\frac{\partial R}{\partial t}\right) + \frac{a}{b^2}\frac{\partial a}{\partial r}\left(\frac{2}{R}\frac{\partial R}{\partial r} - \frac{1}{b}\frac{\partial b}{\partial r}\right) + \\ + \frac{a}{b^2}\frac{\partial^2 a}{\partial r^2} - \frac{1}{b}\frac{\partial^2 b}{\partial t^2} - \frac{2}{R}\frac{\partial^2 R}{\partial t^2} \tag{B.11}$$

$$R_{11} = \frac{b}{a^2}\frac{\partial b}{\partial t}\left(\frac{2}{R}\frac{\partial R}{\partial t} - \frac{1}{a}\frac{\partial a}{\partial t}\right) + \frac{1}{b}\frac{\partial b}{\partial r}\left(\frac{1}{a}\frac{\partial a}{\partial r} + \frac{2}{R}\frac{\partial R}{\partial r}\right) + \\ + \frac{b}{a^2}\frac{\partial^2 b}{\partial t^2} - \frac{1}{a}\frac{\partial^2 a}{\partial r^2} - \frac{2}{R}\frac{\partial^2 R}{\partial r^2} \tag{B.12}$$

$$R_{22} = \frac{R}{a^2}\frac{\partial R}{\partial t}\left(\frac{1}{b}\frac{\partial b}{\partial t} - \frac{1}{a}\frac{\partial a}{\partial t}\right) + \frac{R}{b^2}\frac{\partial R}{\partial r}\left(\frac{1}{b}\frac{\partial b}{\partial r} - \frac{1}{a}\frac{\partial a}{\partial r}\right) + \\ + \left(\frac{1}{a}\frac{\partial R}{\partial t}\right)^2 - \left(\frac{1}{b}\frac{\partial R}{\partial r}\right)^2 + R\left(\frac{1}{a^2}\frac{\partial^2 R}{\partial t^2} - \frac{1}{b^2}\frac{\partial R}{\partial r^2}\right) + 1 \tag{B.13}$$

$$R_{33} = R_{22} \sin^2\theta \tag{B.14}$$

Now we can write the scalar curvature for the generic metric (B.1) and it is useful to define the following operators:

$$D_t \equiv \frac{1}{a}\frac{\partial}{\partial t}, \quad D_t^2 \equiv \frac{1}{a^2}\frac{\partial^2}{\partial t^2}, \quad D_r \equiv \frac{1}{b}\frac{\partial}{\partial r}, \quad D_r^2 \equiv \frac{1}{b^2}\frac{\partial^2}{\partial r^2} \tag{B.15}$$

We then get

$$R = 2\left[\frac{D_t^2 b}{b} + 2\frac{D_t^2 R}{R} - \frac{D_r^2 a}{a} - 2\frac{D_r^2 R}{R} + \left(\frac{D_t R}{R}\right)^2 - \left(\frac{D_r R}{R}\right)^2 + 2\frac{D_t b}{b}\frac{D_t R}{R} -\right.$$

$$-2\frac{D_t a}{a}\frac{D_t R}{R} - \frac{D_t a}{a}\frac{D_t b}{b} + 2\frac{D_r b}{b}\frac{D_r R}{R} + \frac{D_r a}{a}\frac{D_r b}{b} - 2\frac{D_r a}{a}\frac{D_r R}{R} + \frac{1}{R^2}\Bigg] \tag{B.16}$$

and substituting in the expressions for the coefficients a, b and R given by (5.18,5.20,5.21) and expressing $\tilde{a}, \tilde{b}, \tilde{R}$ in terms of $K(r)$, we get with the use also of (5.16), that the Ricci scalar is given by

$$R = 6\left[\frac{\ddot{s}}{s}\left(1 + \epsilon\frac{3\gamma - 1}{5 + 3\gamma}\mathcal{K}\right) + \frac{\dot{s}^2}{s^2}\left(1 - \epsilon\frac{2(2 + 3\gamma)}{5 + 3\gamma}\mathcal{K}\right) + \frac{\mathcal{K}}{s^2}\right], \tag{B.17}$$

where

$$\mathcal{K} = K(r) + \frac{r}{3}K'(r)\,. \tag{B.18}$$

It is useful to compare this with (B.9).

Bibliography

[1] Hawking S. W. 1971 *MNRAS* **152** 75

[2] Carr B. J. & Hawking S. W. 1974 *MNRAS* **168**, 399

[3] Musco I., Miller J. C.& Rezzolla L. 2005 *Class. Quantum Grav.*, **22**, 1405

[4] Polnarev A. G. & Musco I. 2006 *Class. Quantum Grav.* - to be submitted

[5] Musco I. & Miller J. C. 2006 - in preparation

[6] Liddle A.R. & Lyth D.H. 2000 *Cosmological Inflation and Large-Scale Structure* Cambridge University Press

[7] Padmanabhan T. 1993 *Structure Formation in the Universe* Cambridge University Press

[8] Kolb E. W. & Turner M. S. 1990 *The Early Universe* Addison-Wesley Pubblishing Company

[9] Steinhardt P. J., Wang L. & Zlatev I. 1999 *Phys. Rev. D* **59** 123504

[10] Perlmutter S., Turner M. S. & White M. 1999 *Phys. Rev. Lett.* **83** 670

[11] Pagel B. E. J. 1997, *Nucleosynthesis and chemical evolution of Galaxies*, Cambridge University Press, UK.

[12] Schramm D. N. & Turner M. S. 1998 *Rev. Mod. Phys* **70** 303.

[13] Kofman L., Linde A. D. & Starobinsky A. A. 1997 *Phys.Rev. Lett.***73** 3195

[14] Kofman L., Linde A. D. & Starobinsky A. A. 1997 *Phys. Rev. D***56** 3258

[15] Harrison E. R. 1970 *Phys. Rev. D* **1** 2726

[16] Zel'dovich Ya. B. 1970 *Astron. Astrophys.* **5** 84

[17] Carr B.J. 2003 *Lect. Notes Phys.* **631** 301

[18] Wald R. W. 1984 *General Relativity* The University of Chicago Press

[19] Luminet J. P. astro-ph/9801252

[20] Zel'dovich Ya.B. & Novikov I.D. 1966 *Astron.Zh.* **43** 758 [*Sov.Astron.* **10** 602 (1967)]

[21] I. D. Novikov, A. G. Polnarev, A. A. Starobinsky & Ya. B. Zeldovich 1979 *Astron. Astrophys.* **80** 104

[22] Miyama S & Sato K. 1978 *Prog. Theor. Phys.* **59** 1012

[23] Kohri K. & J. Yokoyama 2000 *Phys. Rev. D* **61** 023501

[24] He P. & Fang L. Z. 2002 *Astrophys. J. Lett* **568** L1

[25] Crawford M. & Schramm D. N. 1982 *Nature* **298** 538

[26] Hawking S. W. Moss I. & Stewart J. 1982 *Phys. Rev. D* **26** 2681

[27] La D. & Steinhardt 1989 *Phys. Lett. B* **220** 375

[28] Caldwell R. & Casper P. 1996 *Phys. Rev. D***53** 3002

[29] Garriga J. & Sakellariadou 1993 *Phys. Rev. D***48** 2502

[30] Hawking S. W. 1989 *Phys. Lett. B* **231** 237

[31] MacGibbon J.H. & Brandenberger B. R. 1990 *Phys. Rev. D***57** 2158

[32] Polnarev A. G. & Zembroricz R. 1988 *Phys. Rev. D***43** 1106

[33] Carr B.J. 1975 *Astrophys.J.* **201** 1

[34] Nadezhin D.K., Novikov I.D. & Polnarev A. G. 1978 *Astron.Zh.* **55** 216 [*Sov.Astron.* **22(2)** 129 (1978)]

[35] May M.M. & White R.H. 1966 *Phys.Rev.* **141** 1232

[36] Pondurets M.A. 1964 *Astron.Zh.* **41** 1090 [*Sov.Astron.* **8** 868 (1965)]

[37] Bicknell G.V. & Henriksen R. N. 1979 *Astrophys.J.* **232** 670

[38] Niemeyer J.C. & Jedamzik K. 1998 *Phys.Rev.Lett* **80** 5481

[39] Niemeyer J.C. & Jedamzik K. 1999 *Phys.Rev.D* **59** 124013

[40] Choptuik M.W. 1993 *Phys. Rev. Lett.* **70** 9

[41] Gundlach C. 1999 *Living Rev.Rel.* [`http://www.livingreviews.org/lrr-1999-4`]

[42] Hawke I. & Stewart J. M. 2002 *Class. Quantum Grav.* **19** 3687

[43] Green A.M., Liddle A.R. & Malik K.A., Sasaki M. 2004 *Phys.Rev.D*, **70**, 041502

[44] Shibata M. & Sasaki M. 1999 *Phys.Rev.D* **60** 084002

[45] Green A.M. & Liddle A.R. 1997 *Phys.Rev.D* **56** 6166

[46] Carr B. J., Gilbert J. H. & Lidsey J. E. 1994 *Phys. Rev. D***50** 4853

[47] MacGibbon J. H. 1987 *Nature* **329** 308

[48] MacGibbon J. H. & Carr B. J. 1991 *Astrophys. J.* **371** 447

[49] Carr B. J. 1985, *Observational and Theoretical Aspects of relativistic astrophysics and Cosmology* edited by Sanz J. L. and Goiciechea L. J. (World Scientific, Singapore)

[50] Page D. N. 1976 *Phys. Rev. D***13** 198

[51] Green A. M. & Liddle A. R. 1999 *Phys. Rev. D* **60** 063509

[52] Mujana S. & Sato K. 1978 *Prog. Theor. Phys.* **59** 1012

[53] Vainer B. V. & Nasel'skii P. D. 1978 *Sov. Astron.* **22** 138

[54] Zel'dovich Ya. B., Starobinskii A. A., Kholpov M. Yu. & Chechëtkin V. M. 1977 *Sov. Astron. Lett.* **3** 110

[55] Lindley D.1980 *MNRAS* **193** 593 x

[56] Vainer B. V., DryzhakovaD. V. & Nasel'skii P. D.1978 *Sov. Astron. Lett.* 4 185

[57] Carr B. J. & Lidsey J. E. 1993 *Phys. Rev. D***48** 543

[58] Carr B. J. & Lidsey J. E. 1994 *Phys. Rev. D***50** 4853

[59] Blais D., Kiefer C. & Polarski D. 2002 *Phys. Lett. B* **535** 11

[60] Kim H., Lee C. H. & MacGibbon J. H. 1999 *Phys. Rev. D***59** 063004

[61] Green A. M., Liddle A. R. & Riotto A. 1997 *Phys. Rev. D***56** 7559

[62] Hodges H. M. & Blumenthal G. R. 1990 *Phys. Rev. D***42** 3329

[63] Blais D., Bringmann T. & Polarski D. 2003 *Phys. Rev. D***67** 024024

[64] Polarski D. 2002 *Phys. Lett. B* **328** 193

[65] Jedamzik K. & Niemeyer J.C. 1999 *Phys.Rev.D* **59** 124014

[66] Jedamzik K. 1997 *Phys. Rev. D***55** R5871

[67] Page D. N. 1977 *Phys. Rev. D***16** 2402

[68] MacGibbon J. H. 1991 *Phys. Rev. D***44** 376

[69] MacGibbon J. H. & Webber B. R. 1990 *Phys. Rev. D***41** 3052

[70] MacGibbon J. H. & Carr B. J. 1991 *Astrophys. Journal* **371** 447

[71] Carr B. J. & MacGibbon J. H. 1998 *Phys. Rep,* **307** 141

[72] Misner C.W. & Sharp D.H. 1964 *Phys.Rev* **136** B571

[73] Hernandez W.C. & Misner C.W. 1966 *Astrophys.J.* **143** 452

[74] Miller J.C. & Sciama D.W. 1980 in *General Relativity and Gravitation: one hundred years after the birth of Albert Einstein - Vol.2* ed. Held A. (Plenum Press: New York), p. 359

[75] Miller J.C. & Motta S. 1989 *Class. Quantum Grav.* **6** 185

[76] Baumgarte T.W., Shapiro S.L. & Teukolsky S.A. 1995 *Astrophys.J.* **443** 717

[77] Miller J.C. & Pantano O. 1990 *Phys.Rev.D* **42** 3334

[78] Harada T., Carr B. J. & Goymer C. 2002 *Phys. Rev. D* **66** 104023

[79] Harada T. & Carr B.J. 2005 *Phys. Rev. D***71** 104009

[80] Harada T. & Carr B.J. 2005 *Phys. Rev. D***71** 104010

[81] Koike T, Hara T. & Adachi S. 1995 *Phys.Rev.Lett.* **74** 5170

[82] Lyth D. H., Malik K. A & Sasaki M. 2005 *JCAP* **0505** 004

[83] Langlois D. & Vernizzi F. 2005 *Phys.Rev.Lett.* **95** 091303

[84] Evans C. R. & Coleman J. S. 1994 *Phys. Rev. Lett* **72** 1782

[85] Harada T. 2001 *Calss. Quantum Grav.* **18** 4549

[86] Gundlach C. & Martin-Garcia J.M. *Phys. Rev. D* **61** 084024

[87] Jedamzik K. & Fuller G.M. 1994 *Astroph. Journal* **422** 33

[88] Rezzolla L. & Miller J.C. 1994 *Class. Quantum Grav.* **11** 1815

[89] Miller J.C. & Rezzolla L. 1995 *Phys.Rev.D* **51** 4017

[90] Lee H. K. 2002 *Phys.Rev. D* **66** 063001